The Synthesis, Structure and Magnetic Properties of *O*-Vanillin-Derived Schiff Base Polynuclear Lanthanide Single-Molecule Magnets

Yu Ting Jiang

A thesis submitted to the
Faculty of Graduate and Postdoctoral Studies
in partial fulfillment of the requirements for the
MSc degree in Chemistry

Department of Chemistry

Faculty of Science

University of Ottawa

Abstract

This thesis describes the synthesis, characterization and magnetic investigation of homometallic lanthanide complexes based on two different *o*-vanillin-derived Schiff base ligands: H_2ovph and H_2ovgrd. The studies were performed using single crystal X-ray diffractometry, Powder XRD and SQUID magnetometry. Chapter 2 focuses on dinuclear systems **1-8** coordinated to the ligand H_2ovph and presents their structural and magnetic properties, mainly with respect to their intramolecular interactions. Chapter 3 describes two hexanuclear systems, **9** (Dy^{III}) and **10** (Gd^{III}), with trigonal prism-assembled core structures. A structural comparison to other similar complexes in the literature is performed. A series of dinuclear complexes, **11-15**, based on the ligand H_2ovgrd are described in Chapter 4, focusing on the synthetic strategy, crystal structures and magnetism. The presence of the lanthanide contraction is evident in this system of complexes and is consistent with the intrinsic lanthanide contraction property.

Acknowledgements

First and foremost I offer my sincerest gratitude to my supervisor, Dr. Muralee Murugesu, who has been continuously supportive throughout my study and thesis writing with his patience, motivation and immense knowledge.

I would also like to express my thanks to Ilia Korobkov, the X-ray crystallographer. He has aided me with all my samples and tutored me in how to understand their structures. I would not be able to complete my research without his help. Also thanks to Prof. Liviu F. Chibotaru, who helped with the computational work.

In my daily work I have been blessed with a friendly and cheerful group of fellow students. Fatemah Habib, my knowledgeable office-mate and good friend, has provided countless hours helping me from the first day till now. Her active and enthusiastic attitude towards life has fascinated me a lot and I really enjoyed every minute that I spent with her. Rebecca Holmber and Jennifer Le Roy, the first two girls that I met here, are also really nice and selfless and helped me a lot on my work, especially with PXRD and unit cell measurements. Elena Sebastiao, who joined the group at the same time with me, encouraged me to get used to life in Canada, considering I am from a foreign country. She is one of the sweetest girls I have ever met. Dr. Damir Safin and Dr. Amélie Pialat have been invaluable helpful not only to me but the entire group by sharing their knowledge, leading discussion during group meetings and giving advices upon our problems. And I would like to thank Gabriel Brunet and Katie Harriman for all the fun time we had, especially the past summer with Benjamin Bouny, Antonin Keller and Amo Chebini together. I also want to attribute my completion to my former lab colleagues and dear friends, Dr. Tomoko Aharen, Dr. Cyril Cook, Judith Caballero, Sarah Petit and Irina Kuehne, for all the good moments they shared with me.

Finally, I thank all my friends in Ottawa who support me a lot and make me feel at home here. Thank to my best friends in China and all around the world, who have been with me all the time no matter how far we are. I thank my parents for bringing me here and supporting me throughout my life.

List of Tables

List of Figures

List of Ligands and Complexes

H_2ovph = 2-hydroxy-3-methoxybenzaldehyde (pyridine-2-carbonyl) hydrazone

H_2ovgrd = (E)-2-(dimethylamino)-N'-(2-hydroxy-3-methoxybenzylidene) acetohydrazide

1	$[Dy^{III}_2(ovph)_2(DMF)_2Cl_2]$
2	$[Er^{III}_2(ovph)_2(DMF)_2Cl_2]$
3	$[Tb^{III}_2(ovph)_2(DMF)_2Cl_2]$
4	$[Dy^{III}_2(ovph)_2(IPA)_2Cl_2]$
5	$[Er^{III}_2(ovph)_2(IPA)_2Cl_2]$
6	$[Tb^{III}_2(ovph)_2(IPA)_2Cl_2]$
7	$[Dy^{III}_2(ovph)_2(H_2O)_3(EtOH)Cl_2]$
8	$[Dy^{III}_2(Hovph)_2(OH)Cl_3(H_2O)]\cdot 2H_2O$
9	$[Dy^{III}_6(ovph)_6(IPA)_3Cl_3]\cdot 6MeCN\cdot IPA\cdot TEAOH$
10	$[Gd^{III}_6(ovph)_6(IPA)_3Cl_3]\cdot 6MeCN\cdot TEAOH$
11	$[Gd^{III}_2(ovgrd)_2(acac)_2(H_2O)_2]\cdot EtOH$
12	$[Dy^{III}_2(ovgrd)_2(acac)_2(H_2O)_2]\cdot EtOH$
13	$[Ho^{III}_2(ovgrd)_2(acac)_2(H_2O)_2]\cdot EtOH$
14	$[Er^{III}_2(ovgrd)_2(acac)_2(H_2O)_2]\cdot EtOH$
15	$[Yb^{III}_2(ovgrd)_2(acac)_2(H_2O)_2]\cdot EtOH$

List of Abbreviations

Ln	lanthanide
SMM	single molecule magnet
Me	methyl
MeCN	acetonitrile
MeOH	methanol
EtOH	ethanol
IPA	isopropanol
DMF	dimethylformamide
mg	milligram
mL	millilitre
mmol	millimole
IR	infrared
NMR	nuclear magnetic resonance
SQUID	super-conducting quantum interference device
ac	alternating current
dc	direct current
D	zero-field splitting parameter
K	kelvin
Oe	oersted
H	field
Hz	hertz
M	magnetization
T	temperature
h	hour
χ	molar magnetic susceptibility
χ'	in-phase magnetic susceptibility
χ''	out-of-phase magnetic susceptibility

μ_B	bohr magneton
U_{eff}	effective energy barrier
cm^3	cubic centimetres
br	broad
s	strong (IR), singlet (NMR)
m	medium (IR), multiplet (NMR)
w	weak
d	doublet
t	triplet
R.T.	room temperature

Table of Contents

Chapter 1

Introduction

1.1 Introduction to Molecular Magnetism

According to Ritter, "one of the most interesting but challenging technology required today is to find more efficient ways to store and process digital information. In order to achieve higher density information storage, one possibility would be to make the magnetic nanoparticles that are currently used even smaller and squeeze more data onto them; another is to investigate different methods to process information, such as quantum-based computing" (**2004**). [1] The application of Single-Molecule Magnets (SMMs) [2] would be promising as they possess the features of both.

1.1.1 Single Molecule Magnets (SMMs)

A conventional magnet can be regarded as containing a large number of magnetic domains, which accumulates the alignment of numerous of spin centers in the bulk material and give rise to their spontaneous magnetization. With the applied of a small external magnetic field, the magnetic moments of all domains can be oriented to the direction of the applied field. Then, the data storage capacity for a certain conventional magnet is limited by the size of the domains. Single molecule magnets possess intriguing properties that are different from traditional magnets. First of all, as fully functionalized magnetic materials, SMMs allow the access to magnetism on molecular scale. In Ritter's report, the maximum amount of information that can be stored on a cobalt-based magnetic material hard drive or other devices within an area of 1 cm^2 is about 3 billion bits. [1] That size of material corresponds to approximately thousands of atoms. However, around 30 trillion SMMs can fit into the same area thanks to their much smaller size, which means a 10,000 times greater storage

density than the current best computer manufactures can achieve. Besides their appealing size, more advantages can be taken from the chemical side. SMMs are commonly soluble in organic solvents because of the surrounding organic ligands which also prevent the magnetic cores from interacting with each other. [1] Moreover, the more uniform size and structure of SMMs, with air-stability, can make them suitable for long term storage.

In 1980, the mixed-valence $[Mn_{12}O_{12}(OAc)_{16}(H_2O)_4]\bullet 2AcOH\bullet 4H_2O$ (Mn_{12}-Ac) was reported. [3] Not until a decade later, slow relaxation of magnetization was observed by applying dynamic magnetic susceptibility measurements. [4] Interestingly, the hysteresis measurements presented steps at low temperature for this complex. [5] Since the magnetic properties of Mn_{12}-Ac are molecular in origin, it can be considered as the discovery of SMM phenomenon. Such SMMs can reveal classical magnet properties, [2] and quantum properties, such as quantum tunneling of the magnetization (QTM) [5, 6] and quantum phase interference. [7] The magnetic memory properties of SMMs have intrigued scientists over the past 20 years, with their effort, some improvements on the magnetic properties and better understandings of these SMM systems have been achieved. As one way to compare the success of different SMMs, the bigger the magnitude of the anisotropy barrier, the more prominent the SMM properties at higher temperatures. [8a] At the time of writing, the current record anisotropy barrier for an SMM have reached 909 K. [8]

1.1.2 Quantum Tunneling of the Magnetization

The origin of magnetism in the SMMs is the spins on individual metal ions which couple to give rise to a high-spin ground state (for example Mn_{12}-Ac [3] with $S = 10$). [9] The SMMs have axial Zero Field Splitting (ZFS), which leads to a double-well potential between "spin-up" (the states with positive M_S, $M_S = S$) and "spin-down" (the states with negative M_S, $M_S = -S$) states in each potential well linked by a barrier (Figure 1.1). At zero field, all the degenerate levels are paired. And the barrier ΔE is determined by $|D|S^2$ and $|D|(S^2 - ¼)$ (S is the total ground spin, D is one of the parameters of the ZFS) [10] for integer or half integer total spin, respectively. In the presence of an external field, the degenerate ground state splits and one of the potential wells will be stabilized and populated

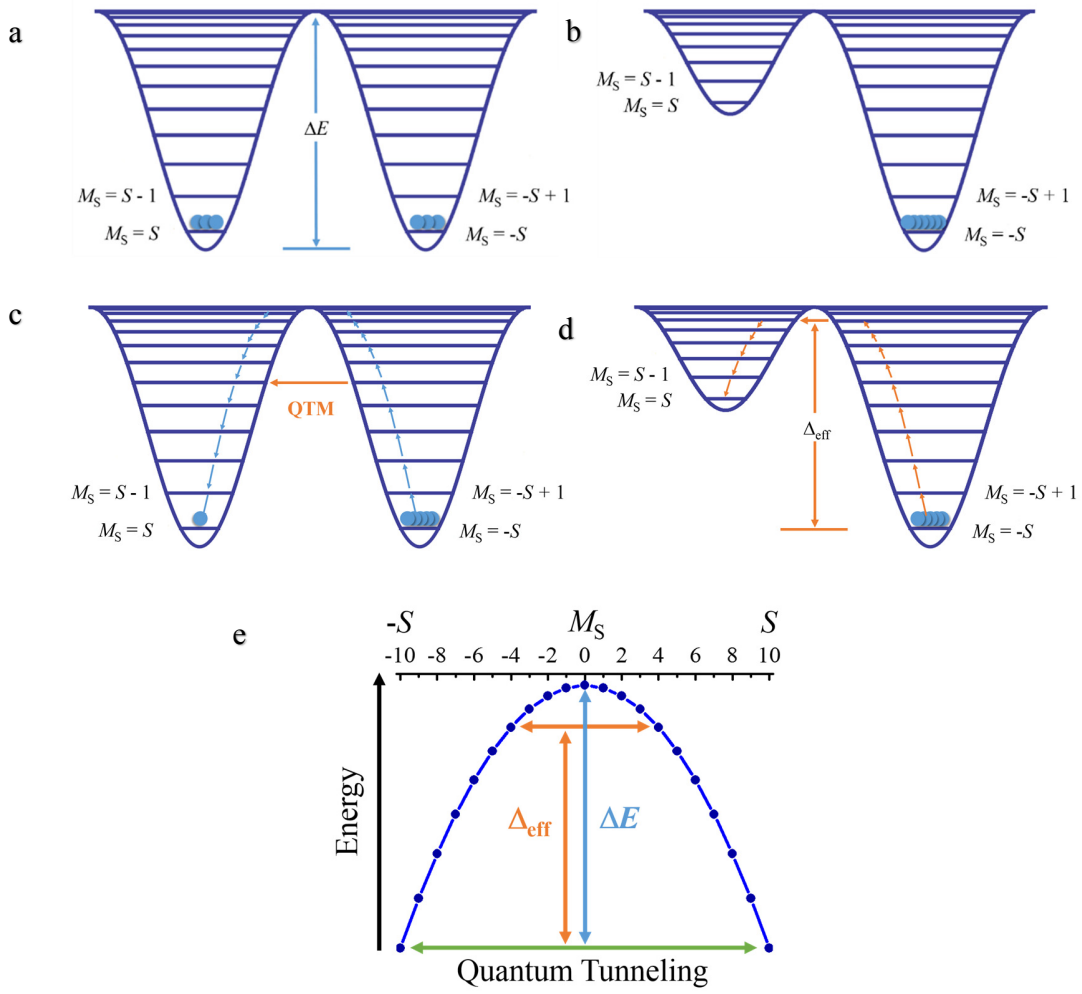

Figure 1.1 Energy levels for a spin state S with easy axis (the magnetization is preferentially oriented parallel to z axis) magnetic anisotropy. The $-M$ levels are localized in the right well and the $+M$ levels in the left well. a) In zero magnetic field the sublevels are degenerate and equally populated. ΔE represents the barrier between the $M_S = \pm S$ states; b) The application of an external field leads to a preferred population of the right well with negative M_S values and the substates with positive M_S values become energetically destabilized. c) After turning off the field, the system goes back to thermal equilibrium through a series of steps corresponding to spin relaxation. d) QTM through the anisotropy barrier (Δ_{eff}) for field induced admixing energy levels (indicated by the orange arrow). e) The energy diagram for an $S = 10$ system. ΔE (in blue) represents the theoretical thermal energy barrier; and the effective energy gap Δ_{eff} (in orange) due to thermally assisted QTM; tunneling occurs between the lowest-lying states $M_S = \pm 10$ (depicted in green). [14]

selectively. Once switching off the magnetic field, the molecules will try to reach the equilibrium population distribution through thermally activated energy levels. However, quantum tunneling can occur alternatively if some levels between the two wells have the same energy and admix by some suitable perturbation, [10] which leads to spin relaxation through different pathways than thermally activated barrier. This tunneling process is so-called resonant tunneling. [11] Also, the tunneling efficiency is determined as a result of many factors including: the anisotropic barrier, the gap between levels which can be influenced by temperature (thermally activated tunneling may occur at intermediate temperatures between pairs of degenerate excited states [12]), as well as the energy level and gap quenching related to the external sweeping field. [10]

It needs to be pointed out that QTM is common for both Kramers' and non-Kramers' ions, [5] even though QTM is forbidden for a system with half-integer spin in zero-applied field predicted by the Kramers theorem. [2, 6] Some mechanisms including long-range dipolar interactions and nuclear coupling have been brought up to explain this, [13] but the reason for the apparent pronounced QTM for Kramers' ions is still a matter of active research.

1.1.3 Characterization of SMMs

Superconducting Quantum Interference Device (SQUID) has been widely used to characterize SMMs in crystalline form. The magnetic susceptibility χ can be measured under an applied direct current (dc) field in the temperature range of 1.8-500 K by using a SQUID magnetometer. This is so-called dc measurement, thus the relationship between χ and temperature can be obtained in different formats, such as $1/\chi$ or χT *vs.* T. From the former type, the Curie constant can be calculated. The latter, the χT *vs.* T, curve(s) can provide important information regarding the room temperature χT value and indicate the intramolecular interaction type. Besides, by studying how the magnetization changes with temperature and the magnetic field applied to the sample, we can determine its magnetism type and related parameters.

Inspecting the variation of in-phase and out-of-phase susceptibilities, denoted by χ' and χ'', respectively, with temperature at several different frequencies is a common method

used to identify an SMM. [14] These measurements involving alternating current (ac), or dynamic, magnetic field, are called ac measurements. The frequencies can range from 0.1-1500 Hz for ac measurements, in the presence or absence of an applied static magnetic field. The presence of frequency-dependent χ'' signals are commonly used to identify SMM behavior, additionally, the $\chi''(\nu)$ isotherms can be used to obtain the energy barrier. Specifically, from each $\chi''(\nu)$ isotherm curve we can determine an average relaxation time, τ, and by the established Arrhenius-type relationship of: $\tau = \tau_0 \exp(U_{eff}/kT)$, where U_{eff} represents the effective energy barrier (or Δ_{eff}) and k is Boltzmann's constant, the anisotropic barrier can be calculated from the slope of $ln\ \tau$ *vs.* T^{-1}, where the plot is linear and $ln\ \tau$ is temperature dependent. [14] For many cases, the Arrhenius plots are only linear across a limited temperature range and very often become temperature independent in the lower temperature range, where $ln\ \tau$ is no longer dependent on temperature. This is because the relaxation mechanism is changing from thermally activated to quantum tunneling of the magnetization. [10]

1.2 Lanthanide-based SMMs

With 3*d* metal ions and their many accessible oxidation states, we can potentially have many choices to build up different spin states and ground terms. Those systems are mainly governed by Ligand Field considerations. Enhancing the total ground spin S or tweaking the zero field splitting parameter D then becomes the strategy to target larger barriers. But a key example of $\{Mn_{19}\}$ [15] which has a large total spin of $S = 83/2$, only presented a barrier of 5 K. The high symmetry of the molecule leads to the individual anisotropies cancelling each other out almost perfectly, such that D for the whole molecule is estimated to be very small. The general conclusion here would be that a lack of anisotropy will prevent SMM behavior no matter how large the total spin of the molecule is. This explains why Ln-SMMs have been the center of attention for the last few years, since manipulating 4*f* ions is a useful way to introduce anisotropy into the complex. [16]

1.2.1 Electronic Configuration of lanthanides

The electronic configurations for lanthanide elements possess two types which depend on the relative lower energy level. For lanthanum (La), cerium (Ce) and gadolinium (Gd), it is $[Xe]4f^n6s^2$ (n = 1, 2 and 8). And for praseodymium (Pr), neodymium (Nd), promethium (Pm), samarium (Sm), europium (Eu), terbium (Tb), dysprosium (Dy), holmium (Ho), erbium (Er), thulium (Tm), ytterbium (Yb) and lutetium (Lu), the general expression is $[Xe]4f^{n-1}5d^16s^2$, where [Xe] represents the electronic configuration of xenon. It is worth noting that scandium (Sc) and yttrium (Y) are commonly regarded as rare earth elements as well, though they do not have 4*f* electrons, because of their valence electrons belonging to $(n\text{-}1)d^1ns^2$ configuration. [16]

Table 1.1 Ground states, *g*-values and calculated R.T. χT values for Ln^{III} ions.

Ln^{III}	Configuration	Ground State	g_J	χT_{cal}* (emu mol^{-1} K)
Ce	f^1	$^2F_{5/2}$	6/7	0.80
Pr	f^2	$^3H_4$	4/5	1.60
Nd	f^3	$^4I_{9/2}$	5/7	1.64
Pm	f^4	$^5I_4$	3/5	0.90
Sm	f^5	$^6H_{5/2}$	2/7	0.09
Eu	f^6	$^7F_0$		
Gd	f^7	$^8S_{7/2}$	2	7.88
Tb	f^8	$^7F_6$	1 1/2	11.82
Dy	f^9	$^6H_{15/2}$	1 1/3	14.17
Ho	f^{10}	$^5I_8$	1 1/4	14.07
Er	f^{11}	$^4I_{15/2}$	1 1/5	11.48
Tm	f^{12}	$^3H_6$	1 1/6	7.15
Yb	f^{13}	$^2F_{7/2}$	8 2/3	2.57

*$\chi T_{cal} = (1/8)\, g_J^2[J(J+1)]$

The magnetic properties of lanthanides are strongly influenced by the internal nature of *f* orbitals. For instance, *f* orbitals of lanthanide ions have unquenched orbital angular momentum and effective spin-orbital coupling, thus resulting in large anisotropy. [16] Different from the 3*d* transition metals, the crystal-field effects for lanthanide ions are reduced (still significant), while the orbital component of magnetic moment is more important. [14, 17] Thus, a different strategy for lanthanide based SMMs to obtain high

energy barriers is focusing on building large magnetic anisotropy by placing ligands at proper positions with respect to the *f*-electron distribution. [18] Numerous compounds containing lanthanide ions have been described, but exerting control over the ligand or through the coordination environment to enhance the anisotropy remains difficult. On one hand we can benefit from the fantastic coordination abilities and fascinating properties of Ln-based SMMs, on the other hand precise control over the synthesis or theoretical understanding of their properties are still evolving.

1.2.2 Lanthanide Contraction

For lanthanides, as the atomic number increases the radius of the atom or ion decreases gradually. This phenomenon is referred to as "lanthanide contraction" (Figure 1.2). Based on the lowest energy principle, as the atomic number increases an electron is not added to the outermost shell but rather to the inner 4*f* shell and only partly distributed within the 5*s*5*p* shell. Therefore, the increased nuclear charge which is not fully shielded from the added electron consequently results in a stronger attraction that causes the lanthanide contraction. [16]

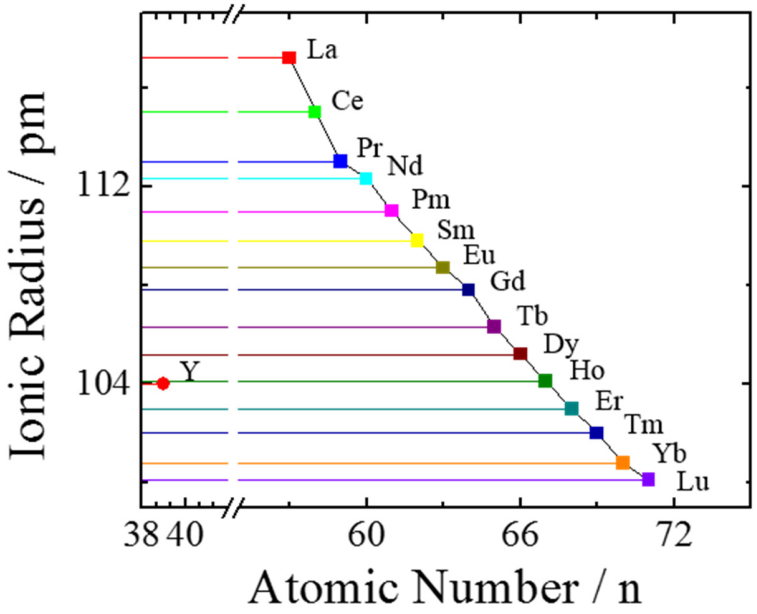

Figure 1.2 The relationship between ionic radius and atomic number of lanthanide ions and Y^{III}. [22]

It is worth noting that the chemical properties of Yttrium are very similar to the lanthanides, and it is always classified as a rare earth element. This can be explained by the radius of Y^{III}, measured to be 104 pm, which is extremely close to that of Ho^{III}. [19] Taking advantage of this similarity and the effects of lanthanide contraction, it allows us to do displacements with Y^{III} to several later lanthanide ions with minimal distortion on the structure. Plus the diamagnetic property of Y^{III}, can yield valuable information using NMR and magnetism studies for lanthanide complexes by introducing this diamagnetic host lattice. [20] For example, by increasing the dilution ratio in $[LnPc_2]^-$ complexes, the removal of the dipolar interactions between the nearest Ln^{III} ions has been observed and as a result the anisotropy barriers were raised as well. [9, 21]

In chapter 4, a series of dinuclear complexes including Gd, Dy, Ho, Er and Yb will be described to exhibit the lanthanide contraction property. Instead of comparing the ionic radii directly, the contraction effects on the average bond distances of the coordination polyhedron and core atoms distances are probed.

1.2.3 The Utilization of Gd^{III}, Tb^{III} and Dy^{III} in Building SMMs

1.2.3.1 Gd^{III}

For the gadolinium (III) ion, its electronic configuration is f^7 and possesses an $^8S_{7/2}$ singlet ground state. This causes entirely different properties for Gd^{III} than the other Ln^{III} ions which have strong unquenched orbital angular momentum and effective spin-orbit coupling. The isotropic nature of Gd^{III} allows the probing of the magnetic interaction of gadolinium-containing compounds by applying the Van Vleck equation to Kambe's vector coupling scheme.

1.2.3.2 Tb^{III} and Dy^{III}

There are two requirements to fulfill in building strong single-ion anisotropy: first, the ground state should be bistable and have a large value of m_J, which maintains a substantial magnetic moment; second, a large separation between ground and first excited m_J level, which defines the energy required to relax and spin. [13] Under these restrictions, terbium (III) and dysprosium (III) stand out with their intrinsic large anisotropy. A tremendous

number of Tb-SMMs and Dy-SMMs have been explored, outnumbering the rest of the Ln^{III} ions. It is clear that, compared to Dy^{III} based SMMs, Tb^{III} containing SMMs are much less common, however, some Tb^{III}-SMMs have the highest anisotropic barriers in the field. [23] The reasons for both features can be explained by their 4*f* configuration. The Dy^{III} ion is a Kramers' ion thus it will always maintain a degenerate ground state, while Tb^{III} can have a larger gap between ground and first excited m_J level but an axial symmetry of the ligand field is necessary to maintain its bistable ground state. [9, 13]

1.3 Modelling Ln-SMMs

The utilization of lanthanides for the construction of single-molecule magnets has rapidly expanded this field with their intrinsic magnetic properties. [24] For building the desired anisotropy which is the basic requirement for strong SMMs, it is of vital importance to understand the nature and strength of interactions between lanthanide ions. Herein, by presenting some important Ln-SMM systems, we expect to have a good understanding of the reasons behind their fascinating properties.

1.3.1 Mononuclear Phthalocyanine Double-Decker Complexes

In 2003, Ishikawa and co-workers described mononuclear phthalocyanine double-decker complexes $[Pc_2Dy]^-•TBA^+$ and $[Pc_2Tb]^-•TBA^+$ ($TBA^+ = N(C_4H_9)_4^+$). [9] This work started a new era for lanthanide SMMs by showing their huge potential benefitting from single-ion anisotropy. [24b] The Tb^{III} complex exhibits slow relaxation of the magnetization below 50 K and by doping into diamagnetic $[Pc_2Y]^-•TBA^+$ ensured that the slow magnetization relaxation behavior is a single-molecule property instead of intermolecular interactions and/or long-range ordering. Furthermore, the occurrence of QTM in these complexes has been shown by performing hysteresis loop measurements at sub-kelvin temperatures. [25] And this QTM for lanthanide SMMs was concluded to be a fundamentally different mechanism from the one for transition metal SMMs, which should arise from entangled states of nuclear and electronic spin. [25]

1.3.2 Dinuclear Ln-SMMs Systems

In our research we mainly focus on dinuclear systems which represent the simplest molecular units for studying magnetic interactions between two spin carriers. [24] The alignment of anisotropy axes can be influenced by molecular symmetry, the coordination sphere as well as the bridging ligands which play the role of superexchange pathways. [26]

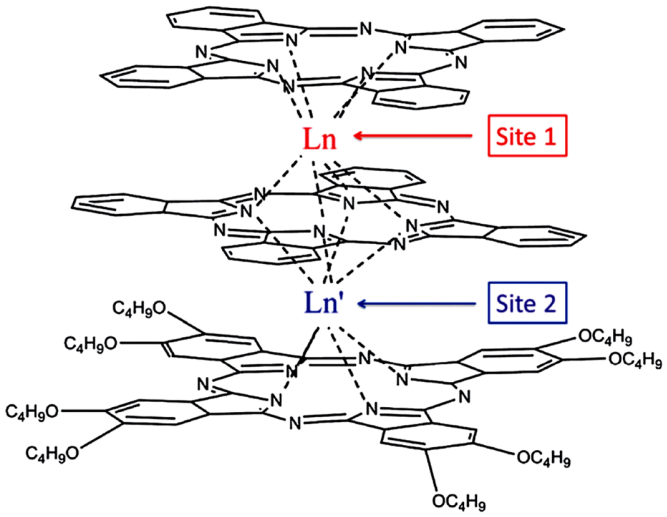

Figure 1.3 Schematic diagram of a triple-decker complex. [10] Doping studies involved the synthesis of analoguous heterodinuclear complexes PcLnPcYPc$(OC_4H_9)_8$ with Ln = Tb, Dy, Ho, Er, Tm and Yb, and Ln' = Y. For homodinuclear complexes PcLnPcLnPc$(OC_4H_9)_8$, Ln = Ln' = Tb, Dy, Ho, Er, Tm and Yb. (Adapted from **Ref. 10.** Copyright 2002 American Chemical Society.)

Expanding on the previously mentioned phthalocyanine double-decker complexes to triple-decker format, Ishikawa and co-workers successfully provided us the simplest model with two interaction modes which allowed the study of exchange coupling between 4*f* ions. [27] To investigate the net contribution of *f-f* interaction in the homodinuclear complexes, heterodinuclear complexes composed of a diamagnetic Y^{III} and a paramagnetic Ln^{III} ion were prepared (Figure 1.3). As for determining the ligand field (LF) parameters and elucidating splitting structures of the ground-state multiplets, ^1H NMR spectra as well as magnetic susceptibility measurements were performed on these heterodinuclear complexes. [28] Some interesting discussions were carried out afterwards. The extracted

magnetic susceptibility of [Ln, Ln] complexes were different for Dy^{III}, Tb^{III} and Ho^{III} where the presence of ferromagnetic interactions were observed; while for Er^{III} the interaction became antiferromagnetic. Additionally, [Tm, Tm] displayed uncommon behavior and only a very small interaction was found in [Yb, Yb]. [28] In order to answer these questions, theoretical calculations using the LF parameters [28] were performed, revealing that the nature of the magnetic interaction between the dinuclear *f*-systems is essentially dipolar. Compared to that, the contribution of the exchange interaction term was nearly negligible. For the ferromagnetic cases, the enlarged χ_z dominated over $\Delta\chi_x$ and $\Delta\chi_y$ leading to a net increase in $\Delta\chi_m$ with a positive value. The $\Delta\chi_z$ for [Tb, Tb] was the largest among the six systems which further led to the maximum $\Delta\chi_m$ value. [27] On the contrary, the antiferromagnetically coupled Er^{III} system gained an overall negative $\Delta\chi_m$ value since the $\Delta\chi_x$ and $\Delta\chi_y$ were more significant here. This also was the case for Tm^{III} analogue, except a relatively smaller susceptibility value was observed. At the end, for Yb^{III} the closed surfaces are more spherical which produced a nearly isotropic magnetic susceptibility with $\Delta\chi_m$ of zero. This work provided a tool to study the electronic structures of mono- or dinuclear Ln-SMMs, as well as a strategy to design new SMMs with higher energy barriers. [26, 27]

For dinuclear Ln-SMMs, different bridging atoms/moieties between the metal centers have vital influence on the overall magnetic properties of the complexes. Through the investigation of different bridging groups, we may be able to determine the origin of the *f-f* interactions and extend our knowledge in designing new SMMs with better properties. Based on our research interests and the available resources, herein our discussion is mainly focused on oxygen-bridged molecules.

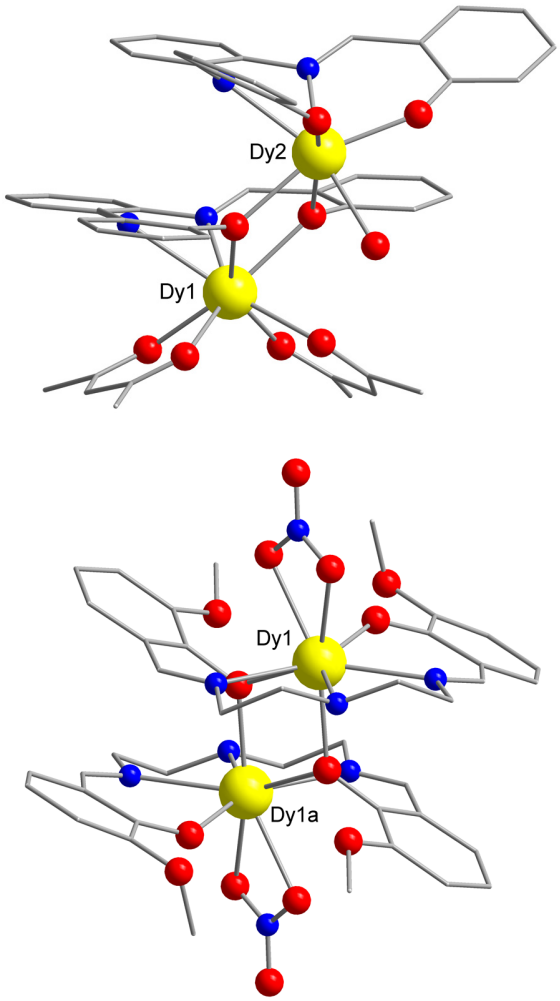

Figure 1.4 Molecular structures of **top**: $[Dy^{III}_2(\mathbf{L})_2(acac)_2(H_2O)]\cdot 2CH_2Cl_2$, and **bottom**: $Ln^{III}_2(\mathbf{L2})_2(NO_3)_2$ (Ln = Eu, Gd, Tb, Dy, Ho). Color code: yellow (Dy), red (O), blue (N) and grey (C). Hydrogen atoms and solvent molecules have been omitted for clarity.

Asymmetric complex $[Dy^{III}_2(\mathbf{L})_2(acac)_2(H_2O)]\cdot 2CH_2Cl_2$, where Schiff base ligand $H_2\mathbf{L}$ = N,N-bis(salicylidene)-*o*-phenylenediamine (Figure 1.4, top), was synthesized and found to crystallize in the monoclinic $P2_1/c$ space group. [29] The two Dy^{III} centers are eight-coordinated and seven-coordinated bridged through the phenol oxygen atoms. The magnetic measurements revealed a weak ferromagnetic coupling in this system, and two slow relaxation processes were obtained under a 1000 Oe applied field. The two relaxation processes might be due to the distinct coordination environments and geometries of the two Dy^{III} centers. The obtained effective energy barriers were 36 K ($\tau_0 = 4.2*10^{-7}$ s) and 80 K

(τ_0 = 8.3*10^{-8} s), respectively. Another interesting phenoxide-oxygen-bridged series of dinuclear complexes with a general formula of Ln^{III}_2(**L2**)$_2$(NO_3)$_2$ (Ln = Eu, Gd, Tb, Dy, Ho), where H_2**L2** = *N*1,*N*3-bis(3-methoxysalicylidene)diethylenetriamine (Figure 1.4, bottom), were explored by our group recently. [30] The observed weak antiferromagntic coupling in the Dy^{III} analogue was confirmed by both *ab initio* calculations with a $J_{Dy\text{-}Dy}$ = -0.21 cm^{-1} and the quantified coupling constant from its Gd^{III} analogue where $J_{Gd\text{-}Gd}$ = -0.18 cm^{-1}. The bridging phenol groups here acted as superexchange pathways between the metal centers which is consistent with other systems. [31] The Dy^{III} analogue revealed SMM behavior with an obtained barrier of 76 K where τ_0 = 6.0*10^{-7} s.

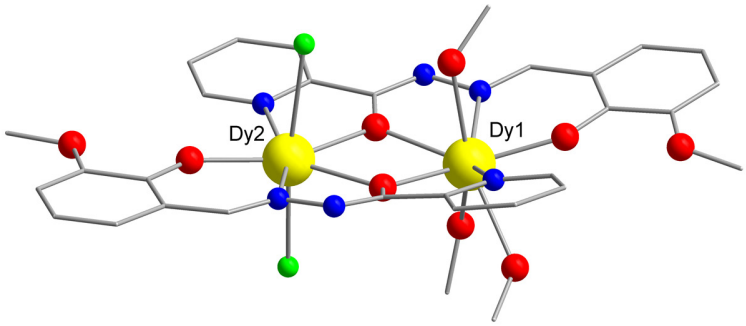

Figure 1.5 Molecular structure of complex [Dy^{III}_2(ovph)$_2$$Cl_2$($MeOH$)$_3$]·MeCN. Color code: yellow (Dy), red (O), blue (N) and grey (C). Hydrogen atoms and solvent molecules have been omitted for clarity.

Even though keeping "the same" feature of the bridging groups along with oxygen atoms, different source of those oxygen atoms may cause a significant difference in the behavior of the complexes. The study of complex [Dy^{III}_2(ovph)$_2$$Cl_2$($MeOH$)$_3$]·MeCN [32] ($H_2$ovph = 2-hydroxy-3-methoxybenzaldehyde (pyridine-2-carbonyl) hydrazone) (**Ref-1** in chapter 2, Figure 1.5) which we took as a parent compound for the studies in chapter 2 and 3 will be presented as an example here. This alkoxide-oxygen-bridged asymmetric dinuclear Dy^{III} complex was found to be ferromagnetically coupled, and the magnetization studies revealed the presence of significant magnetic anisotropy. A micro-SQUID technique was applied to this system and showed two-step hysteresis cycle below 1.5 K. At the meantime, by decreasing temperature, the coercity increased significantly, which suggested a slow tunneling rate with a characteristic time of τ_{QTM} = 35 s. Detailed

computational studies implied that the local anisotropy axes and the Dy…Dy axis were being aligned almost in parallel to each other. The strong ferromagnetic interaction between the two dysprosium ions was calculated to be J = 5.88 cm^{-1}, of which the dipolar contribution was J_{dip} = 5.36 cm^{-1} and consequently the pure exchange contribution was J_{exch} = 0.52 cm^{-1}. Therefore, the observed ferromagnetic coupling was mainly originating from a dipolar interaction. The ac susceptibility measurements on this asymmetric {Dy_2} complex featured two different relaxation processes, and the resulting effective energy barriers were U_{eff} = 150 K ($\tau_0 = 2.3*10^{-8}$ s) and 198 K ($\tau_0 = 7.3*10^{-9}$ s) for the fast relaxation and slow relaxation phases, respectively.

Generally, oxygen based bridges are more common in the construction of Ln-SMMs. This is mainly due to the easier synthesis and multi bridging ability nature of the oxygen atoms which also provide potential superexchange pathways. [26] Ln-SMMs with N-based, [33a] S-based [33b] and Cl bridges [33c] were also investigated with the aim of looking for stronger magnetic interactions, detailed information can be obtained from the corresponding literature references.

1.3.3 Polynuclear SMMs (three or more metal ions involved)

Recently, inspired by some fourfold symmetrical SMMs with fascinating physics such as $[Pc_2Tb]^-•TBA^+$ ($TBA^+ = N(C_4H_9)_4^+$) [9] and $Na_9[Er(W_5O_{18})_2]$, [34] as well as the triangular array {Dy_3} cage with unusual spin chirality, [35] Winpenny and co-workers focused on synthesizing a molecule with both properties. The resulting *iso*-propoxide-bridged dysprosium complex [$Dy_5O(O$*i*$Pr)_{13}$] is shown in Figure 1.6, exhibiting disordered square-based pyramid geometry. [36] Though the structure has no crystallographic symmetry, each Dy site has local C_4 symmetry. The magnetism studies revealed a possible weak antiferromagnetic interaction and/or depopulation of the Dy^{III} ions excited Stark sublevels upon cooling. [37] The relaxation process was monitored under a large temperature range (3-56 K) at zero static field, and by fitting with Arrhenius law gave a thermal energy barrier of 530 K with $\tau_0 = 4.7*10^{-10}$ s. A very narrow hysteresis was observed at 1.8 K which might be due to the existence of QTM at lower temperatures. However, some minor features also suggested a second thermally activated relaxation process below 12 K within

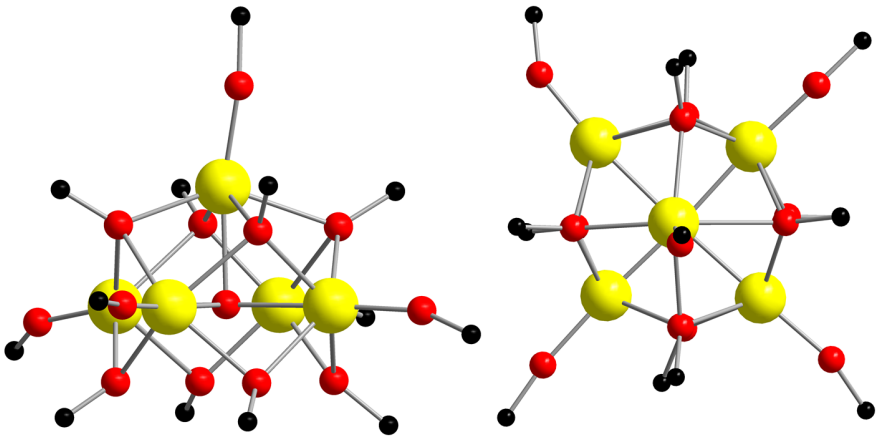

Figure 1.6 Molecular structure of $[Dy_5O(O^iPr)_{13}]$ from perpendicular (left) and parallel to the pseudo-fourfold axis (right) view. Color code: yellow (Dy), red (O) and black (*i*Pr groups).

the quantum tunneling region of the first process with an estimated barrier of 32 K and $\tau_{0(2)} = 3.8*10^{-6}$ s. This molecule revealed the second largest barrier ever to be reported, and the only family of complexes with a higher barrier are $[Pc_2Tb]^{n-}$ [8] which also exhibit fourfold symmetry crystal field on the 4f-centers. Therefore, Winpenny and co-workers believed that the symmetry was important in these systems, and the magnetic properties are mainly dominated by single ions.

Interestingly, this intriguing pentametallic dysprosium complex $[Dy_5O(O^iPr)_{13}]$ was expanded to other late lanthanides afterwards, Dy^{III} ion was substituted with Sm, Gd, Tb, Ho and Er. [38] Though various crystal systems were observed for these clusters, the core structure $\{Ln_5\}$ was inherited and each Ln site kept the approximate fourfold symmetry which was hypothesized as crucial to the enhancement of single-ion anisotropy. [36] Nevertheless, neither the isostructural terbium or erbium analogues, representing non-Kramers' ion and Kramers' ion separately, showed any SMM nature. On the contrary, the $\{Ho_5\}$ presented frequency dependent out-of-phase signals with a maximum under an applied field of 3500 and 5500 Oe, the effective anisotropic barrier was determined to be $U_{eff} = 400$ K ($\tau_0 = 1.5*10^{-9}$ s) at both dc-fields (Figure 1.7). This also suggested an efficient QTM in zero applied field which most likely due to hyperfine interactions and co-tunneling events with adjacent neighboured ions, as commonly observed in Ho^{III} based complexes.

[39] This work was only the third Ho-SMM ever reported, [39, 40] and the first polymetallic example. Both of the Dy and Ho analogues showed huge potential in the [$Ln_5O(O^iPr)_{13}$] family of complexes which may deserve more investigation.

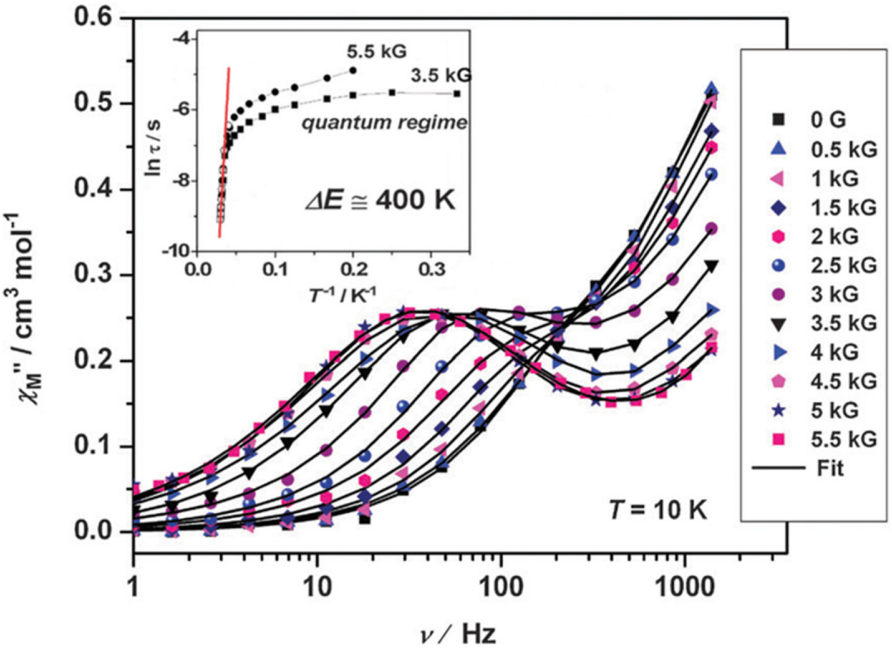

Figure 1.7 Out-of-phase magnetic susceptibility of [$Ho_5O(O^iPr)_{13}$] at 10 K under indicated dc fields. Inset: Arrhenius plot based on ac data collected at 3500 and 5500 Oe, fitted with data above 24 K.

1.4 Schiff Base-SMMs

Schiff base ligands have been widely used for the purpose of synthesizing Ln-SMMs. [29-32] The growing interest in lanthanide SMMs leads to huge focus on ligand development, since the coordination environment is the main factor in the complex properties. Generally, Schiff base ligands are derived from aromatic aldehydes and alkyl diamines, reactions commonly taking place in alcohol through condensation. [41] The straight forward synthesis could be one of the reason that Schiff base ligands are so popular, and also the basic imine nitrogen which exhibits pi-acceptor property shows affinity to Ln^{III} ions making it the preferred choice.

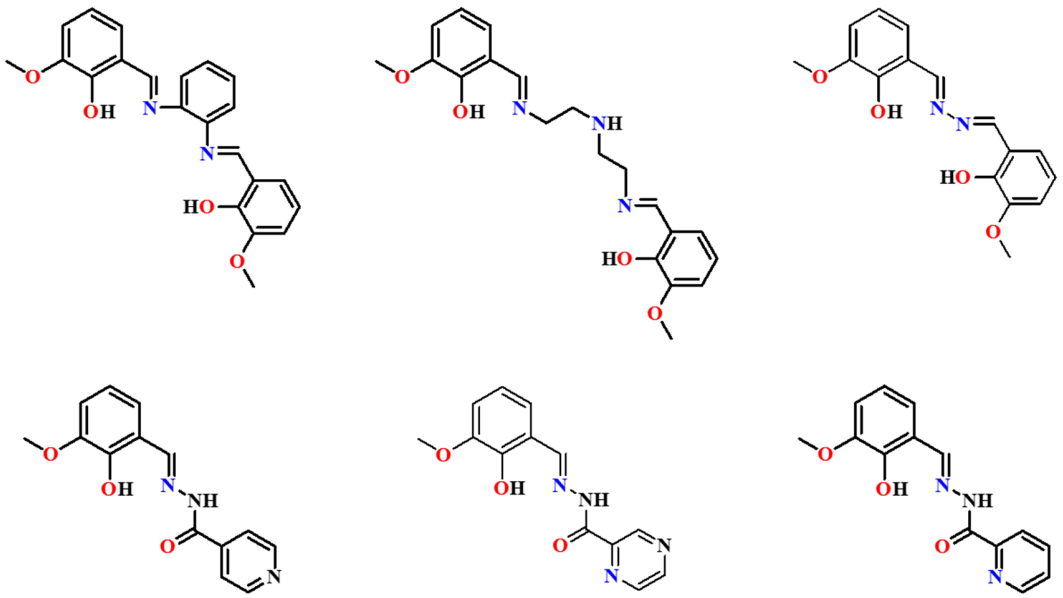

Figure 1.8 Ligand structures of selected Schiff base H_2**L1**- H_2**L5** and H_2ovph (left to right from top to bottom).

Additionally, the Schiff base ligands can be easily modified by using different aldehyde and diamine components. For instance, by controlling the diamines with different sizes, flexibility and basicity, [42] which provides different "pockets" for Ln^{III} ions to occupy, we can target dinuclear, trinuclear, tetranuclear and even more ploynuclear structures. [43] Additionally, the flexibility of the diamines or the linkers potentially introduces chirality to the complex by increasing the chance of forming helicate or mesocate structures. [44]

O-vanillin derived Schiff base ligands have proven to be particularly suitable for the synthesis of Ln-SMMs, [30, 32, 43c, 43d, 45] some previously used ligands are shown in Figure 1.8. With H_2**L1**, pure Schiff base and phthalocyanine ligand mixed sandwich-type lanthanide triple-decker complexes [Ln_2(**L1**)$_3$(H_2O)] and [Ln_2(Pc)$_2$(**L1**)(H_2O)] (Ln = Dy, Gd) was prepared. [45a] Also the previously mentioned symmetric ligand H_2**L2** with two *o*-vanillin moieties, provided an extra N donor and a more flexible linker which resulted in five isostructural dinuclear complexes [Ln^{III}_2(**L2**)$_2$(NO_3)$_2$] (Ln = Eu, Gd, Tb, Dy, Ho). [30] Each metal center was "independently" surrounded by one ligand with 3 N and 2 O atoms from the amine moieties and phenol groups, respectively, with metal-metal bridging by the -OMe groups. On the contrary, shorter linkers, such as H_2**L3**, [43b] changed the arrangement

to a "sharing" ligand type: each ligand provided two pockets for Ln^{III} ions and formed a centrosymmetric tetranuclear complex as a result. Previous studies reveal that the bridging group is crucial in lanthanides systems in order to overcome the core nature of 4*f* orbitals and also to induce significant exchange interactions between the paramagnetic centers." [30]

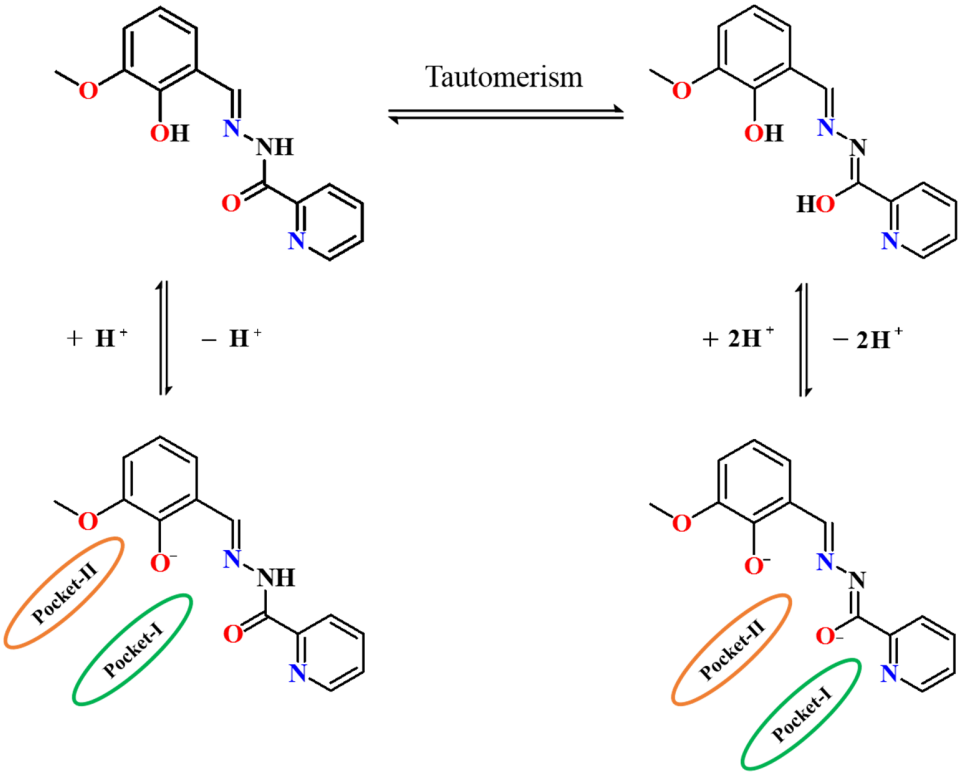

Figure 1.9 The keto-enol tautomerism of H_2**L6** (H_2ovph) and observed coordination pockets with different bridging modes.

Furthermore, the introduction of H_2**L4**, [45b] H_2**L5** [43c] and H_2ovph [32] synthesized by the condensation of *o*-vanillin and the corresponding hydrazide allowed for the study of the effects of different bridging groups on intramolecular interactions. Under different synthetic methods, the preference of the bridging atoms changed from *o*-vanillin derived phenol groups to the hydrazide provided keto- or enol oxygen atoms. [46] The N atoms from pyridine or pyrazine rings also helped transform the bridging groups by being involved in the coordination in H_2**L5** and H_2ovph cases. Among all these ligands, H_2ovph caused us more concern due to its multi bridging modes. Figure 1.9 demonstrates the known coordination pockets for this ligand. [32, 46]

1.5 Thesis Overview and Research Objectives

This thesis describes the synthesis, characterization and magnetic investigation of homometallic lanthanide complexes based on two different *o*-vanillin-derived Schiff base ligands. The research results are presented in the following three chapters. Chapter 2 focuses on dinuclear systems with description of the synthetic method, crystal structures and magnetic properties, mainly with respect to their intramolecular interactions. Chapter 3 describes two hexanuclear systems with trigonal prism-assembled core structure. Other than introducing the structure and magnetic properties of our complexes, we also perform a comparison to similar architectures in literature. Chapter 4 focuses on a series of dinuclear complexes, and shows the studies of their synthetic approaches, crystal structures and magnetism. The presence of the contraction result in this system of complexes is consistent with the intrinsic lanthanide contraction property.

The synthetic methods of lanthanide coordination chemistry have been well established, however, it is still not easy to control the key parameters in an existing system to improve its SMMs properties. This is due to the difficulties in controlling the arrangement of the metal centers, the magnetic coupling between them and the orientations of single-ion anisotropy axes. To minimize the difference in structure which influences those factors significantly, we adopt a widely-used Schiff-base ligand H_2ovph (chapter 2 and 3). The newly designed complexes are more comparable to those previously reported examples within the same ligand group than the other systems. We can possibly monitor the change in structures and, consequently, the influence on the magnetic behaviors. In this thesis, two *o*-vanillin-derived Schiff-base ligands are used for the purpose of studying new SMMs with improved properties.

1.6 References

[1] S. K. Ritter. *Chem. Eng. News.*, **2004**, *50*, 29-32.

[2] R. Sessoli, D. Gatteschi, A. Caneschi, M. A. Novak. *Nature,* **1993**, *365*, 141-143.

[3] T. Lis. *Acta. Cryst.,* **1980**, *B36,* 2042-2046.

[4] (a) A. Caneschi, D. Gatteschi, R. Sessoli, A. L. Barra, L. C. Brunel, M. Guillot, *J. Am. Chem. Soc.,* **1991**, *113*, 5873-5874. (b) R. Sessoli, H.-L. Tsai, A. R. Schake, S. Wang, J. B. Vincent, K. Folting. D. Gatteschi, G. Christou, D. N. Hendrickson, *J. Am. Chem. Soc.,* **1993**, *115*, 1804-1816.

[5] L. Thomas, F. Lionti, R. Ballou, D. Gatteschi, R. Sessoli, B. Barabara. *Nature,* **1996**, *383*, 145-147.

[6] J. R. Friedman, M. P.Sarachik, J. Tejada, R. Ziolo. *Phys. Rev. Lett.,* **1996***, 76,* 3830–3833.

[7] (a) W. Wernsdorfer, R. Sessoli. *Science,* **1999***, 284,* 133–135. (b) W. Wernsdorfer. *Nature Materials,* **2007**, *6*, 174-176.

[8] (a) C. R. Ganivet, B. Ballesteros, G. de la Torre, J. M. Clemente-Juan, E. Coronado, T. Torres. *Chem. Eur. J.,* **2013**, *19*, 1457-1465. (b) R. A. Layfield. *Organometallics,* **2014**, *33*, 1084-1099.

[9] N. Ishikawa, M. Sugita, T. Ishikawa, S. Koshihara, Y. Kaizu. *J. Am. Chem. Soc.,* **2003**, *125*, 8694-8695.

[10] D. Gatteschi, R. Sessoli. *Angew. Chem. Int. Ed.,* **2003**, *42*, 268-297.

[11] (a) *Quantum Tubbeling of Magnetization-QTM 94*. (Eds.: L. Gunther, B. Barbara), **1995**, Kluwer, Dordrecht. (b) E. M. Chudnovsky, J. Tejada. *Macroscopic Quantum Tunneling of the Magnetic Moments,* **1998***,* Cambridge University Press, Cambridge. (c) P. C. P. Stamp, E. M. Chudnovsky, B. Barbara. *Int. J. Mod. Phys. B.,* **1992**, *6*, 1355-1473.

[12] (a) A. Fort, A. Rettori, J. Villain, D. Gatteschi, R. Sessoli. *Phys. Rev, Lett.,* **1998**, *80,* 612-615. (b) D. A. Garanin, E. M. Chudnovsky. *Phys. Rev. B*., **1997**, *56*, 11102-11118. (c) M. N. Leuenberger, D. Loss. *Europhys. Lett.,* **1999**, *46,* 692-698. (d) M. N. Leuenberger, D. Loss. *Phys. Rev. B*., **2000**, *61*, 1286-1302. (e) F. Luis, J. Bartolomé, J. F. Fernàndez. *Phys. Rev. B*., **1998**, *57*, 505-513. (f) T. Pohjola, H. Schoeller. *Phys. Rev. B*., **2000**, *62*, 15026-15041. (g) J. R. Friedman. *Phys. Rev. B*., **1998**, *57*, 10291-10294.

[13] J. D. Rinehart, J. R. Long. *Chem. Sci.,* **2011**, *2*, 2078-2085.

[14] D. N. Woodruff, R. E. P. Winpenny, R. A. Layfield. *Chem. Rev.*, **2013**, *113*, 5110-5148.

[15] A. K. Ako, I. J. Hewitt, V. Mereacre, R. Clérac, W. Wernsdorfer, C. E. Anson, A. K. Powell. *Angew. Chem. Int. Ed.,* **2006**, *45*, 4926-4929.

[16] C. H. Huang. *Rare Earth Coordination Chemistry: Fundamentals and Applications.* **2010**, John Wiley & Sons (Asia) Pte Ltd., Singapore.

[17] A. Abragam, B. Bleaney. *Electron Paramagnetic Resonance of Transition Ions,* **2012**, Oxford Universtiy Press, New York.

[18] M. Nakano, H. Oshio. *Chem. Soc. Rev.*, **2011**, *40*, 3239-3248.

[19] R. D. Shannon. *Acta. Cryst.*, **1976**, *A32*, 751-767.

[20] S. Cotton. *Lanthanide and Actinide Chemistry*, **2013**, John Wiley & Sons, Rutland, UK.

[21] N. Ishikawa, M. Sugita, W. Wernsdorfer. *Angew. Chem. Int. Ed.,* **2005**, *124,* 3650-3653.

[22] C. H. Huang. *Coordination Chemistry of Rare Earth Complexes*, **1997**, Science Press, Beijing.

[23] (a) N. Ishikawa, S. Otsuka, Y. Kaizu. *Angew. Chem. Int. Ed.,* **2005**, *44*, 731-733. (b) F. Branzoli, P. Carretta, M. Filibian, G. Zoppellaro, M. J. Graf, J. R. Galan-Mascaros, S. Brink, M. Ruben. *J. Am. Chem. Soc.,* **2009**, *131*, 4387-4396. (c) M. Gonidec, D. Amabilino, J. Veciana. *Dalton Trans.,* **2012**, *41*, 13632-13639. (d) S. Takamatsu, N. Ishikawa. *Polyhedron,* **2007**, *26*, 1859-1862. (e) M. Gonidec, F. Luis, A. Vilchez, J. Esquena, D. B. Amabilino, J. Veciana. *Angew. Chem. Int. Ed.,* **2010**, *49,* 1623-1626.

[24] (a) J. -C. G. Bünzli, *Acc. Chem. Res.,* **2006**, *39*, 53-61. (b) L. F. Chibotaru, L. Ungur, A. Soncini, *Angew. Chem. Int. Ed.*, **2008**, *47*, 4126-4129.

[25] N. Ishikawa, M. Sugita, W. Wernsdorfer. *Angew. Chem. Int. Ed.,* **2005**, *44,* 2931-2935.

[26] F. Habib, M. Murugesu. *Chem. Soc. Rev.,* **2013**, *42*, 3278-3288.

[27] N. Ishikawa, T. Iino, Y. Kaizu. *J. Am. Chem. Soc.,* **2002**, *124*, 11440-11447.

[28] N. Ishikawa, T. Iino, Y. Kaizu. *J. Phys. Chem. A*., **2002**, *106*, 9543-9550.

[29] P. H. Lin, W. B. Sun, P. F. Yan, L. Ungur, L. F. Chibotaru, M. Murugesu. *Chem. Commun.*, **2011**, *47*, 10993-10995.

[30] J. Long, F. Habib, P. H. Lin, I. Korobkov, G. Enright, L. Ungur, W. Wernsdorfer, L. F. Chibotaru, M. Murugesu. *J. Am. Chem. Soc.*, **2011**, *133*, 5319-5328.

[31] P. H. Lin, T. J. Burchell, R. Clérac, M. Murugesu. *Angew. Chem.,* **2008**, *120*, 8980-8983.

[32] Y. N. Guo, G. F. Xu, W. Wernsdorfer, L. Ungur, Y. Guo, J. K. Tang, H. J. Zhang, L. F. Chibotaru, A. K. Powell. *J. Am. Chem. Soc.,* **2011**, *133*, 11948-11951.

[33] (a) R. A. Layfield, J. W. McDouall, S. A. Sulway, F. Tuna, D. Collison, R. E. P. Winpenny. *Chem.–Eur. J*., **2010**, *16*, 4442-4446. (b) S. A. Sulway, R. A. Layfield, F. Tuna, W. Wernsdorfer, R. E. P. Winpenny. *Chem. Commun.,* **2012**, *48*, 1508-1510. (c) J. D. Rinehart, T. D. Harris, S. A. Kozimor, B. M. Bartlett, J. R. Long. *Inorg. Chem.,* **2009**, *48*, 3382-3395.

[34] M. A. AlDamen, J. M. Clemente-Juan, E. Coronado, C. Martí-Gastaldo, A. Gaita-Ariño. *J. Am. Chem. Soc*., **2008**, *130*, 8874 –8875.

[35] (a) J. K. Tang, I. Hewitt, N. T. Madhu, G. Chastanet, W. Wernsdorfer, C. E. Anson, C. Benelli, R. Sessoli, A. K. Powell, *Angew. Chem*., **2006**, *118*, 1761–1765; *Angew. Chem. Int. Ed*., **2006**, *45*, 1729–1733. (b) J. Luzon, K. Bernot, I. J. Hewitt, C. E. Anson, A. K. Powell, R. Sessoli, *Phys. Rev. Lett*., **2008**, *100*, 247205/1-247205/4.

[36] R. J. Blagg, C. A. Muryn, E. J. L. McInnes, F. Tuna, R. E. P. Winpenny. *Angew. Chem. Int. Ed.,* **2011**, *50*, 6530-6533.

[37] L. Sorace, C. Benelli, D. Gatteschi. *Chem. Soc. Rev.,* **2011**, *40*, 3092-3104.

[38] R. J. Blagg, F. Tuna, E. J. L. McInnes, R. E. P. Winpenny. *Chem. Commun.,* **2011**, *47*, 10587-10589.

[39] N. Ishikawa, M. Sugita, W. Wernsdorfer. *J. Am. Chem. Soc.,* **2005**, *127*, 3650-3651.

[40] M. A. AlDamen, S. Cardona-Serra, J. M. Clemente-Juan, E. Coronado, A. Gaita-Ariño, C. Martí-Gastaldo, F. Luis, O. Montero. *Inorg. Chem.,* **2009**, *48*, 3467-3479.

[41] (a) D. N. Dhar, C. L. Taploo. *J. Sci. Ind. Res.,* **1982**, *41*, 501-506.

[42] (a) R. G. Pearson. *J. Am. Chem. Soc.,* **1963**, *85*, 3533-3543. (b) R. G. Pearson. *J. Chem. Educ.,* **1968**, *45*, 581-587.

[43] (a) M. U. Anwar, L. K. Thompson, L. N. Dawe, F. Habib, M. Murugesu. *Chem. Commun.,* **2012**, *48*, 4576-4578. (b) Y. N. Guo, G. F. Xu, P. Gamez, L. Zhao, S. Y. Lin, R. P. Deng, J. K. Tang, H. J. Zhang. *J. Am. Chem. Soc.,* **2010**, *132*, 8538-8539. (c) H. Q. Tian, L. Zhao, Y. N. Guo, Y. Guo, J. K. Tang, Z. L. Liu. *Chem. Commun.,*

2012, *48*, 708-710. (d) Y. N. Guo, X. H. Chen, S. F. Xue, J. K. Tang. *Inorg. Chem.,* **2012**, *51*, 4035-4042.

[44] (a) F. Habib, J. Long. P. H. Lin, I. Korobkov, L. Ungur, W. Wernsdorfer, L. F. Chibotaru, M. Murugesu. *Chem. Sci.*, **2012**, *3*, 2158-2164. (b) A. Lalehzari. Thesis title "Preparation of chiral acid-functionalized Shciff-base ligands and their complexation with divalent transition metals: the story of helices and cubanes", **2007**, Kansas state university, Manhattan, Kansas.

[45] (a) H. L. Wang, C. X. Liu, T. Liu, S. Y. Zeng, W. Cal, Q. Ma, C. Y. Duan, J. M. Dou, J. Z. Jiang. *Dalton Trans.,* **2013**, *42*, 15355-15360. (b) P. H. Lin, T. J. Burchell, R. Clérac, M. Murugesu. *Angew. Chem.,* **2008**, *47*, 8848-8851.

[46] (a) Y. N. Guo, X. H. Chen, S. F. Xue, J. K. Tang. *Inorg. Chem.,* **2011**, *50*, 9705-9713. (b) L. F. Zou, L. Zhao, P. Chen, Y. N. Guo, Y. Guo, Y. H. Li, J. K. Tang. *Dalton Trans.,* **2012**, *41*, 2966-2971.

Chapter 2

Probing the Origin of Ferromagnetism in Dinuclear Lanthanide Complexes

2.1 Bimetallic Ln-SMMs

Lanthanide-based SMMs have been drawing extensive attention during the past decades. The investigation of the intramolecular interactions between metal centers for polynuclear lanthanide complexes could be a very challenging topic, and also represents a fundamental step to gaining a better understanding of the field. Unlike d-block SMMs, the exchange coupling in polymetallic lanthanide compounds is not well-understood. Starting from dinuclear systems could be the best option for us since they are less sophisticated but contain vital information. Some great pioneers who worked on bimetallic SMMs provided us with a lot of information and possibly hints to design new SMMs. As a class of their own, the bimetallic salts $[K(18\text{-crown-6})(THF)_2][Ln_2\{N(SiMe_3)_2\}_4(THF)_2(\mu{:}\eta^2{:}\eta^2\text{-}N_2)]$ [1] (Ln = Gd, Tb, Dy, Ho, Er) have a huge intramolecular exchange coupling constant of J = -27 cm^{-1} which is mainly due to the diffuse spin of an N_2^{3-} radical bridge. A series of triple-decker complexes with a general formula $[Pc^1Ln(\mu\text{-}Pc^2)Ln(Pc^3)]$, [2] demonstrated by Ishikawa and coworkers, allowing us to study the influence of intramolecular *f-f* interactions on dynamic magnetic properties. Besides, with easier synthetic methods as an advantage, Schiff base chemistry has been used extensively in this field. For instance, the weak intramolecular exchange interaction in complex $[Dy_aY_b(valdien)(NO_3)]_2$ [3] has been investigated using magnetic dilution and revealed as small but significant. Variations in the ligand linkers produces helicates $(NEt_4)_2[Dy_2(L^1)_4]((CH_3)_2CO)_{0.25}$, $(NEt_4)_2[Dy_2(L^2)_4](H_2O)(DMF)_{0.5}$ and mesocate $(NEt_4)_2[Dy_2(L^3)_4](Et_2O)_2((CH_3)_2CO)_{1.5}$, [4]

demonstrating that even minute changes on the Dy^{III} coordination sphere can change the orientation of the anisotropy axes significantly. Overall, the understanding of dinuclear Ln-SMMs has being enriched by works focusing on different perspectives.

The range of ligand types used to assemble dinuclear SMMs is somewhat limited, and the μ-bridging interactions are commonly based on *O*-donors: phenolate, carboxylate, and acetylacetonate ligands have proven to be particularly popular scaffolds for constructing SMMs. [5] Among them, a group of complexes with alkoxido oxygen atoms as the bridging atom attracted our attention by their potential regular pattern of ferromagnetic intramolecular interactions. [6-9] As we found out, a large O-Dy-O angle (>110°) seems to be the prerequisite for a ferromagnetically coupled system. To explore and discover the origin of such effect in dinuclear lanthanide complexes with a possible pattern, especially for Dy^{III} ions, H_2ovph has been chosen as the ligand. The selection of hydrazone ligand is especially useful to synthesize ploynuclear Ln^{III} complexes with its multiple N- and O-donors with a strong coordination affinity to lanthanide ions. For the design of low-nuclearity to high-nuclearity clusters, the ligand should allow variable possibilities with its linear structure and provides a good chance to learn magnetic properties of different complexes within similar ligand motifs. Particularly, the coordination chemistry of the ligand H_2ovph, [10] and its derivatives with differing aryl-substituents, has been well established in meticulous works. [6-9] So, it becomes a preferential choice for our project by providing rich potential on structural diversity and, at the same time, well established methods from a synthetic point of view. Nevertheless, Schiff base reactions in coordination chemistry is extremely sensitive and the conditions must be carefully controlled. Some new synthetic techniques are demonstrated here. The benefits of this work are numerous: Not only can new lanthanide SMMs be studied to enrich our knowledge, but also the presence of more examples with alkoxido-bridging group might bring us closer to determining the origin of ferromagnetism in these systems.

2.2 Centrosymmetric Dinuclear System

As a remarkable example, with the presence of extremely large intramolecular interaction (J = 5.88 cm^{-1}), **Ref-1** (reference complex **1**) [7] demonstrates that strong axiality of the

local doublets can be achieved by designing suitable crystal fields on the Dy site(s), which leads to an efficient blocking of magnetization. Taking into account its low symmetry, even slightly adjusting the local environments of each Dy ions would cause entirely different results. To diminish the potentially diverse changes that may be caused by fine-tuning the structure, namely to get a better control on modulation, we would like to focus on centrosymmetric structures first.

2.2.1 Centrosymmetric Dinuclear Lanthanide Systems 1-6

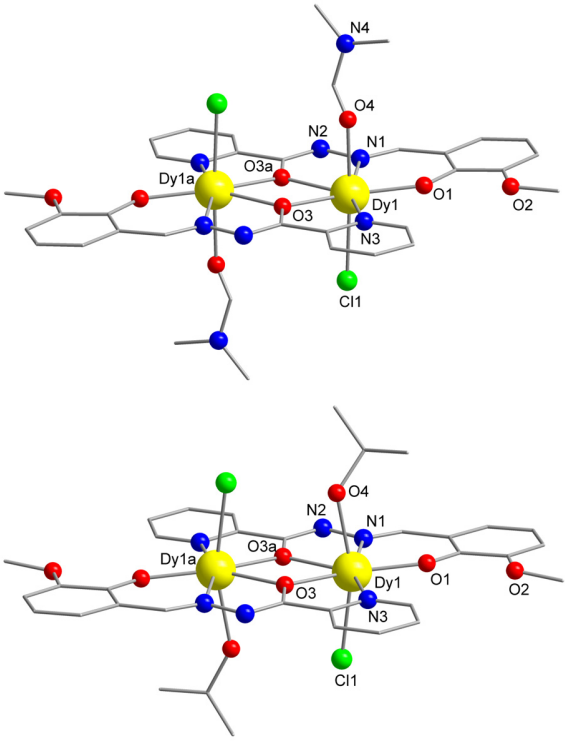

Figure 2.1 Labeled molecular structures of centrosymmetric complexes $[Dy^{III}_2(ovph)_2(DMF)_2Cl_2]$, **1** (top) and $[Dy^{III}_2(ovph)_2(IPA)_2Cl_2]$, **4** (bottom), where H_2ovph = 2-hydroxy-3-methoxybenzaldehyde (pyridine-2-carbonyl) hydrazone. Color code: yellow (Dy), red (O), blue (N), green (Cl) and grey (C). Hydrogen atoms have been omitted for clarity.

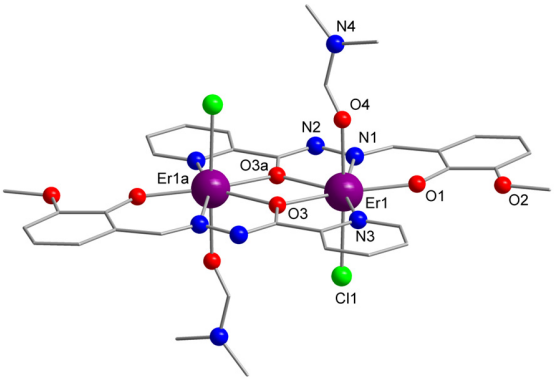

Figure 2.2 Labeled molecular structure of centrosymmetric complex $[Er^{III}_2(ovph)_2(DMF)_2Cl_2]$, **2**, where H_2ovph = 2-hydroxy-3-methoxybenzaldehyde (pyridine-2-carbonyl) hydrazone. Color code: purple (Er), red (O), blue (N), green (Cl) and grey (C). Hydrogen atoms have been omitted for clarity.

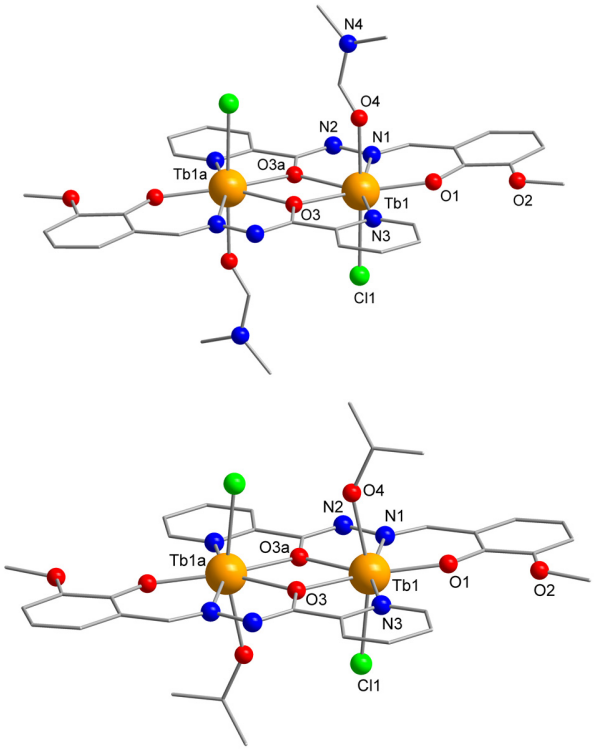

Figure 2.3 Labeled molecular structures of centrosymmetric complexes and $[Tb^{III}_2(ovph)_2(DMF)_2Cl_2]$, **3** (top) and $[Tb^{III}_2(ovph)_2(IPA)_2Cl_2]$, **6** (bottom), where H_2ovph= 2-hydroxy-3-methoxybenzaldehyde (pyridine-2-carbonyl) hydrazone. Color code: orange (Tb), red (O), blue (N), green (Cl) and grey (C). Hydrogen atoms and solvent molecules have been omitted for clarity.

All the synthesis methods are referred to the experimental chapter 6. The single X-ray crystallography studies reveal that complexes **1-3** (Figures 2.1-2.3) are isostructural and crystallize in the monoclinic $P2_1/n$ space group (Table A.1, appendix A). The structure of the dysprosium analogue, complex **1** will be described as an example. The centrosymmetric dinuclear complex is composed of two seven-coordinate Dy^{III} ions bridged by alkoxido groups (O3, O3a) of the $ovph^{2-}$ ligands with a Dy1-O3-Dy1a angle of 113.60(9)° and a Dy···Dy distance equal to 3.8937(3) Å. The central core Dy_2O_2 appears to be nearly rhombic with two Dy-O3 distances being 2.316(2) and 2.337(2) Å. Each asymmetric unit also contains one Cl^- ion and one DMF solvent molecule coordinated to the Dy^{III} ion leading to an overall N_2O_4Cl coordination environment with a Dy1-Cl1 distance of 2.613(1) Å and Dy1-O4 distance of 2.288(4) Å. The heptacoordinated Dy^{III} center exhibits disordered pentagonal bipyramidal coordination environment with a nearly linear O4-Dy1-Cl1 angle equal to 176.2(1)° (Figure 2.5). The shortest intermolecular Dy···Dy distance is 7.5646(3) Å. Despite the isostructurality, small differences exist between the three dinuclear systems (Table 2.1).

Table 2.1 Selected bond distances and angles for complexes **1-4** and **6**.

	1	**2**	**3**	**4**	**6**
Ln-Ln/Å	3.8937(3)	3.8645(3)	3.9280(3)	3.8538(3)	3.8835(4)
Ln1-O3/Å	2.337(2)	2.318(3)	2.360(2)	2.322(4)	2.358(5)
Ln1-O3a/Å	2.316(2)	2.292(2)	2.332(2)	2.317(4)	2.329(5)
Ln1-O4/Å	2.288(4)	2.257(3)	2.302(3)	2.381(3)	2.392(5)
Ln1-Cl1/Å	2.613(1)	2.592(1)	2.6336(8)	2.633(1)	2.638(2)
Ln1-O3-Ln1a/°	113.60(9)	113.9 (1)	113.69(8)	112.4(1)	111.9(2)
O4-Ln1-Cl1/°	176.2(1)	177.0(1)	177.52(7)	163.41(9)	163.5(1)
Packing*/Å	7.5646(3)	7.4934(3)	7.5161(3)	7.7415(3)	7.7940(7)

*The closest intermolecular metal center distance.

Complexes **4-6** (Figure 2.1-2.3) have relatively similar structures to complexes **1-3** but with DMF coordinated solvent being replaced by isopropanol (IPA) molecules, are crystallized in monoclinic $P2_1/n$ space group as well (Table A.1, appendix A). For complex **5**, single crystal X-ray data could not be obtained. However, structure of **5** has been shown to be in good agreement with its isostructural complexes of **4** and **6** by PXRD

measurements. Take complex **4** for example (Figure 2.1, right), the bridging alkoxido groups (O3, O3a) give a Dy1-O3-Dy1a angle of 112.4(1)° with a Dy···Dy metal center distance of 3.8538(1) Å, which are both close to the values of complex **1** (Table 2.1). The coordination sphere of each Dy center consists of two N atoms (N1, N3), four O atoms (O1, O3, O3a) that are provided by the ligands and solvent molecule IPA (O4), and a Cl^- ion that completes the coordination environment. In contrast with the previously described complexes **1-3**, the O4-Dy1-Cl1 angle of complex **4** is considerably smaller with a value of 163.5(1) °. Similar packing scheme was observed between complex **1** and **4** as well, with a shortest Dy···Dy distance equal to 7.7415(3) Å.

The packing schemes of complexes **1** and **4** seem to be similar, however, the existence of hydrogen bonds between chloride ions and the hydrogen atoms from the adjacent non-parallel layer results a tighter structure with the closest distance between two parallel layers being 16.94 Å in complex **4**. The corresponding value for **1** is 17.51 Å. Even from Figure 2.4 which illustrated the packing arrangement, the average metal centers distances are much smaller in **4**. Although the closest intermolecular Dy···Dy distance for **4** is farther, it actually contains higher density throughout the whole packing system.

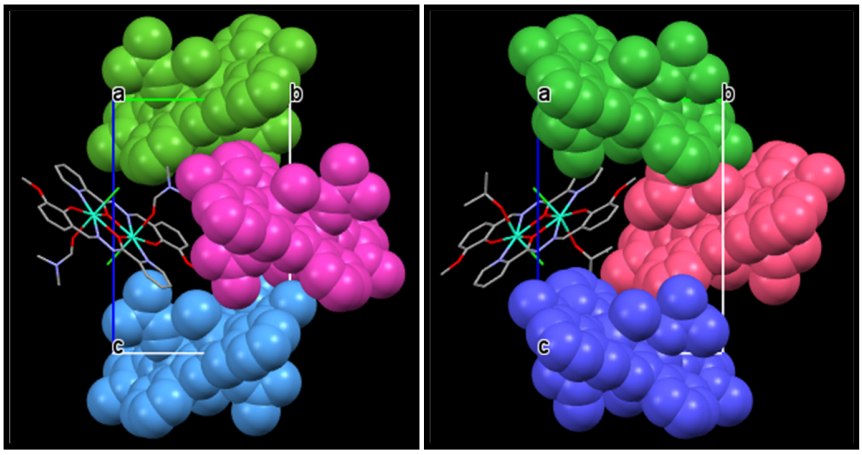

Figure 2.4 Illustration of the packing arrangements of complexes **1** (left) and **4** (right). The shortest metal centers distance for **1**: green-purple-9.42 Å, purple-blue-9.89 Å; for **4**: green-pink-9.31 Å, pink-blue-9.38 Å.

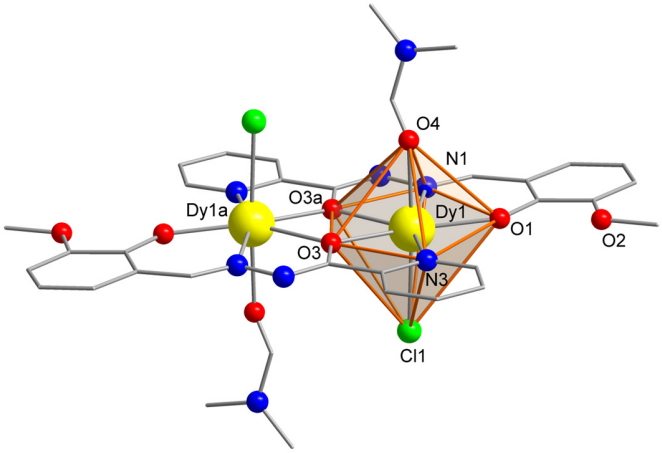

Figure 2.5 Structure of **1** highlighting the disordered pentagonal bipyramidal coordination polyhedron of Dy1 in orange used in the Shape-Measure Approach calculations. Structure of **1**, **3**, **4** and **6** follows the same labelling scheme.

In centrosymmetric complexes **1** and **4**, both Dy centers hold disordered pentagonal bipyramidal geometry (Figure 2.5). As mentioned in chapter 1, the effective energy barrier relates to several different aspects, including the metal center arrangement, the magnetic coupling and the orientation of the magnetic anisotropic axes. Normally, the higher the similarity between the complexes, the more the comparability they have. Therefore, it is a precious chance to study the attribution of small structure change on their magnetic properties between these two series complexes. In deriving magneto-structural correlations, it is essential to provide a quantifiable structural comparison of the coordination spheres between these two series of complexes. To that end, the shape-measure (Eqn. 1) approach was utilized based on the dihedral angles along the edges of the polyhedron of Dy1 and Tb1 (Figure 2.5) [11]. Shape measure [11] SM with δi = observed dihedral angle along m edges of a coordination polyhedron (angle between normals of adjacent faces) and θi = corresponding dihedral angle for a reference polyhedron.

$$SM = \min\left[\sqrt{\frac{1}{m}\sum_{i=1}^{m}(\delta i - \theta i)^2}\right] \qquad \textbf{Eqn. 1}$$

Complexes **4** and **6** have been selected as the parent complexes for Dy^{III} and Tb^{III} species, respectively. Within each metal system, a deviation of 4.553° and 4.913° has been found between **1** and **4**, as well as **3** and **6** (Table 2.2). Such deviation values can be

regarded as relatively large. The difference in the structures corresponds to coordinating monodentate DMF molecules (**1** and **3**) and IPA molecules (**4** and **6**), which also cause different angles of O4-Ln1-Cl1 as mentioned earlier. This could be speculated as the main reason for the large difference in energy barriers between **1** and **4**, since the composition of the rest of the polyhedron is highly similar.

Table 2.2 Dihedral angles along the edges of the coordination polyhedral (°) of dysprosium complexes **1**, **3**, **4** and **6**.

EDGE	**1**	**4**	**3**	**6**
O1-N1	75.617	80.029	75.046	80.44
O1-N3	70.081	77.818	69.138	77.256
O1-O4	54.279	51.376	54.777	51.345
O1-Cl1	58.919	54.832	59.742	55.523
O3a-O3	75.281	64.567	76.183	65.059
O3a-O4	43.285	48.766	42.864	48.209
O3a-Cl1	52.577	54.823	52.252	54.393
O3a-N1	79.35	72.837	79.609	73.465
N1-O4	57.684	57.993	57.879	57.818
N1-Cl1	59.276	60.373	58.625	59.678
N3-O3	78.065	74.86	78.755	75.451
N3-Cl1	69.149	68.093	69.277	67.293
N3-O4	61.174	60.298	61.438	60.518
O3-Cl1	49.378	50.272	49.681	51.046
SM	4.553	0	4.913	0

2.2.2 Magnetic Study of 1-6

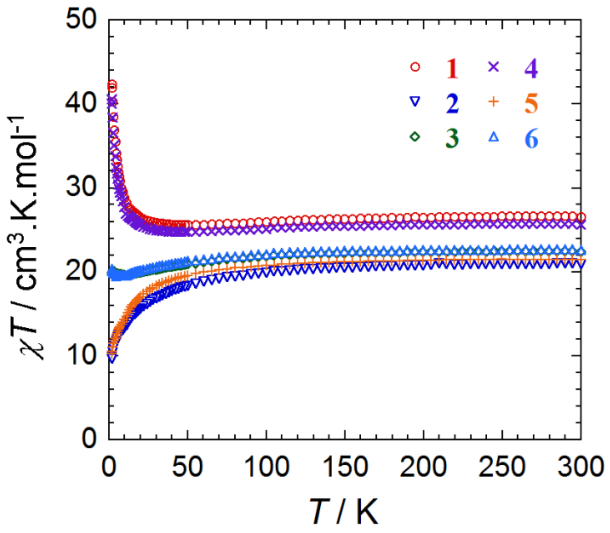

Figure 2.6 Temperature dependence of the magnetic susceptibility, χT, at 1000 Oe for complexes **1-6**.

The direct current (dc) magnetic properties of complexes **1-3** were investigated under a 1000 Oe field in the temperature range of 1.8-300 K (Figure 2.6). Ferromagnetic interaction has been observed for the dysprosium analogue **1**, with a room temperature χT value of 26.60 cm^3 K mol^{-1}, which is lower than the theoretical value for two noninteracting Dy^{III} ions ($^6H_{15/2}$, $S = 5/2$, $\chi T = 28.34$ cm^3 K mol^{-1}). Upon the decrease of the temperature, the χT product remains nearly constant then increases dramatically reaching a maximum value of 42.37 cm^3 K mol^{-1} of at 1.8 K. The increase of χT at low temperature range suggests the presence of intramolecular interactions between the metal centers, as shown in other dysprosium systems [7]. Interestingly, the erbium complex **2** presents an antiferromagnetic interaction. At room temperature, the χT value is equal to 20.97 cm^3 K mol^{-1} within reasonable agreement of the expected value ($^4I_{15/2}$, $S = 5/2$, $\chi T =$ 22.96 cm^3 K mol^{-1}) for two uncoupled Er^{III} ions. For complex **3**, the room temperature χT value of 22.40 cm^3 K mol^{-1}, is consistent with the presence of two Tb^{III} ions ($^7F_6$, $S = 5/2$, $\chi T = 23.64$ cm^3 K mol^{-1}). Upon lowering the temperature, an almost constant χT value is obtained down to ~50 K, then a slight drop to a minimum value of 19.57 cm^3 K mol^{-1} at 12 K, originating from the thermal depopulation of the Stark sublevels and/or the presence of significant magnetic anisotropy. [13c] The subsequent increase in the χT product reaching

19.71 cm^3 K mol^{-1} at 1.8 K suggests the possible presence of a weak intramolecular ferromagnetic exchange interaction.

In the IPA solvent series (**4-6**), dc magnetic properties have been probed as well and present similar results as the DMF coordinated complexes (**1-3**). Complex **4** exhibits similar magnetic behavior as complex **1**, the interaction between Dy^{III} ions appears ferromagnetic as well (Figure 2.6). At room temperature, the χT value is 25.60 cm^3 K mol^{-1}, and increases with decreasing temperature reaching a maximum value of 40.57 cm^3 K mol^{-1} at 1.8 K. Consistent with the other Er^{III} compound **2**, complex **5** gives a nearly constant χT value with decreasing temperature until a smooth drop in the lower temperature range below 45 K, potential antiferromagnetic interaction behavior. The room temperature χT value is 21.44 cm^3 K mol^{-1}, which corresponds well to the expected value of 22.96 cm^3 K mol^{-1}. The lowest value of 10.27 cm^3 K mol^{-1} has been reached at 1.8 K, close to the corresponding value for complex **2** of 9.63 cm^3 K mol^{-1}. As is the case with **3**, Tb^{III} dinuclear complex **6** presents weak ferromagnetic coupling as well, with a room temperature χT value equal to 22.59 cm^3 K mol^{-1}. Overall, these two series of complexes with different coordinating solvent molecules are showing similar dc magnetic properties for each metal species.

The field dependence of the magnetization below 7 K have been plotted for complexes **1-6**, non-saturation of the magnetization indicates the presence of significant magnetic anisotropy and/or low-lying excited states in all systems (Figure 2.7 and 2.8). This can be further confirmed by the lack of superposition and high field variation on a single master curve of each *M* vs. *H/T* plots. The values of the magnetization at 1.8 K and 7 T are 9.80, 9.46, and 8.72 μ_B for complex **1-3**, and 9.29, 9.45 and 9.26 μ_B for complexes **4-6**, respectively. Within the more comparable systems **1** and **4**, highly similar behavior can be observed which indicates that no torquing and possibly very weak magnetic interactions in both samples.

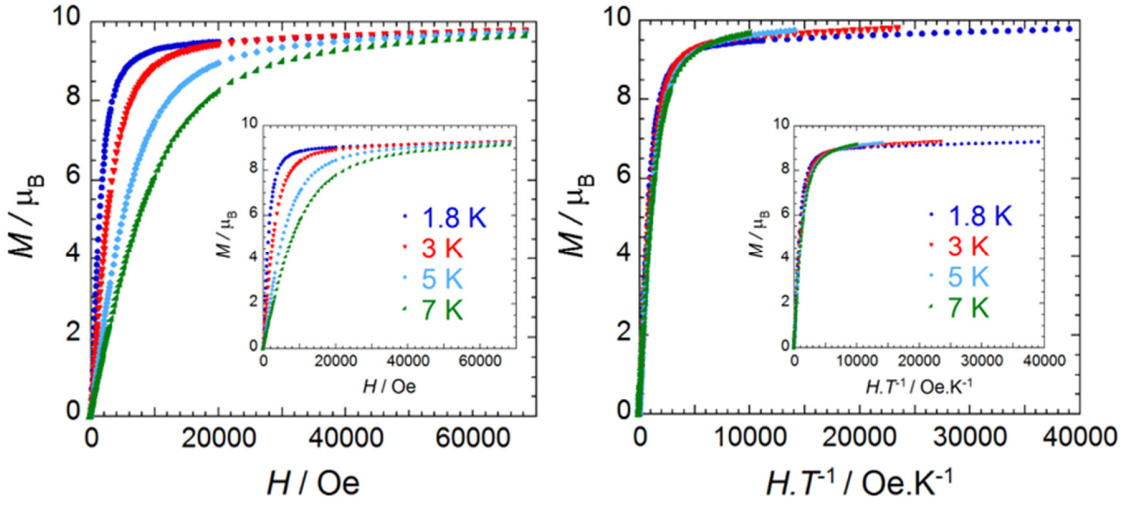

Figure 2.7 Field dependence of the magnetization *M* at 1.8, 3, 5, and 7 K for complex **1** plotted as *M vs. H* and *M vs. HT*$^{-1}$. The inset is the magnetization for complex **4**.

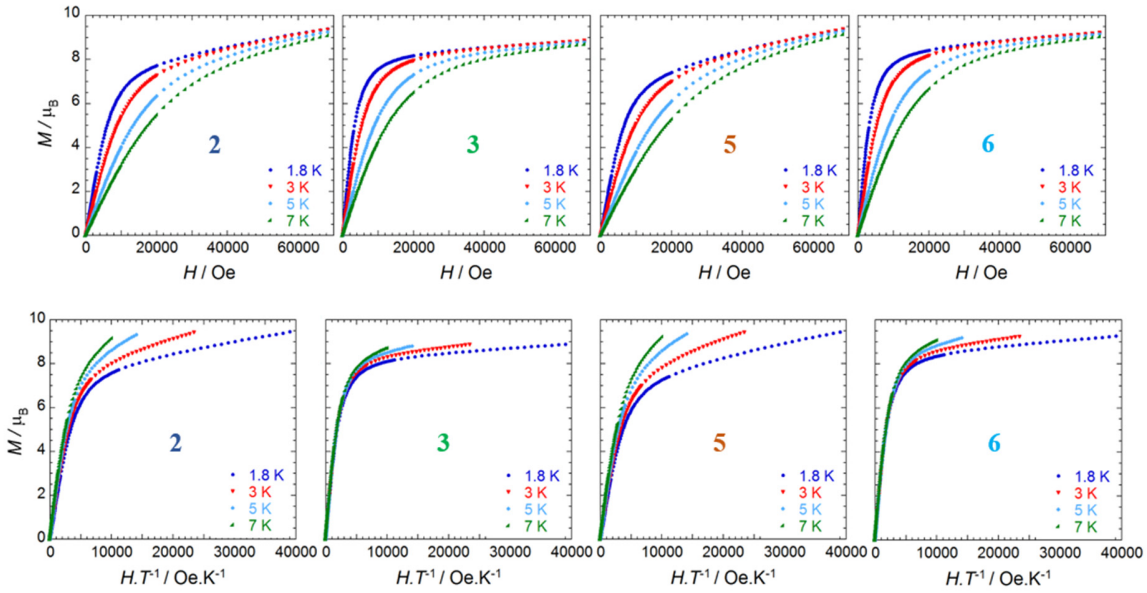

Figure 2.8 Field dependence of the magnetization *M* at 1.8, 3, 5, and 7 K for complex **2, 3**, **5** and **6** plotted as *M vs*. *H* (top) and *M vs. HT*$^{-1}$ (bottom).

In order to investigate the potential slow magnetization relaxation, alternating current (ac) measurements were performed on all complexes. However, the temperature and frequency dependent ac susceptibility signals were only clearly observed on two dysprosium complexes **1** and **4** (Figure 2.9) in zero applied dc field, which indicates the

SMM nature of these compounds. The in-phase (χ') and out-of-phase (χ'') susceptibilities were measured in the temperature range of 1.8-17 K and 1.8-20 K for complexes **1** and **4**, respectively. The presence of peaks shifting to lower frequency with decreasing temperature is indicative of slow magnetization relaxation.

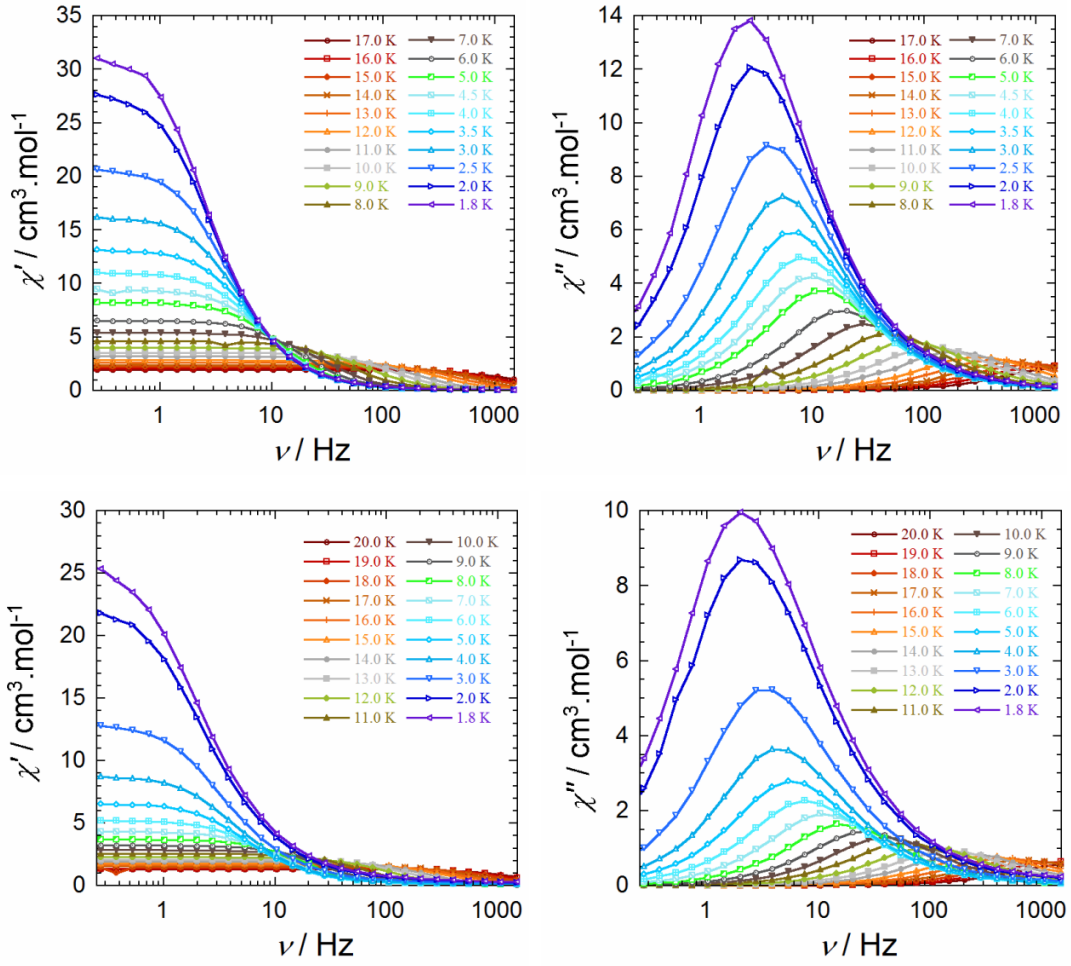

Figure 2.9 Frequency (υ) dependence of the in-phase (χ', left) and out-of-phase (χ'', right) magnetic susceptibility at the indicated temperatures for **1** (top, 1.8-17 K) and **4** (bottom, 1.8–20 K) under zero applied dc field.

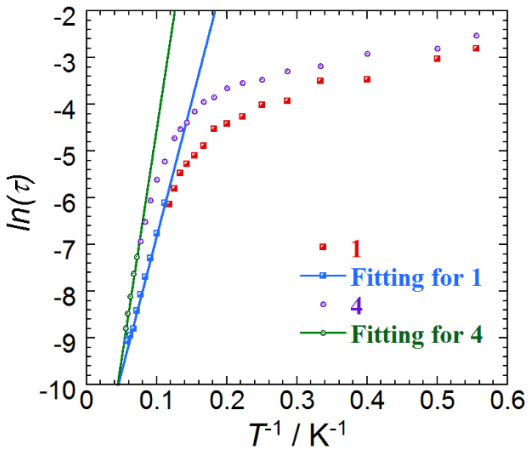

Figure 2.10 Relaxation time of the magnetization *ln(τ) vs.* T^{-1} at zero dc field for complex **1** and **4**. The anisotropic barriers (obtained by fitting this data using the Arrhenius law, $\tau = \tau_0 \exp(U_{eff}/kT)$) [12] were calculated to be U_{eff} = 58 K (τ_0 = 3.51*10^{-6} s) for **1**, and U_{eff} = 98 K (τ_0 = 6.69*10^{-7} s) for **4**, respectively.

In light of Tb^{III} being a non-Kramers ion, rigorous axial symmetry is usually required to maintain the bistability of the ground state, hence it is not surprising to see the absence of slow magnetic relaxation for Tb^{III} complex **3**. For erbium analogue **2**, only high frequency tails are observed in χ'' *vs.* υ plot at 2 K for fields over 400 Oe, further analysis of the relaxation behavior is precluded. Nevertheless, in the case of **5** and **6**, a growing out-of-phase signal at high frequency was observed with the application of an external field which may indicate potential SMM behavior. Unfortunately, no full peaks can be achieved.

The anisotropic energy barrier can be obtained from the high temperature regions of the relaxation where it is thermally activated. Fitting with the Arrhenius equation ($\tau = \tau_0 \exp(U_{eff}/kT)$) yields U_{eff} = 58 K (τ_0 = 3.51*10^{-6} s) for **1** and U_{eff} = 98 K (τ_0 = 6.69*10^{-7} s) for **4** (Figure 2.10). It is worth mentioning that the *ln(τ)* becomes nearly temperature independent at lower *T* for both complexes, where a quantum tunneling relaxation pathway becomes dominant. The Cole-Cole plots (Figure 2.11 and 2.12) show a relatively symmetrical shape and have been fitted using a generalized Debye model, with α parameters below 0.1 for both complexes **1** and **4** above 5 K. This low degree of deviation from the pure Debye model confirms that a single relaxation mechanism is mainly involved in these relaxation processes. For **4**, an increase in α up to 0.22 (1.8 K) is

observed below 4 K, which could possibly due to some Dy-Dy interaction at very low temperature.

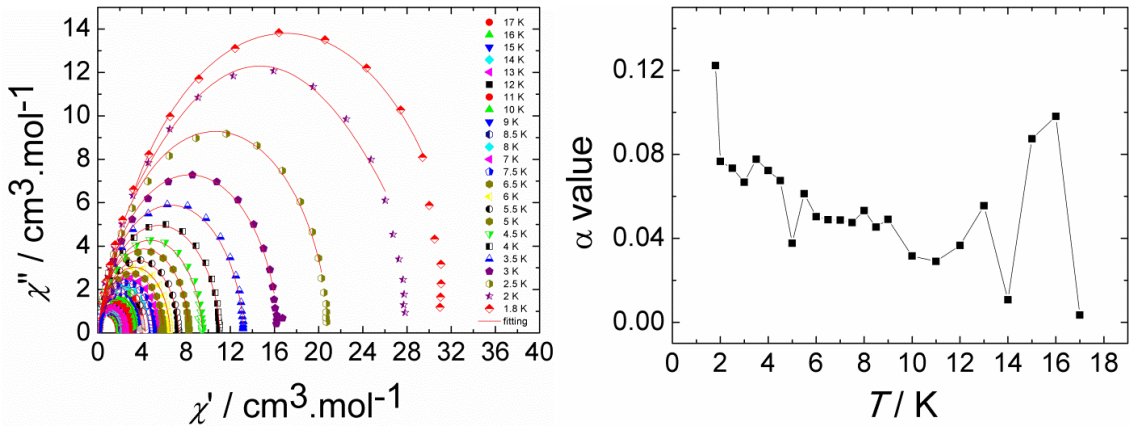

Figure 2.11 Cole-Cole plot using the ac susceptibility data for complex **1** (left) and the obtained α values from the fit using a generalized Debye model plotted as α *vs.* T (right).

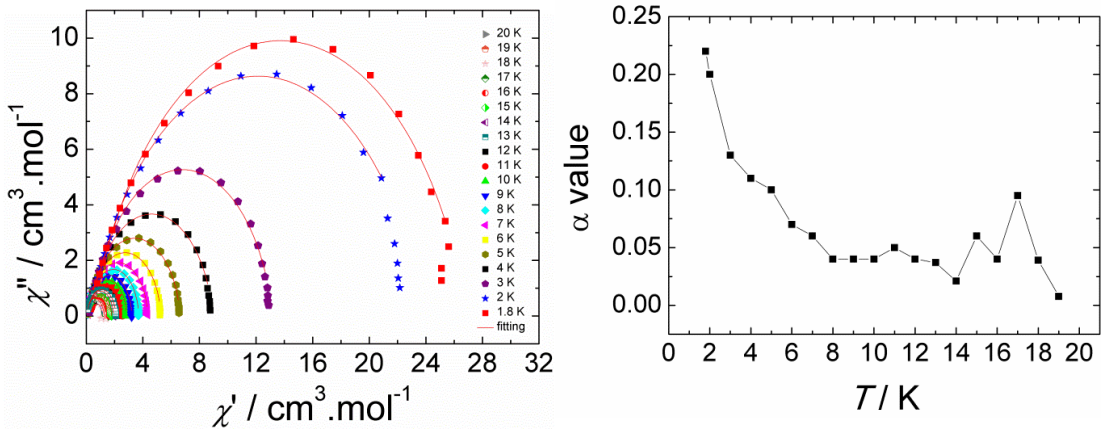

Figure 2.12 Cole-Cole plot using the ac susceptibility data for complex **4** (left) and the obtained α values from the fit using a generalized Debye model plotted as α *vs.* T (right).

2.2.3 The Difference between DMF and IPA Groups

In light of the same general structure for the main ligands, the distinction between **1-3** and **4-6** should be attributed to the monodentate coordinated solvents: DMF and IPA. As previously mentioned, the angle of O4-Ln1-Cl1 exhibits the most divergence over 12° which might further influence the packing arrangement, the bent angle on the ligand $ovph^{-2}$ (doubly deprotonated H_2ovph) and other minute changes in the structures. Moreover, the

shape measure revealed a deviation over 4.5°. It would not be surprising if the orientation of anisotropic axes, known to be highly dependent on the coordination environment of the metal centers, [4] were found to be different. Consequently, the energy barriers of **1** and **4** would also be significantly different.

There may be a few more questions that still need to be answered: 1) why erbium analogues **2** and **5** behave differently from the rest of the series in terms of their intramolecular interactions? Do they exhibit real antiferromagnetic interactions or is the decrease in χT a reflection of the depopulation of the crystal field splitting energy levels? And 2) what causes the significant difference in energy barriers between **1** and **4**, especially considering the overall similarity in structure? If we assume that the energy gap between the ground and first excited states (excluding possible QTM) is equal to the energy barrier extracted from the dynamic magnetic properties, then minute differences in the metal center's coordination environment would influence the energy barriers greatly. Computational studies could shed some light on these questions and would be the next logical approach.

2.3 Asymmetric Dinuclear System

Another important observation in **Ref-1** is that low-symmetry coordination environments can produce efficient magnetization blocking in Dy^{III} SMMs which allows us to probe the contributions of both exchange interactions and single-ion anisotropy to the dynamic magnetic properties, simultaneously. [5] The theoretical calculations revealed *g*-tensors of g_z = 19.6668 and 19.6880 for eight and seven-coordinate dysprosium, respectively, and the local anisotropy axes being aligned nearly parallel with the Dy···Dy axis which corroborates the ferromagnetic exchange in **Ref-1** as dipolar in nature. It would be interesting to further investigate such asymmetric {Dy_2} complexes by using the same ligand H_2ovph while slightly modifying its coordination pockets. Compound **7** and **8** were synthesized with this objective in mind.

2.3.1 Structure Analysis for 7 and 8

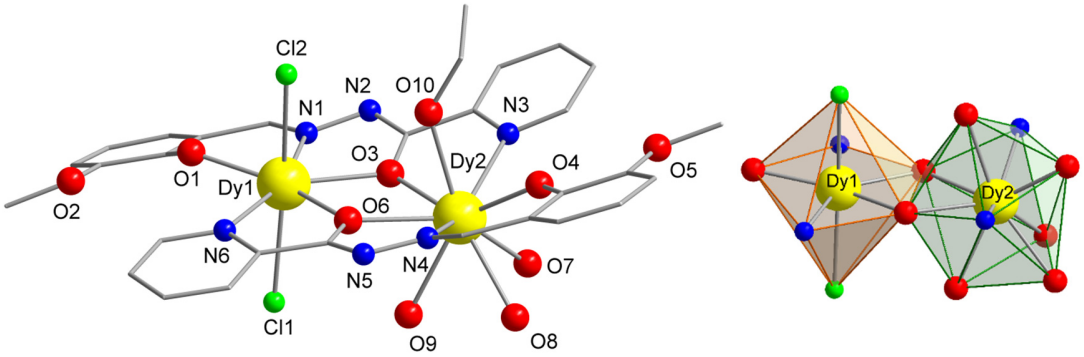

Figure 2.13 Left: Labeled molecular structure of asymmetric complex $[Dy^{III}_2(ovph)_2(H_2O)_3(EtOH)Cl_2]$, **7**, where H_2ovph = 2-hydroxy-3-methoxybenzaldehyde (pyridine-2-carbonyl) hydrazone. Color code: yellow (Dy), red (O), blue (N), green (Cl) and grey (C). Hydrogen atoms have been omitted for clarity. Right: Coordination polyhedron of Dy1 in orange and Dy2 in green.

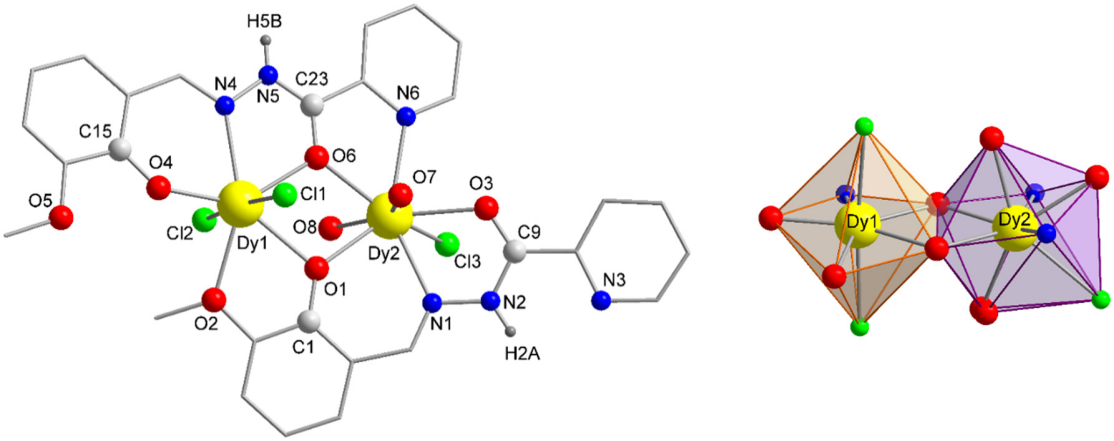

Figure 2.14 Left: Labeled structure of asymmetric complex $[Dy^{III}_2(Hovph)_2(OH)Cl_3(H_2O)]\cdot 2H_2O$, **8**, where H_2ovph = 2-hydroxy-3-methoxybenzaldehyde (pyridine-2-carbonyl) hydrazone. Color code: yellow (Dy), red (O), blue (N), green (Cl) and grey (C). Hydrogen atoms and solvent molecules have been omitted for clarity. Right: Coordination polyhedron of Dy1 in orange and Dy2 in purple.

The single X-ray crystallography studies reveal that complex **7** crystallizes in monoclinic $P2_1/n$ space group (Table A.2, appendix A). The main structure consists of two $ovph^{-2}$ ligands that are following the same antiparallel architecture as the previous complex

1-**6**, and similarly, the alkoxido oxygen atoms O3 and O6 are bridging two Dy^{III} metal centers (Figure 2.13) with an average Dy-O-Dy angle of 113.5° (Table 2.3). The doubly deprotonated ligand format can be confirmed by the change in the bond distances of C9-O3 (C23-O6) and C9-N2 (C23-N5). Disordered pentagonal bipyramidal geometry is observed for Dy1 with two chloride ions completing the coordination sphere, the Cl1-Dy1-Cl2 angle of 169.3° is intermediate to complexes **1** and **4** (Figure 2.13). As for the nine-coordinated Dy2, four oxygen atoms provided by one EtOH and three water molecules from distinct sides form its unique geometry. There are hydrogen bonds existing between Cl1-O9 and Cl2-O10 with bond distances equal to 3.12 and 3.17 Å, respectively, and the latter may influence the arrangement of EtOH molecule's location. Also caused by hydrogen bonds, contacts originated from O1···O7 and O2···O9 result in tight packing with the closest intermolecular Dy···Dy distance being 6.26 Å. As a consequence, the ligand on the O1 and O2 side is found to be bent.

A procedure similar to that for **7** except replacing EtOH solvent by IPA yields yellow rhombus crystals of **8** after a week. The single crystal X-ray diffraction measurement reveals that compound **8** crystallizes in space group *P1* with Z = 2 (Figure 2.14). Different from all the complexes shown earlier in this chapter, **8** exhibits two parallel ligands and both of them are singly deprotonated with one minus charge. This is confirmed by carefully compared with the free ligand on bond distances (Table 2.3). As the bridging oxygen atoms are originating from ketone and phenoxy groups, respectively, large differences between Dy1-O1-Dy2 and Dy1-O6-Dy2 angles have been found with values of 106.68 and 113.25°. The Dy···Dy distance is 3.84 Å, which is close to the reported value with a similar structure arrangement. [6] Consistent with **7**, Dy1 is in a disordered pentagonal bipyramidal polyhedron with two chloride ions coordinated on distinct sides and the Cl1-Dy1-Cl2 angle is equal to 174.40°. However, the coordination sphere for Dy2 is completed by one chloride ion (Cl3) and two water molecules where O7 is deprotonated and O8 is refined to be disordered over two possible sites with site-occupancy factors of 0.5, making it eight-coordinate with a disordered square antiprismatic geometry. [13] The contained solvent accessible voids are noteworthy in this particular structure with about 180 $Å^3$, which means that the structure of **8** might be highly dependent on the solution environment. The shortest intermolecular Dy···Dy distance is 7.42 Å.

Table 2.3 Selected bond distances and angles for complex **7** and **8**.

	7		**8**
Dy1-Dy2/Å	3.954(1)	Dy1-Dy2/Å	3.8347(3)
Dy1-O3/Å	2.30(1)	Dy1-O1/Å	2.432(4)
Dy1-O6/Å	2.32(1)	Dy1-O6/Å	2.287(3)
Dy2-O3/Å	2.44(1)	Dy2-O1/Å	2.348(3)
Dy2-O6/Å	2.40(1)	Dy2-O6/Å	2.305(4)
Dy2-O10/Å	2.45(1)	Dy2-O7/Å	2.378(5)
Dy2-O7/Å	2.48(1)	Dy2-O8/Å	2.47(2)
Dy2-O8/Å	2.50(1)	Dy2-Cl3/Å	2.724(2)
Dy2-O9/Å	2.44(1)	Dy1-Cl1/Å	2.666(2)
Dy1-Cl1/Å	2.662(5)	Dy1-Cl2/Å	2.286(2)
Dy1-Cl2/Å	2.665(5)	C9-N2/Å	1.331(6)
C9-N2/Å	1.30(2)	C9-O3/Å	1.252(7)
C9-O3/Å	1.30(2)	C23-O6/Å	1.314(7)
C23-O6/Å	1.28(2)	C23-N5/Å	1.284(7)
C23-N5/Å	1.31(2)	C1-O1/Å	1.327(6)
Cl1-O9/Å	3.12(1)	C2-O2/Å	1.396(7)
Cl2-O10/Å	3.17(1)		
Dy1-O3-Dy2/°	113.2(5)	Dy1-O1-Dy2/°	106.7(2)
Dy1-O6-Dy2/°	113.8(4)	Dy1-O6-Dy2/°	113.2(2)
Cl1-Dy1-Cl2/°	169.3(1)	Cl1-Dy1-Cl2/°	174.40(5)
Packing/Å	6.256(1)	Packing/Å	7.4212(3)

2.3.2 Magnetic Properties and Multi Relaxation Processes

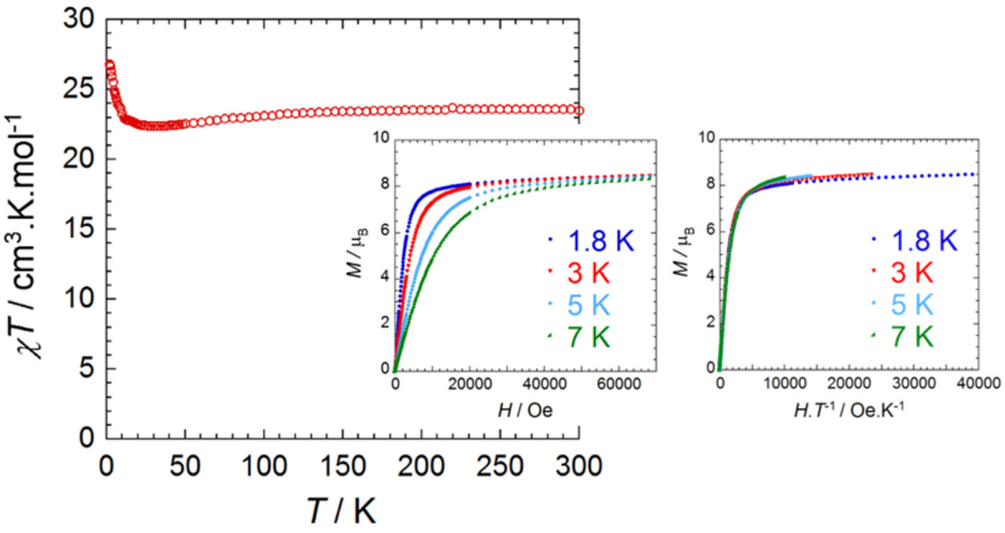

Figure 2.15 Temperature dependence of the magnetic susceptibility χT at 1000 Oe for complex **7**. Inset: Field dependence of the magnetization M at 1.8, 3, 5 and 7 K for complex **7** plotted as M *vs.* H and M *vs.* HT^{-1}.

Magnetic susceptibility data were collected for complex **7** under a static field of 1000 Oe (Figure 2.15). The χT value of 23.52 cm^3 K mol^{-1} obtained at 300 K is lower but in decent agreement with the value anticipated for two non-interacting Dy^{III} ions ($^6H_{15/2}$, S = 5/2, χT = 28.34 cm^3 K mol^{-1}). The χT product remains roughly constant upon the decreasing of the temperature before dramatically increasing around 10 K and reaching a maximum value of 26.79 cm^3 K mol^{-1} at 1.8 K. The field dependence of the magnetization in the temperature range of 1.8–7 K have been collected for complex **7** (Figure 2.15), the non-superimposition of the curves in the M *vs.* HT^{-1} plot on a single mastercurve suggests the presence of magnetic anisotropy and/or the lack of a well-defined ground state, where the low-lying excited states might be populated when a field is applied. [14] The magnetization value obtained for complex **7** at 1.8 K under 7 T is 8.49 μ_B.

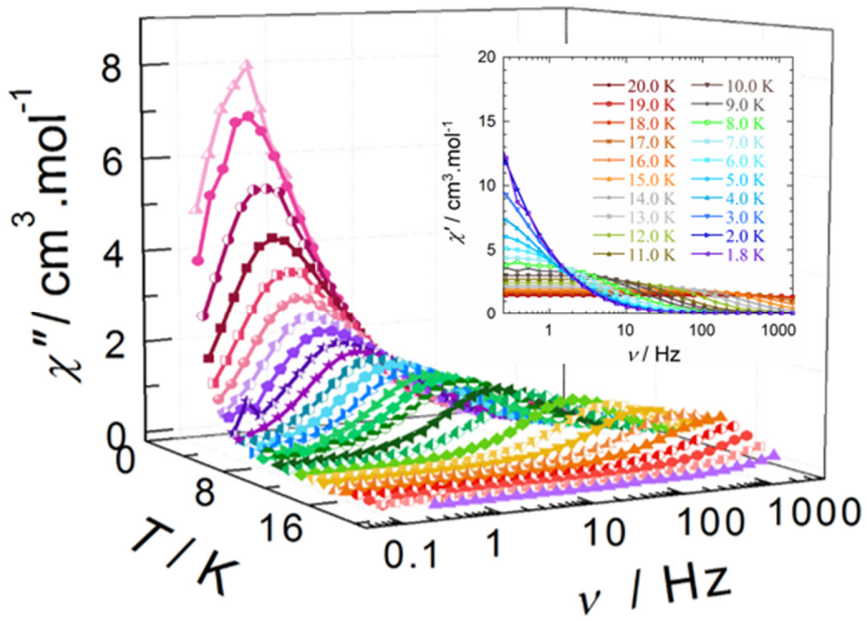

Figure 2.16 Out-of-phase susceptibility, χ'', *vs.* frequency, υ, (logarithmic scale) in the temperature range 1.8–20 K for **7** under zero dc field. Inset: Frequency (υ) dependence of the in-phase (χ') magnetic susceptibility at the indicated temperatures.

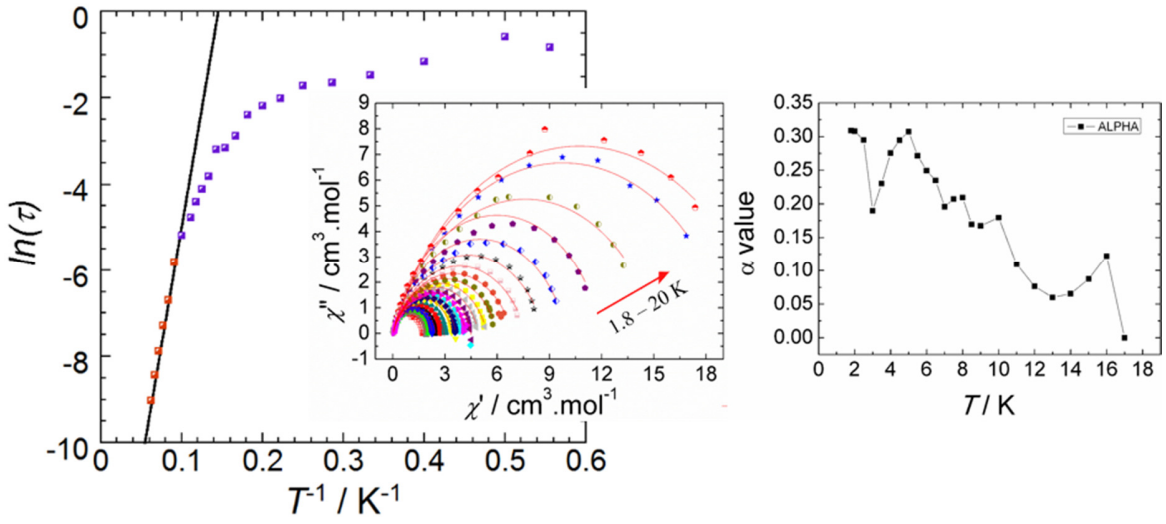

Figure 2.17 Left: Relaxation time of the magnetization *ln(τ) vs.* T^{-1} at zero dc field for complex **7**. The anisotropic barriers (obtained by fitting this data using the Arrhenius law, $\tau = \tau_0 \exp(U_{eff}/kT)$) were calculated to be U_{eff} = 110 K (τ_0 = 1.36*10^{-7} s). Middle: Cole-Cole plot using the ac susceptibility data for complex **7**. Right: The obtained α values from the fit using a generalized Debye model plotted as α *vs. T*.

To probe the existence of SMM-type behavior for complex **7**, ac susceptibility measurements were performed in the temperature range 1.8-20 K with zero dc field. The out-of-phase (χ'') component of the ac susceptibility (Figure 2.16) clearly exhibits temperature- and frequency-dependent behavior, which indicates the presence of slow magnetization relaxation. In the high-temperature regime, the relaxation process follows an Arrhenius law with an effective energy barrier U_{eff} = 110 K (τ_0 = 1.36*10^{-7} s) (Figure 2.17, left). An evaluation of the distribution for the relaxation times from analysis of the Cole-Cole plot for complex **7** yielded a relatively large α parameter (ca. 0.20; Figure 2.17, right), which suggests a potential multi-pathway relaxation mechanism. This could be related to the structure of the compound that is made up by two different Dy^{III} centers. When the system enters the quantum regime (below 5 K), an increase in α up to 0.31 (1.8 K) is observed.

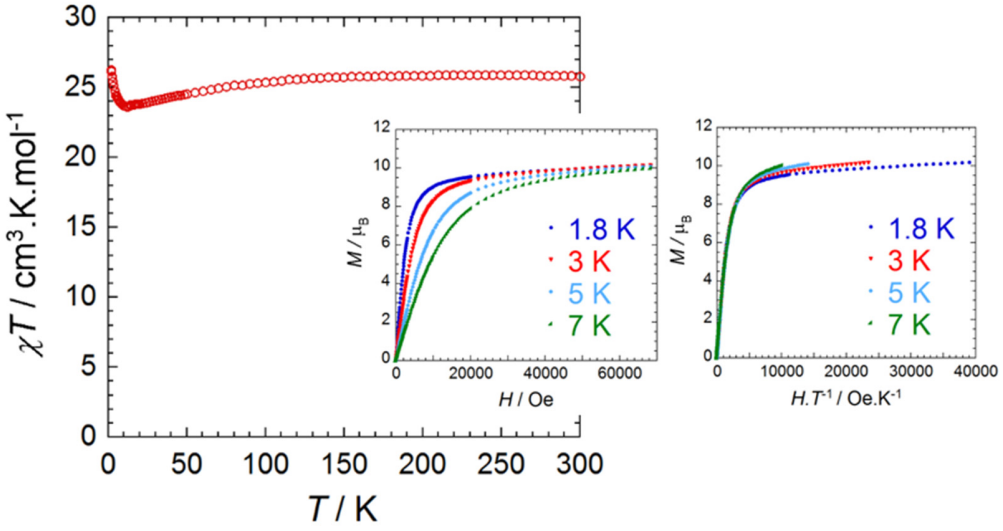

Figure 2.18 Temperature dependence of the magnetic susceptibility χT at 1000 Oe for complex **8**. Inset: Field dependence of the magnetization M at 1.8, 3, 5 and 7 K for complex **8** plotted as M *vs.* H and M *vs.* HT^{-1}.

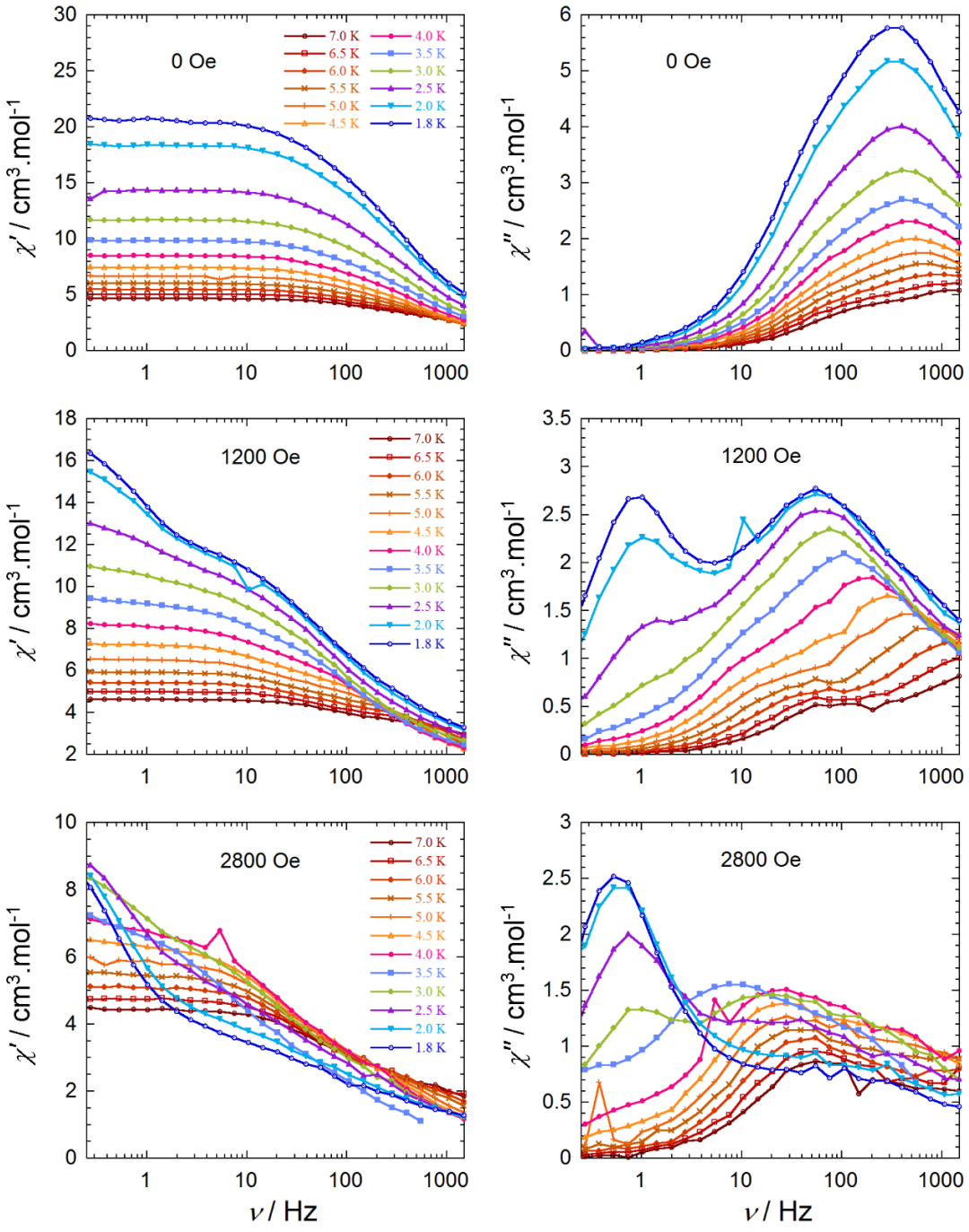

Figure 2.19 Frequency (υ) dependence of the in-phase (χ', left) and out-of-phase (χ'', right) magnetic susceptibility at the indicated temperatures for **8** under zero (top), 1200 (middle) and 2800 (bottom) Oe applied dc field.

For **8**, typical ferromagnetic intramolecular interaction is revealed in the magnetic susceptibility versus temperature plot (Figure 2.18), and the room temperature χT product

is found to be 26.13 cm^3 K mol^{-1} which is consist with the theoretical value for two non-interacting Dy^{III} ions of 28.34 cm^3 K mol^{-1}. By decreasing of temperature, the χT value remains nearly constant before a stepwise drop in the low-temperature range reaching a minimum value of 23.59 cm^3 K mol^{-1} at 12 K. With further temperature decrease, this is followed by a sharp increase in the χT value reaching 26.26 cm^3 K mol^{-1} at 1.8 K. The field-dependent magnetization measurements (Figure 2.18) show similar behavior to complex **7** that present non-saturation at the indicated temperatures, and also a lack of superimposition of the *M vs.* HT^{-1} data on a single master curve. Both of them indicate the presence of significant magnetic anisotropy and/ or low-lying excited states in this system. The magnetization value obtained for complex **8** at 1.8 K under 7 T is 10.20 μ_B.

Alternating current (ac) measurements were carried out under zero applied dc field between 1.8-7 K for complex **8**. However, no clear frequency dependent peak shifting is observed (Figure 2.19, top). Instead, overlapping peaks are observed in the out-of-phase (χ'') ac susceptibility plot indicating QTM mainly. To diminish the quantum effect, [15] applied dc fields of 1200 and 2800 Oe were applied as the optimum field for further measurements (Figure 2.19, middle and bottom). Not surprisingly, two slow relaxation processes are found, and that could be related to the two distinct Dy coordination spheres. However, assigning each relaxation pathway to a particular metal center is rather difficult and remains uncharted territory that will require further studies and, might not be potentially possible. For our system, under an applied field of 1200 Oe, fitting the high-frequency data with Arrhenius law where $\tau = \tau_0 \exp(U_{eff}/kT)$, the effective energy barrier is found to be 22 K ($\tau_0 = 3.88*10^{-6}$ s, Figure 2.20). On the other hand, under 2800 Oe applied static field, a barrier of 8 K ($\tau_0 = 6.22*10^{-4}$ s) is obtained for the high-frequency region as well. The multiple relaxation processes in high-frequency region under different applied fields might arise from the spin-flip through different excited states.[16] Although the lower frequency relaxation process and its corresponding barrier or relaxation time could not be presented quantitatively, the existence of a second relaxation is quite clear. This may provide insight into the study of separate relaxation modes for asymmetry dinuclear systems.

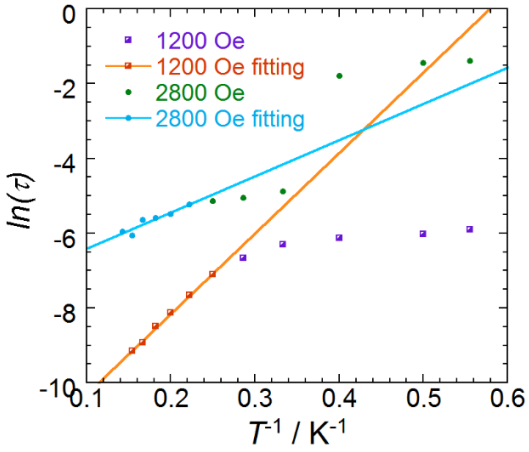

Figure 2.20 Relaxation time of the magnetization *ln(τ) vs.* T^{-1} at 1200 and 2800 Oe dc field for complex **8**. The anisotropic barriers (obtained by fitting these data using the Arrhenius law, $\tau = \tau_0 \exp(U_{eff}/kT)$) were calculated to be U_{eff} = 22 K ($\tau_0 = 3.88*10^{-6}$ s) under 1200 Oe and U_{eff} = 8 K ($\tau_0 = 6.22*10^{-4}$ s) under 2800 Oe.

2.3.3 Variations in Polyhedra

The fact that the seven-coordinate spheres for Dy1 sites in both complexes **7** and **8** are the same as those seen in the published work **Ref-1**, causes great concern. Thus, shape-measure is included for these systems which may provide a more authentic comparison of their coordination environments and a possible reflection on the difference in the magnetic properties between these complexes (Table 2.4).

When complex **7** is selected as the parent complex, its deviation from **8** and **Ref-1** complexes are 4.61° and 4.53°, respectively. On top of that, by taking complex **8** as the reference and comparing with **Ref-1**, a larger deviation of 5.12° is obtained, thus we can conclude that these dysprosium ions are actually located in very different environments. Especially complex **8**, with its distinct coordination sphere, shows a remoter relevance to the other two. The similarly coordinated Dy ions are sufficiently dissimilar on a molecular standard, while the two distinct Dy ions in each asymmetric complex are very different. The contrasting responses observed to dynamic magnetic fields could be assigned to the change in the structure and possibly different orientations of the easy axes of magnetization for the asymmetric complexes. [5] For future work, a comprehensive computational study

of the orientations of magnetic axes is needed in order to access more information and be able to determine the origins of the different magnetic properties observed experimentally.

Even though **7** presents a relatively large α parameter around 0.2, no clearly separated peaks could be obtained from the χ'' versus frequency plot. However, complex **8** and **Ref-1** seem to be more similar in that multi-relaxation processes are observed. Though the origin of the energy barrier or slow relaxation is based on the difference in energy between the $M_S = \pm S$ and the next highest Ms level, we are not able to present that data here without a detailed computational study.

Table 2.4 Dihedral angles along the edges of the coordination polyhedral (°) of Dy1 in complexes **7**, **8** and Dy2 in **Ref-1**. Calculation equation follows **Equation 1** as previously introduced.

EDGE	**7**	EDGE	**8**	EDGE	**Ref-1**
O3-O6	71.297	O1-O6	68.826	O4-O1	67.188
O6-N6	79.715	O6-N4	74.015	O1-N3	74.248
N6-O1	74.236	N4-O4	71.873	N3-O2	73.822
O1-N1	61.075	O4-O2	65.817	O2-N4	66.763
N1-O3	67.813	O2-O1	71.877	N4-O4	70.555
O3-Cl2	49.333	O1-Cl2	51.299	O4-Cl2	53.633
O6-Cl2	49.858	O6-Cl2	45.952	O1-Cl2	47.041
N6-Cl2	60.593	N4-Cl2	66.863	N3-Cl2	64.48
O1-Cl2	56.155	O4-Cl2	50.388	O2-Cl2	53.917
N1-Cl2	73.051	O2-Cl2	69.586	N4-Cl2	65.54
O3-Cl1	54.958	O1-Cl1	62.367	O4-Cl1	49.546
O6-Cl1	48.801	O6-Cl1	53.493	O1-Cl1	56.102
N6-Cl1	55.701	N4-Cl1	54.253	N3-Cl1	54.75
O1-Cl1	62.631	O4-Cl1	64.897	O2-Cl1	60.481
N1-Cl1	62.66	O2-Cl1	55.803	N4-Cl1	68.137
SM	0	-	4.605	-	4.531
SM	-	-	0	-	5.121

2.4 Looking for the Ferromagnetism in {Dy_2} Systems

By choosing similarly constructed didysprosium systems, herein we define "similar" as: the oxygen atoms responsible for μ-O bridges that are originating from phenoxido or alkoxido groups from Schiff base ligands, we are looking for characters from complexes that showing ferromagnetic interactions. Table 2.5 lists some typical complexes after screening from 106 dinuclear Dy^{III} compounds that have been published to date, and also complexes **1**, **4**, **7** and **8** extracted from our work. Except for the last two complexes, **Ref-9** [6] and **Ref-10** [18] which show antiferromagnetic interactions, all other complexes reveal weak ferromagnetic intramolecular interactions. It can be observed that the most common characteristics for the ferromagnetically-coupled compounds is a large Dy···Dy distance of approximately 3.8-3.9 Å and an average Dy-O-Dy angle around or over 110°. Especially for compounds **1**, **4**, **7**, **8** and reference complexes **Ref-1**, **Ref-2** and **Ref-3** [6, 7] that consist of the same ligand $Hovph^{-1}$/$ovph^{-2}$, which seem to fit this rule very well. **Ref-9** is the only exception with this ligand, yet, the smaller metal center distance and shrunken Dy-O-Dy angle might explain the observed antiferromagnetic interaction since both features are outside the distances and angles range that cited earlier for ferromagnetically coupled systems. Additionally, in **Ref-9** the source of bridging oxygens is the phenoxy groups, which is different than the rest of the compounds which exhibit bridging oxygens from fully or partially deprotonated alkoxido atom(s). Taking the rigid ligand nature into consideration, large metal-metal distances and open M-O-M angles can be predetermined when alkoxido-bridging occurs. Then, the question arises, would this large metal-metal separation be a necessary condition for systems to interact in a ferromagnetic fashion? Maybe in doubly-bridged systems, but certainly not in multi (>2) bridged systems like **Ref-4**, [19] **Ref-8** and **Ref-9**. Multi bridged systems could be more complicated based on the diversity of the μ-O bridging sources and their possible contributions to the metal-metal interactions. Moving towards phenoxido-bridged compounds, we are unable to conclude a general rule either. For instance, **Ref-6** and **7** [17, 15] are both showing ferromagnetic intramolecular interactions with close metal-metal distances and angles compared to **Ref-10** [18] and its derivatives [20] which reveal antiferromagnetism instead. Between different bridging types, **Ref-3** and **Ref-7** are more comparable based on their similar construction,

and both of them are centrosymmetric systems. While the type of bridging oxygen atoms do not seem to direct influence the magnetic interaction greatly, **Ref-3** and **Ref-7** reveal similar magnetic properties. Though we do not have enough evidence to derive conclusive magneto-structural relationships in terms of the ferromagnetic interactions in dinuclear Dy^{III} complexes at this moment, it would be very interesting to further investigate this topic.

As the most important and valuable property, the effective energy barrier of these didysprosium complexes should be highlighted (Figure 2.21). However, as a consequence of the lack of computational study for most of the systems, it is almost impossible to figure out the connection between structures, orientation of their anisotropic axes and the corresponding barriers. We believe that by further investigating these systems, we can potentially reveal the origin of ferromagnetism and even the relationship between molecule architecture and its effective energy barrier eventually.

2.5 Conclusion

In this chapter, we focused on designing and studying dinuclear Ln-SMMs with Schiff base ligands. Complexes **1-8** have been successfully synthesized with the rigid ligand H_2ovph. Comprehensive structural and magnetic studies reveal that Dy^{III} compounds **1**, **4**, **7** and **8** are SMMs with ferromagnetic intramolecular interactions between metal centers. The effective energy barriers are 58, 98, 110 K for **1**, **4** and **7**, respectively, and 22 (1200 Oe), 8 (2800 Oe) K for complex **8**. The Shape-measure approach was utilized for two solvent group complexes (**1** and **4**, as well as **3** and **6**) and also the asymmetric complexes **7** and **8** verified that clearly distinct coordination environments were present for different Dy^{III} ions, this has a significant effect on the observed difference in energy barriers.

To probe the origin of ferromagnetism in the μ-O bridged systems, structure-based analysis was demonstrated from angle, distance and geometry aspects. Unfortunately no sufficient evidence can be obtained in order to formulate a concise rule to obtain ferromagnetic interactions. For future work, we may expect more theoretical calculations to lead us close to the answer.

Table 2.5 Dinuclear Dy^{III} SMMs.

Formula	Code	Dy···Dy /Å	Dy-O-Dy /°	U_{eff}/K (external field)	Ref
$[Dy^{III}_2(ovph)_2(DMF)_2Cl_2]$	**1**	3.894	113.61	58	-
$[Dy^{III}_2(ovph)_2(IPA)_2Cl_2]$	**4**	3.854	112.40	98	-
$[Dy^{III}_2(ovph)_2(H_2O)_3(EtOH)Cl_2]$	**7**	3.954	113.25, 113.84	110	-
$[Dy^{III}_2(Hovph)_2(OH)Cl_3(H_2O)]\cdot 2H_2O$ ¤	**8**	3.835	106.68, 113.25	20 (1200 Oe)	-
$[Dy^{III}_2(ovph)_2Cl_2(MeOH)_3]\cdot MeCN$	**Ref-1**	3.864	112.32, 111.52	150/198	7
$[Dy^{III}_2(Hovph)(ovph)(NO_3)_2(H_2O)_4]\cdot NO_3\cdot 2CH_3OH\cdot 3H_2O$ ¤	**Ref-2**	3.893	111.20, 113.52	-	6
$[Dy^{III}_2(ovph)_2(NO_3)_2(H_2O)_2]\cdot 2H_2O$	**Ref-3**	3.826	110.12	69	6
$[Dy^{III}_2L^2(H_2L^2)(teaH_2)(o\text{-vanillin})(H_2O)](ClO_4)_2\cdot 2CH_3OH\cdot H_2O$ * ¤	**Ref-4**	3.549	94.19, 97.74, 103.55	Tail only	19
$[Dy^{III}_2(L^1)_2(NO_3)_2(MeOH)_2]\cdot 4CH_3CN$	**Ref-5**	3.923	114.88	41	9
$[Dy^{III}_2(L^3)_2(acac)_2(H_2O)]\cdot 2CH_2Cl_2$ ¤	**Ref-6**	3.848	110.70, 110.97	36/80(1000 Oe)	17
$[Dy^{III}_2(L^4)_2(NO_3)_2(MeOH)_2]$ ¤	**Ref-7**	3.750	106.41	56	15
$[Dy^{III}_2(HL^5)_3(NCS)_3]\cdot 2MeOH\cdot py$ * ¤	**Ref-8**	3.556	96.13, 100.86, 101.08	-	16
$Na[Dy^{III}_2(Hovph)_2(\mu 2\text{-}OH)(OH)(H_2O)_5]\cdot 3Cl\cdot 3H_2O$ * †¤	**Ref-9**	3.615	92.14, 99.72, 100.08	-	6
$[Dy^{III}_2(L^6)_2(NO_3)_2]$ †¤	**Ref-10**	3.768	108.22	76	18

H_2L^1 = N'-((2-hydroxy-1-naphthyl)methylene) picolinohydrazide; H_2L^2 = *N,N'*-bis(3-methoxysalicylidene)-1,2-cyclohexanediamine; H_2L^3 = N,N-bis(salicylidene)-*o*-phenylenediamine; H_2L^4 = (2-hydroxy-3-methoxyphenyl)methylene (isonicotino)hydrazine; H_2L^5 = *N'*-(2-hydroxy-3-methoxybenzylidene)benzhydrazide; H_2L^6 = *N*1,*N*3-bis(3-methoxysalicylidene)diethylenetriamine.

"*" Represents complexes with more than two μ-O bridges; "†" represents systems revealed antiferromagnetic interaction; "¤" represents the complexes contained phenoxy oxygen bridge(s).

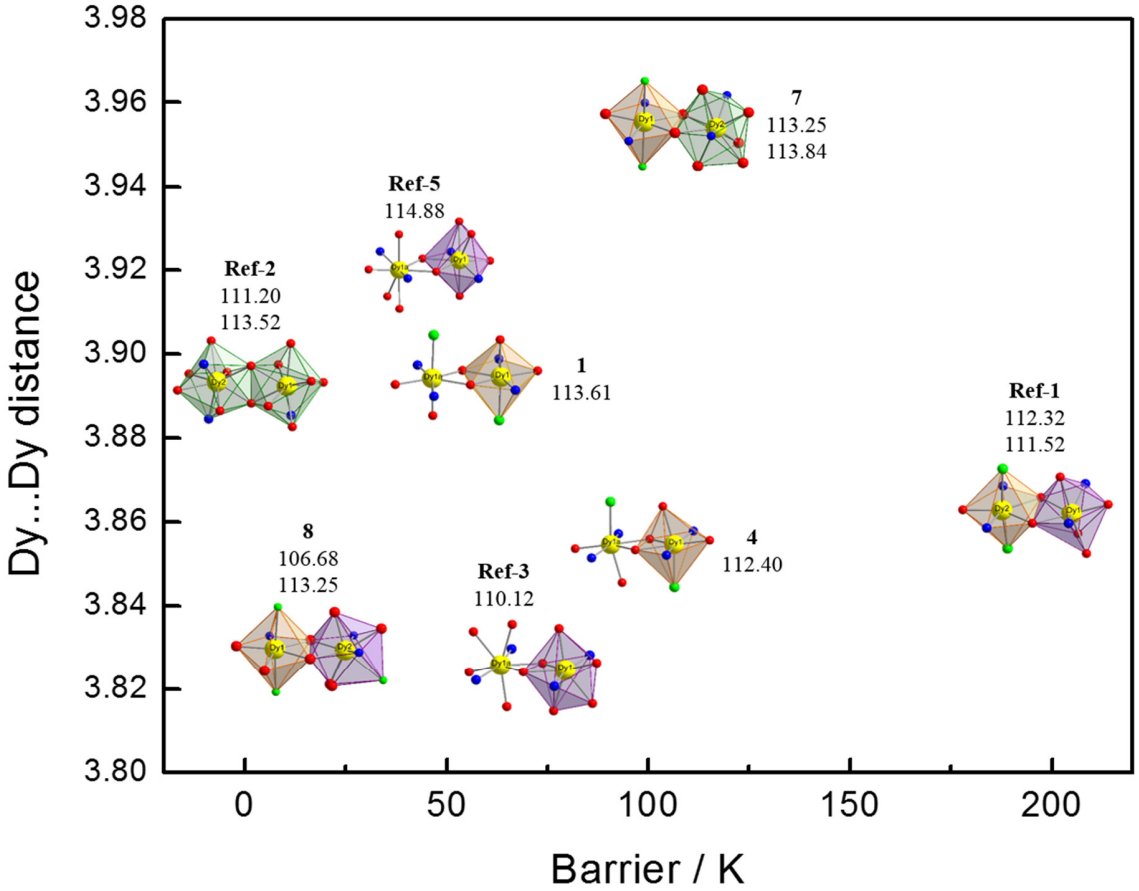

Figure 2.21 Plot demonstrating the relationship between Dy···Dy distance, Dy-O-Dy angle (values shown beneath compound labels), coordination polyhedron and effective energy barrier for few complexes in **Table 2.5**. Polyhedron color code: orange (seven-coordinate), purple (eight-coordinate) and green (nine-coordinate).

2.6 References

[1] (a) J. D. Rinehart, M. Fang, W. J. Evans, J. R. Long. *Nat. Chem.*, **2011**, *3*, 538-542. (b) J. D. Rinehart, M. Fang, W. J. Evans, J. R. Long. *J. Am. Chem. Soc.,* **2011**, *133*, 14236-14239.

[2] N. Ishikawa, S. Otsuka, Y. Kaizu. *Angew. Chem. Int. Ed.,* **2005**, *44*, 731-733.

[3] F. Habib, P. H. Lin, J. Long. I. Korobkov, W. Wernsdorfer, M. Murugesu. *J. Am. Chem. Soc.,* **2011**, *133*, 8830-8833.

[4] F. Habib, J. Long. P. H. Lin, I. Korobkov, L. Ungur, W. Wernsdorfer, L. F. Chibotaru, M. Murugesu. *Chem. Sci.*, **2012**, *3*, 2158-2164.

[5] D. N. Woodruff, R. E. P. Winpenny, R. A. Layfield. *Chem. Rev.*, **2013**, *113*, 5110-5148.

[6] Y. N. Guo, X. H. Chen, S. F. Xue, J. K. Tang. *Inorg. Chem.,* **2011**, *50*, 9705-9713.

[7] Y. N. Guo, G. F. Xu, W. Wernsdorfer, L. Ungur, Y. Guo, J. K. Tang, H. J. Zhang, L. F. Chibotaru, A. K. Powell. *J. Am. Chem. Soc.,* **2011**, *133*, 11948-11951.

[8] Y. N. Guo, X. H. Chen, S. F. Xue, J. K. Tang. *Inorg. Chem.,* **2012**, *51*, 4035-4042.

[9] L. F. Zou, L. Zhao, P. Chen, Y. N. Guo, Y. Guo, Y. H. Li, J. K. Tang. *Dalton Trans.,* **2012**, *41*, 2966-2971.

[10] M. L. Liu, J. M. Dou, D. Q. Wang, D. C. Li. *Acta. Cryst.,* **2005**, *E61*, o3876-o3878.

[11] M. Seitz, A. G. Oliver, K. N. Raymond. *J. Am. Chem. Soc.,* **2007**, *129*, 11153-11160.

[12] A. H. Morrish. *The Physical Principles of Magnetism*, **1966**, Wiley, New York.

[13] A. F. Wells. *Structural Inorganic Chemistry,* **1984**, Oxford University Press, USA.

[14] G. Abbas, Y. Lan, G. Kostakis, C. E. Anson, A. K. Powell. *Inorg. Chim. Acta.*, **2008**, *361*, 3494-3499.

[15] P. H. Lin, T. J. Burchell, R. Clérac, M. Murugesu. *Angew. Chem. Int. Ed.*, **2008**, *47*, 8848–8851.

[16] A. J. Hutchings, F. Habib, R. J. Holmberg, I. Korobkov, M. Murugesu. *Inorg. Chem.,* **2014**, *53(4)*, 2102-2112.

[17] P. H. Lin, W. B. Sun, P. F. Yan, L. Ungur, L. F. Chibotaru, M. Murugesu. *Chem. Commun.*, **2011**, *47*, 10993-10995.

[18] J. Long, F. Habib, P. H. Lin, I. Korbkov, G. Enright, L. Ungur, W. Wernsdorfer, L. F. Chibotaru, M. Murugesu. *J. Am. Chem. Soc.,* **2011**, *133*, 5319-5328.

[19] L. Zhang, P. Zhang, L. Zhao, S. Y. Lin, S. F. Xue, J. K. Tang, Z. L. Liu. *Eur. J. Inorg. Chem*., **2013**, *8*, 1351–1357.

[20] F. Habib, G. Brunet, V. Vieru, I. Korobkov, L. F. Chibotaru, M. Murugesu. *J. Am. Chem. Soc.,* **2013**, *135*, 13242-13245.

Chapter 3

Trigonal Prism-Assembled Hexanuclear Dy^{III} and Gd^{III} Complexes

3.1 Introduction

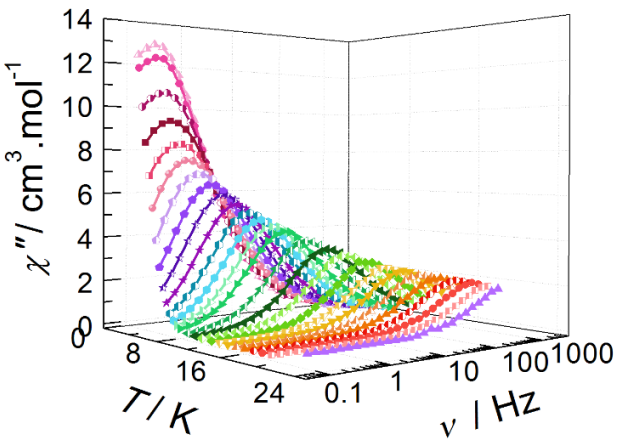

In the previous chapter, we have introduced the centrosymmetric ferromagnetically-coupling dinuclear Dy^{III} complex **4**, which behaves as an SMM with an effective energy barrier of 98 K. Herein, a polynuclear dysprosium cluster has been assembled with the same coordination moieties, and due to the presence of a carbonate ligand which sets up the bridging triangle core, the structure has been stabilized and formed. Instead of intentional design, this compound was actually isolated by accident from base trial reactions for the former complex. This kind of reaction is known as serendipitous synthesis. The first synthetic organic chemical dye, mauveine, was discovered by this approach in 1856. [1, 2] Though it may sound rare, these occasional "happy accident" have broadened our knowledge of science and even become a powerful technique to develop new theories or advance an existing method. For instance, the discovery of penicillin's antibiotic properties by Nobel laureate Alexander Fleming, began with a serendipitous observation and led to the blooming of the field of antibiotics. [3] Focusing on an inorganic discipline, serendipitous self-assembly [4] is a widely accepted

synthetic method to obtain high-nuclearity coordination complexes. [5] Our work will be presented as a good example here. Along with the unpredicted assembly approach, carbon dioxide soaked in the solvents or absorbed from air plays a major role in the formation of this complex. The coordination chemistry involving CO_2 [6] has been of major interest, especially for metal organic frameworks (MOFs) [7] CO_2 absorption [8] and relevant catalysis applications. [9] It might be impractical to relate our work to the giant picture of CO_2 chemistry, and yet the static and dynamic magnetic properties of this complex will make an important contribution to the rising field of SMMs. It is not surprising to see similar construction from literatures related to our work, especially as we all know, the competition in science is always intense. Particularly, works done by Tang's group which were generated using the same ligand gave compounds $[Dy_6(OAc)_3(\mu_3\text{-}CO_3)_2(ovph)_5(Hovph)(MeOH)_2]\cdot 4H_2O\cdot 5MeOH\cdot EtOH$ [10] (**Ref-11**) and $[Dy_6(ovph)_4(Hovph)_2Cl_4(H_2O)_2(CO_3)_2]\cdot CH_3OH\cdot H_2O\cdot CH_3CN$ [11] (**Ref-12**). It turns out that studying these complexes will give us a good chance to better understand our own system since we are sharing the same carbonate co-ligand. Because different solvent molecules involved in structures could change the energy barriers for each SMM, we synthesized the isotropic Gd analogue **10** to compare. A comparison to the literature will be presented after the detailed analysis of our work is discussed allowing us to acquire a better understanding of these unique structures and perhaps other useful information which can provide a guide to synthesizing better SMMs.

3.2 Structural Analysis

The single crystal X-ray studies reveal that complexes **9** and **10** are isostructural and crystallize in the monoclinic $P2_1/n$ space group (Table A.3, appendix A). The structure of the dysprosium analogue, complex **9** will be described as an example. The hexanuclear Dy^{III} compound can be considered as resulting from the combination of two carbonate-ligands and three Dy_2 units (Figure 3.2), forming a double layered trigonal prism (Figure 3.3), with a distance of 4.30 Å between C94 and C95 atoms as the cores of each triangular face. Furthermore, the average Dy···Dy distances in the double layers, which also represents the mean distance between Dy^{III} ions in each unit, is 3.86 Å.

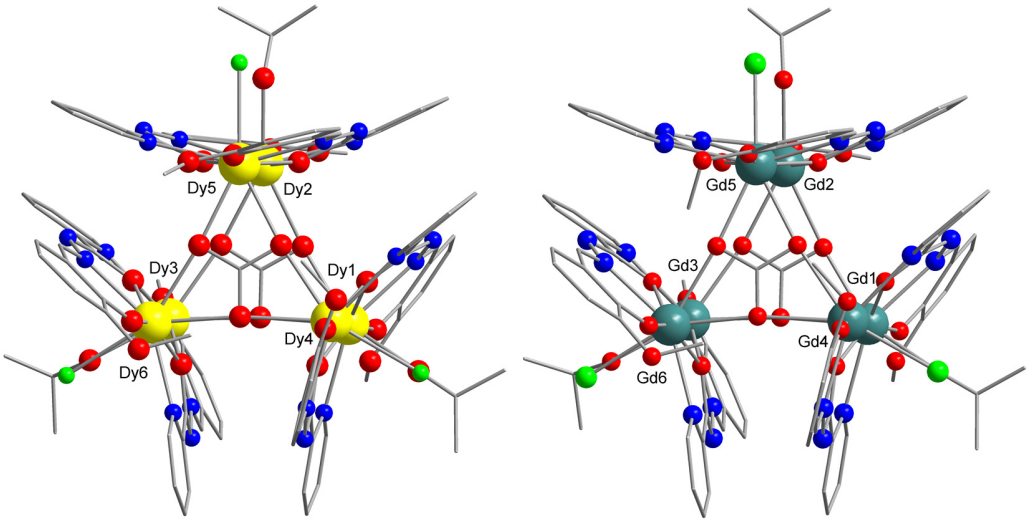

Figure 3.1 Labeled molecular structure of asymmetric complexes $[Dy^{III}_6(ovph)_6(IPA)_3Cl_3]\cdot 6MeCN\cdot IPA\cdot TEAOH$, **9**, left, and $[Gd^{III}_6(ovph)_6(IPA)_3Cl_3]\cdot 6MeCN\cdot TEAOH$, **10**, right, where H_2ovph= 2-hydroxy-3-methoxybenzaldehyde (pyridine-2-carbonyl) hydrazone. Color code: yellow (Dy), teal (Gd), red (O), blue (N), green (Cl) and grey (C). Hydrogen atoms and solvent molecules have been omitted for clarity.

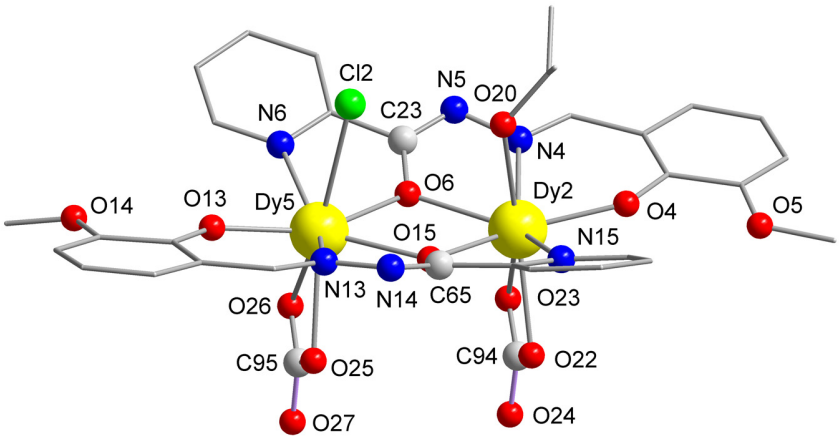

Figure 3.2 Labeled Dy_2 unit (Dy2···Dy5) structure of complex **9**, two carbonate-ligands (C94, C95) help to bridge the three units as linkers. Hydrogen atoms have been omitted for clarity. Color code: yellow (Dy), red (O), blue (N), green (Cl) and grey (C).

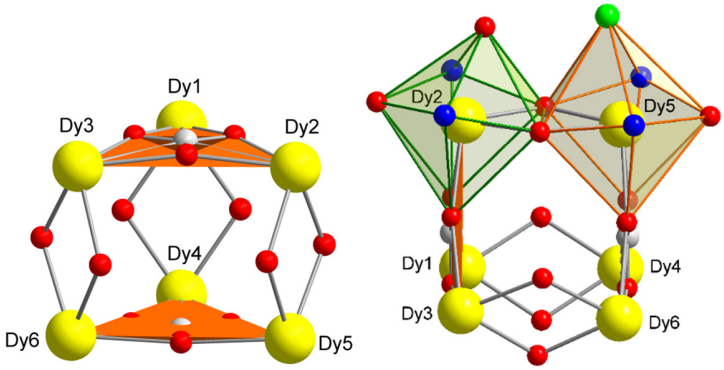

Figure 3.3 Left: the Dy_6 core structure for **9**. Right: Coordination polyhedra observed in **9**.

Additionally, the alkoxido groups (O6 and O15) play the role of bridging the Dy^{III} ions, with an average Dy-O distance being 2.33 Å, and Dy-O-Dy angles in the range of 111.4° to 112.2º. These values are in good agreement with previously reported works which have similar trigonal prism core structures using the same ligand system. [10, 11] Similar hendecahedron coordination polyhedron has been observed for all metal centers. By applying the shape measure approach, [12] based on the dihedral angles along the edges of the polyhedra for Dy2 and Dy5, respectively, a relatively large deviation close to 4.06° has been achieved.

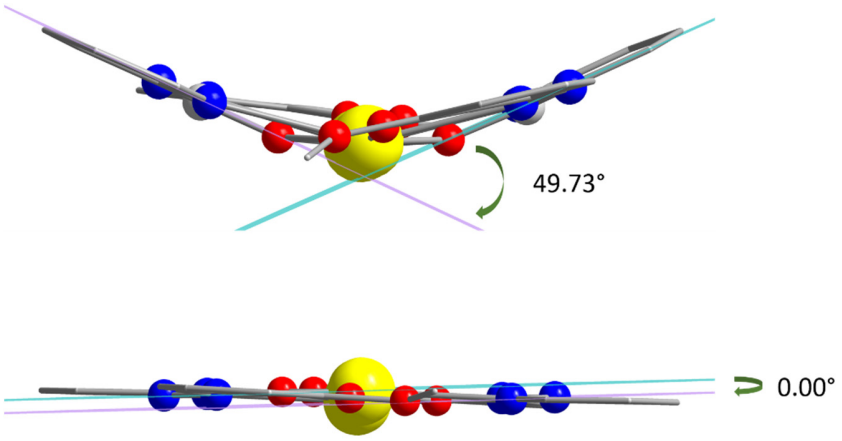

Figure 3.4 The bending angles between two ligand planes (defined as the plane built through three N and the bridging O atoms from each ligand) for Dy_2 unit (Dy2-Dy5) of **9** (top) and for dinuclear complex **4** (bottom).

It is worth mentioning that this deviation may exist between each one of the two Dy centers and leads to different relaxation pathways which could be further confirmed by ac measurements for complex **9**. Interestingly, the unit structure is consistent with complex **4** which possesses a centrosymmetric dinuclear Dy^{III} compound with one chloride ion and an isopropanol solvent molecule coordinated to each metal center (Figure 2.1). That complex **4** can be considered as the "skeleton" of this work. However, instead of the ligands being almost flat, bent ligands are observed and seem to be necessary to form large clusters with an average angle of 49.73° in **9** (Figure 3.4). Also, hydrogen bonds exist between the IPA oxygen atoms and chloride ions with an average distance of 3.03 Å, which is shorter than the corresponding value in complex **4** (3.15 Å).

3.3 Magnetic properties

3.3.1 Direct Current Magnetic Measurements

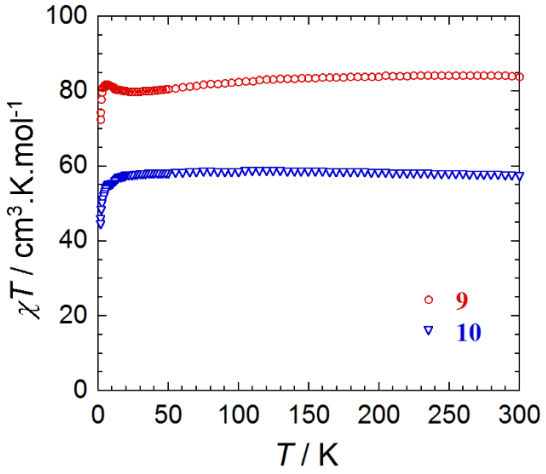

Figure 3.5 Temperature dependence of the magnetic susceptibility χT at 1000 Oe for complexes **9** (red) and **10** (Blue).

Direct current (dc) magnetic measurements have been performed for complex **9** under 1000 Oe dc-applied field, where a weak ferromagnetic intramolecular interaction was clearly observed (Figure 3.5). The χT value of 83.90 cm^3 K mol^{-1} at 300 K is in reasonable agreement with the expected value for six isolated Dy^{III} ions ($^6H_{15/2}$, S=5/2, χT= 85.02 cm^3 K mol^{-1}). The χT product remains nearly constant with decreasing temperature

where it drops slightly in the temperature range of 26-120 K. This could be mainly due to the depopulation of excited Stark sub-levels and/or from the presence of large anisotropy in the system. [13] With further decreasing of the temperature, the χT value then increases up to value of 81.87 cm^3 K mol^{-1} at 5.5 K, after which χT decreases again to a minimum value of 72.44 cm^3 K mol^{-1} at 1.8 K. This can be attributed to the depopulation of the crystal field splitting energy levels. [14] The field dependence of the magnetization curves below 7 K have been plotted for complexes **9** as shown in Figure 6, non-saturation of the magnetization indicates the presence of significant magnetic anisotropy and/or low-lying excited states in the system. This can be further confirmed by the lack of superposition and high field variation on a single master curve of M vs. HT^{-1} plots. The value of the magnetization at 1.8 K and 7 T is 28.79 μ_B, which is much lower than the expected saturation value of 60 μ_B for six non-interacting Dy^{III} ions. [15] The difference is possibly due to significant anisotropy and crystal-field effects eliminating the 16-fold degeneracy of the $^6H_{15/2}$ ground state. [16]

For the Gd^{III} analogue **10**, a typical antiferromagnetic interaction has been obtained with a room temperature χT value of 57.18 cm^3 K mol^{-1} (Figure 3.5). The theoretical spin only value for six non-interacting Gd^{III} ions is 47.28 cm^3 K mol^{-1} ($^8S_{7/2}$, $S = 7/2$, $L = 0$, $g = 2$), and thus is lower than experimental value.

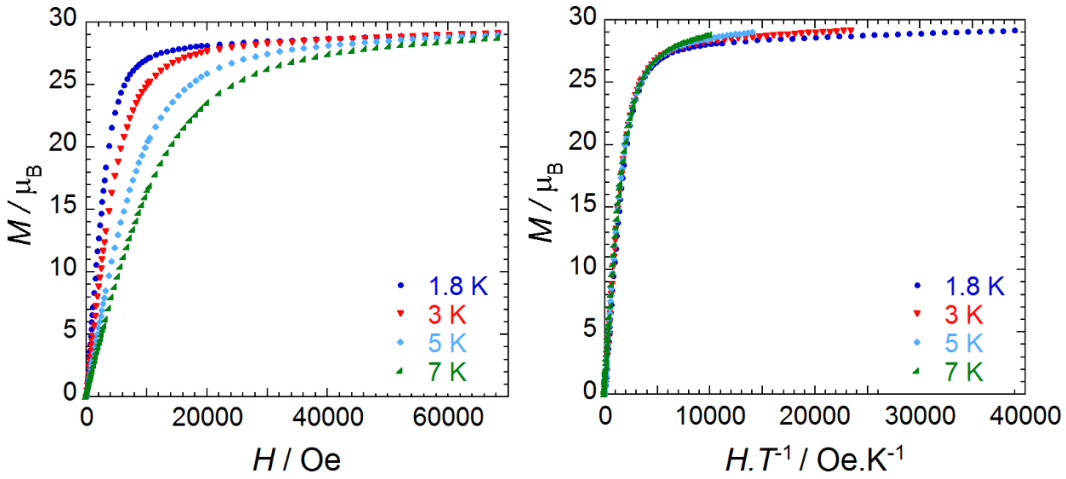

Figure 3.6 Field dependence of the magnetization M at 1.8, 3, 5 and 7 K for complex **9** plotted as M *vs.* H and M *vs.* HT^{-1}.

3.3.2 Alternating Current Magnetic Measurement

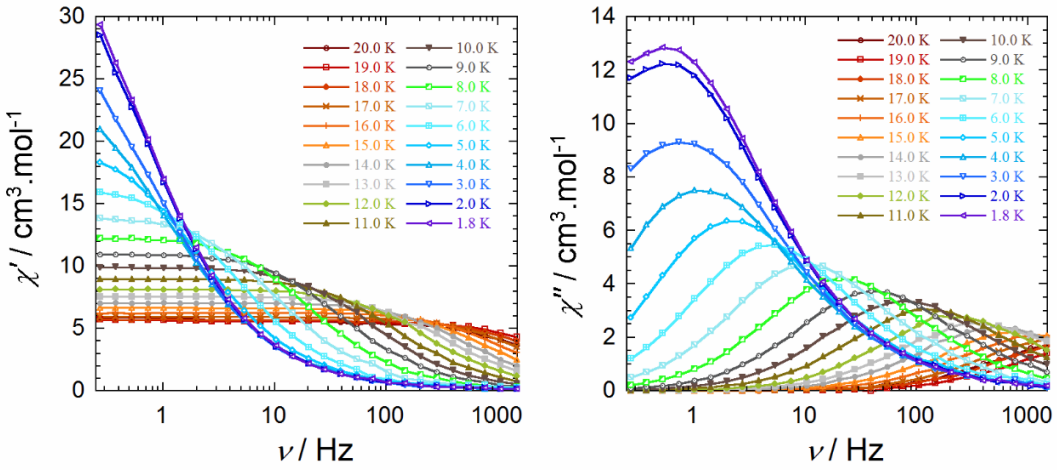

Figure 3.7 Frequency (υ) dependence of the in-phase (*χ'*, left) and out-of-phase (*χ''*, right) magnetic susceptibility at the indicated temperatures for **9** under zero applied dc field.

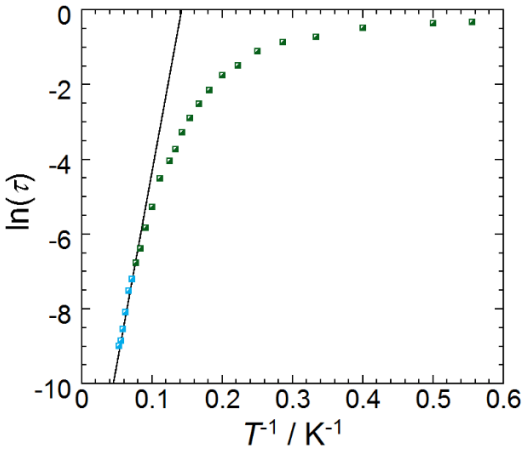

Figure 3.8 Relaxation time of the magnetization *ln(τ) vs.* T^{-1} at zero dc field for complex **9**. The anisotropic barrier (obtained by fitting this data using the Arrhenius law, $\tau = \tau_0 \exp(U_{eff}/kT)$) was calculated to be U_{eff}=102 K (τ_0=5.18*10^{-7} s).

In order to investigate the existence of slow magnetization relaxation, ac measurements were carried out on complex **9**. Under zero applied dc field, the temperature and frequency dependence ac susceptibility signals clearly indicate the SMM nature of this complex. Both the in-phase (*χ'*) and out-of-phase (*χ''*) susceptibilities measurements were performed in the temperature range of 1.8-20 K (Figure 3.7), and the latter exhibits peak

shifting with decreasing temperatures which is evidence of slow magnetization relaxation. The anisotropic energy barrier can be obtained by fitting the data using the Arrhenius equation ($\tau = \tau_0 \exp(U_{eff}/kT)$) from the high temperature regions of the relaxation plot, yielding a barrier of 102 K with a pre-exponential factor $\tau_0 = 5.18*10^{-7}$ s (Figure 3.8).

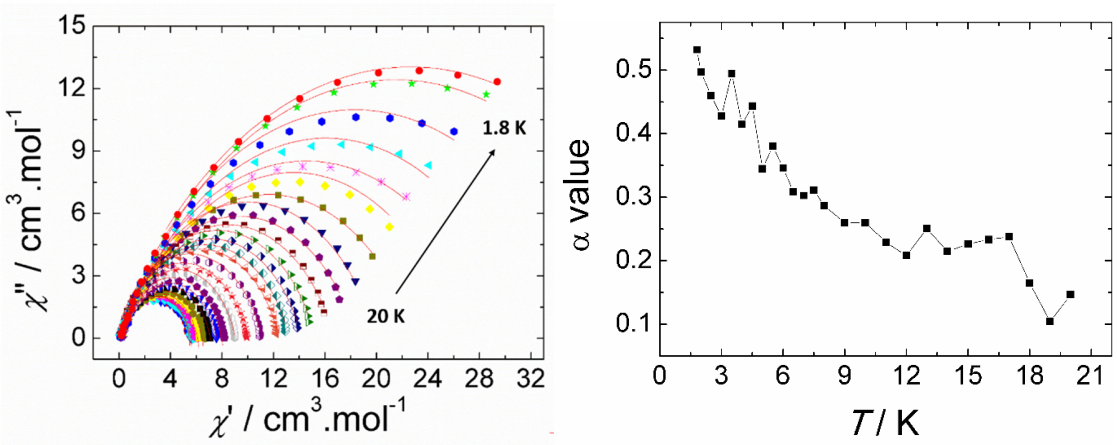

Figure 3.9 Cole-Cole plot using the ac susceptibility data for complex **9** (left) and the obtained α values from the fit using a generalized Debye model plotted as α *vs.* T (right).

The Cole-Cole plot has been achieved by taking χ'' versus χ' and fitting the semicircles with a generalized Debye model. The obtained α parameters have an average value of 0.24 in temperature range of 6-20 K (Figure 3.9). With further decreasing of the temperature, α values increase dramatically and reach 0.53 at 1.8 K which indicates a large width of the distribution in this relaxation processes suggesting that multiple relaxation processes could be involved. [17] For future work, to give stronger evidence of this, in-field measurements to reduce QTM would be an ideal choice. [18]

3.4 Three Close but Different Trigonal Prism {Dy_6} Systems

Due to the sensitive nature of Schiff base ligand reactions with lanthanides, different structures could be generated under slightly different synthetic conditions. For instance, $[Dy_6(OAc)_3(\mu_3\text{-}CO_3)_2(ovph)_5(Hovph)(MeOH)_2]\cdot 4H_2O\cdot 5MeOH\cdot EtOH$ (**Ref-11**) and $[Dy_6(ovph)_4(Hovph)_2Cl_4(H_2O)_2(CO_3)_2]\cdot CH_3OH\cdot H_2O\cdot CH_3CN$ (**Ref-12**) were formed in

different dysprosium salt, solvent and base sources. Including compound **9**, these three share the same Dy_6 core structure as described earlier, however, the coordinating solvent molecules, which complete the coordination environments of the Dy^{III} ions are different (Figure 3.10). As a consequence, the resulting magnetic anisotropy which highly depends on the orientation of local axes might change from one to another. Detailed comparison will be presented from structural differences, packing schemes and magnetism three different aspects, respectively.

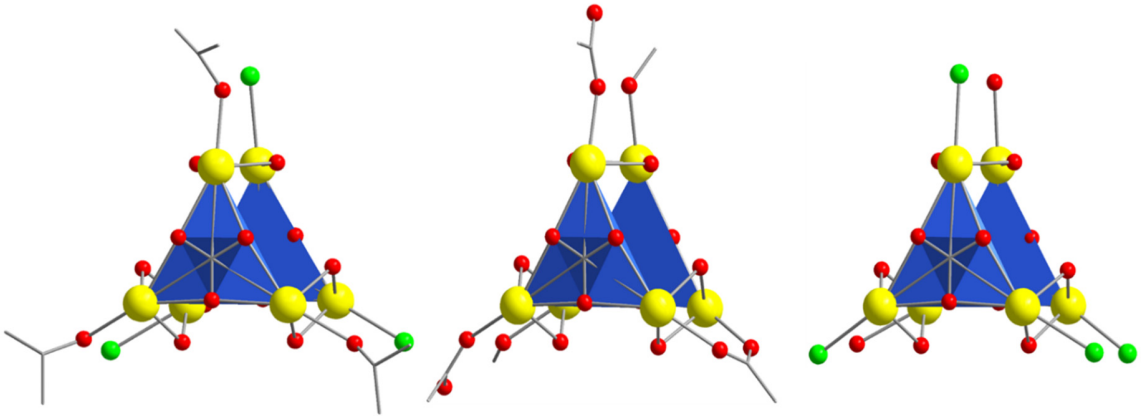

Figure 3.10 Core structures with coordinated solvent molecules of complexes **9**, **Ref-11** and **Ref-12** (from left to right). Color code: yellow (Dy), red (O), green (Cl) and grey (C). Hydrogen atoms have been omitted for clarity.

Firstly, the structural differences must be pointed out. As mentioned above, the Dy dinuclear unit of complex **9** (Figure 3.2) is bridged by the alkoxido groups (O6 and O15) of two antiparallel ligands, and we believe that each ligand is doubly deprotonated. On one hand, the average length of the bridging C-O bonds (ex. C23-O16, C65-O15 in Figure 3.2) is 1.31 Å, which increased from the original C=O groups which exhibit a bond length of 1.22 Å. Meanwhile, the adjacent C-N bond became shorter from 1.35 Å of the free ligand to 1.29 Å after coordination, in other words, a C=N bond is formed. [19, 20] Besides, the phenolate oxygen atoms (ex. O4 or O13) are deemed as deprotonated as well by observing an average bond length of 1.31 Å (1.37 Å in the free ligand H_2ovph). Therefore, $ovph^{-2}$ can be concluded for all six ligands. Additional evidence can be provided when the charge balance requirement is taken into account and $ovph^{-2}$ is fulfilled. However, compounds **Ref-11** and **Ref-12** both contain multi deprotonated ligand states $Hovph^{-1}$ and $ovph^{-2}$.

Moreover, different anions (OAc^-, Cl^-) and solvent molecules (H_2O, MeOH) helped to complete the structures and coordination spheres. All these minute differences would influence other properties such as magnetic properties.

Table 3.1 Void volume calculations* for complexes **9**, **Ref-11** and **Ref-12**.

		9	**Ref-11**	**Ref-12**
Void volume		Before omitting solvent		
	% of unit cell volume	4.7	6.3	22.3
	/ Å^3	634.49	1429.59	2750.92
		After omitting solvent		
	% of unit cell volume	27.6	16.5	29.8
	/ Å^3	3731.95	3722.29	3677.58

*Probe Radius: 1.2 Å; Approx. Grid Spacing: 0.7 Å. Calculate voids using the contact surface.

Secondly, complex **9** contains certain amount of MeCN and IPA solvent molecules, while for **Ref-11** and **Ref-12**, MeOH, EtOH, water and MeCN molecules are also participating as part of the structure without direct coordinating to the metal ion. These differences in solvents could significantly influence the packing schemes, which can then possibly affect the intermolecular interactions and other magnetic properties. Therefore, it would be interesting to calculate how much "free" space that is non-occupied by the molecules, which can be approached by applying voids calculation. In another way, it also represents how much a structure depends on the solvent molecules to form its skeleton. The voids that exist in **9**, **Ref-11** and **Ref-12** have been calculated in two ways, before and after omitting solvent molecules, based on the contact surface (Table 3.1, Figure 3.11). As can be noticed from the formula, **Ref-12** contains less solvent molecules, as a consequence, its void space before and after omitting solvent does not change drastically. On the contrary, both **9** and **Ref-11** show around 3-5 fold increase of void volume after pulling off all the small molecules from their structures. These results may indicate that the solvent molecules that form in the space for **9** and **Ref-11** systems play crucial roles, which are rather dependent compared to **Ref-12**. Although all these three complexes contain four asymmetric units in one unit cell, their packing schemes are different from each other. The

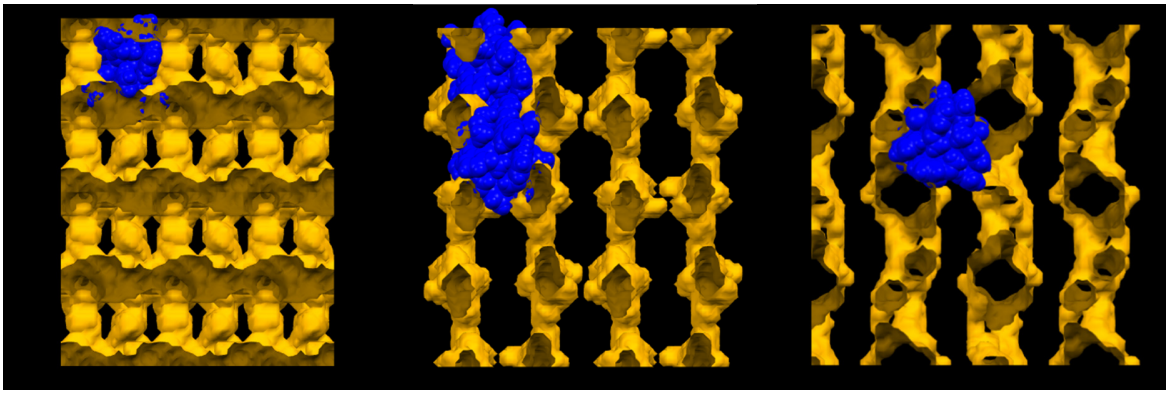

Figure 3.11 The void illustration (view down *a* axis) after omitting solvent molecules in the structures for **9**, **Ref-11** and **Ref-12** (from left to right, respectively). The structures are shown in blue, empty spaces (voids) are shown in yellow. According to the demonstration of voids, diverse packing schemes can be concluded as well.

closest intermolecular Dy···Dy distance is 9.56 Å for **9** (Figure 3.12). However, the presence of strong intermolecular hydrogen-bonding interactions in **Ref-11** leads to a one-dimensional supramolecular chain structure with the shortest metal center distance in the packing diagram as 8.82 Å, much closer than in **9**. As for complex **Ref-12**, one side of the trigonal prism contained two chloride ions, which force the formation of an asymmetric couple through their strong interactions, yielding the smallest packing distance with a value of 9.32 Å.

Thirdly, the dc measurement reveals highly similar magnetic susceptibility χT *vs.* T plots: ferromagnetic intramolecular interaction are observed for all three complexes with a low-temperature decrease which could be ascribed to the Stark sublevels depopulation. [13] The room temperature χT product of 85.02 cm^3 K mol^{-1} for **9** is in good agreement with **Ref-11** and **Ref-12** which are 85.78 and 82.10 cm^3 K mol^{-1}, respectively. Moreover, the magnetization values at 1.9 K and 7 T for the reported two complexes are higher than in our system, with values about 40 μ_B (**Ref-11**) and 32 μ_B (**Ref-12**), but are lower than the expected saturation value as well. Since the difference between calculated and experimental values is most likely due to the significant anisotropy and the crystal field effect, we might be able to conclude that the differences in the structures lead to such distinct results.

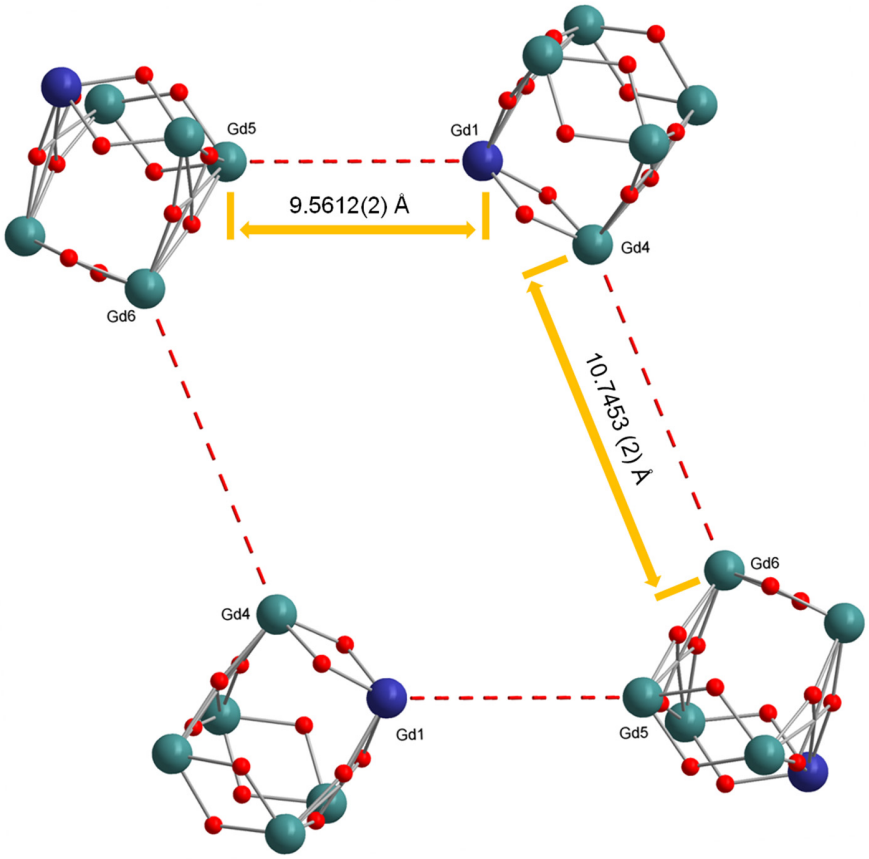

Figure 3.12 Illustration of the asymmetric units' arrangement in the unit cell for complex **10**, only core structures have been included for clarity. The distances between Gd1···Gd5, which also represents the shortest distance in packing, and Gd4···Gd6 are measured to be 9.56 and 10.75 Å, respectively. The shortest distance in packing for Dy analogue is 9.56 Å as well.

Lastly, the dynamic magnetic properties investigated by ac measurements also reveal similar behavior between the three complexes with distinct differences. They all reveal the presence of slow relaxation of magnetization, typical of SMMs under zero-dc field. For complex **Ref-11**, an estimation of the anisotropic barrier around 56 K has been obtained with the pre-exponential factor $\tau_0 = 6.6*10^{-6}$ s.

Notably, hysteresis loops were clearly observed for **Ref-11** under 5 K with measurements performed on a SQUID-VSM which further confirms the SMM nature of it. While for **Ref-12**, the effective energy barrier is relatively higher with a value of 76 K and

τ_0 = 1.2*10^{-6} s. At the same time, only a moderate increase of the α parameter from 0.1 to 0.23 under the temperature range of 16 to 1.9 K has been observed, clearly representing a narrow distribution of relaxation times. Compared to complex **9** which has much larger α values, the dominance of a single relaxation pathway was found in **Ref-12**. Such difference might be caused by the overall differences in the coordination sphere of the Dy^{III} ions in each compound.

It is noteworthy that without computational studies we are not able to clarify the alignment of anisotropy axes, or the energies of the excited states for Dy sites which could be associated with the multi relaxation processes. And due to the non-definitive magnetism data obtained for the gadolinium analogue, it would be difficult to determine the coupling constant between the metal centers. Despite these, such close structural arrangements unfolding on magnetic properties, present similar ferromagnetic intramolecular interactions and show SMM behaviors for all systems. However, the minute changes in these supramolecular architectures still may lead to changes in the local anisotropy and the effective energy barriers.

3.5 Conclusion

We have successfully synthesized a hexanuclear Dy^{III} cluster with a trigonal prism core structure by absorbing CO_2 from the surroundings, and also its Gd^{III} analogue. By applying ac measurements on the Dy complex **9**, its magnetic properties have been probed and SMM behavior was observed with an effective energy barrier of 102 K (τ_0 = 5.18*10^{-7} s). Careful comparison with previously published works, **Ref-11** and **Ref-12**, has been presented in three different areas, from structural-based multiformity to diverse magnetic behaviors. The high similarity in ligand construction for all three Dy complexes might be the cause of ferromagnetic intramolecular interactions, however the different solvents that coordinate to the metal centers as well as those found in the surroundings may have caused the differences observed in energy barrier values. We believe that the capture of atmospheric CO_2 was the key for building these architectures, and perhaps it could be a new effective approach to assemble polynuclear complexes in the future.

3.6 References

[1] K. Hübner. *Chem. Unserer. Zeit.,* **2006**, *40*, 274- 275.

[2] A. S. Travis. *Technology and Culture,* **1990**, *31(1)*, 51-82.

[3] J. Houbraken, J. C. Frisvad, R. A. Samson. *IMA Fungus*., **2011**, *Jun. 2(1)*, 87-95.

[4] R. E. P. Winpenny. *J. Chem. Soc., Dalton Trans*., **2002**, 1-10.

[5] M. Ledezma-Gairaud, L. Grangel, G. Aromí, T. Fujisawa, A. Yamaguchi, A. Sumiyama, E. C. Sañudo. *Inorg. Chem*., **2014**, *53*, 5878−5880.

[6] (a) W. Leitner. *Coord. Chem. Rev.,* **1996**, *153*, 257-284. (b) J. C. Calabrese, T. Herskovitz, J. B. Kineey. *J. Am. Chem. Soc.,* **1983**, *105*, 5914-5915. (c) H. S. Choi, M. P. Suh. *Angew. Chem. Int. Ed.,* **2009**, *48*, 6865-6869.

[7] (a) J. L. C. Rowsell, O. M. Yaghi. *Microporous Mesoporous Mater*., **2004**, *73*, 3-14. (b) S. Kitagawa, R. Kitaura, S. Noro. *Angew. Chem. Int. Ed.,* **2004**, *43*, 2334-2375. (c) G. Ferey. *Chem. Soc. Rev.,* **2008**, *37*, 191-214. (d) J. R. Li, R. J. Kuppler, H. C. Zhou. *Chem. Soc. Rev.,* **2009**, *38*, 1477-1504.

[8] J. An, N. L. Rosi. *J. Am. Chem. Soc.,* **2010**, *132*, 5578-5579.

[9] (a) S. D. Allen, D. R. Moore, E. B. Lobkovsky, G. W. Coates. *J. Am. Chem. Soc*., **2002**, *124*, 14284-14285. (b) Cheng, M.; Moore, D.; Reczek, J.; Chamberlain, B.; Lobkovsky, E. B.; Coates, G. W. *J. Am. Chem. Soc*., **2001**, *123*, 8738-8749. (c) Cheng, M.; Lobkovsky, E. B.; Coates, G. W. *J. Am. Chem. Soc*., **1998**, *120*, 11018-11019.

[10] H. Q. Tian, M. Wang, L. Zhao, Y. N. Guo, Y. Guo, J. K. Tang, Z. L. Liu. *Chem. Eur. J.,* **2012**, *18*, 442-445.

[11] Y. N. Guo, X. H. Chen, S. F. Xue, J. K. Tang. *Inorg. Chem.,* **2012**, *51*, 4035-4042.

[12] M. Seitz, A. G. Oliver, K. N. Raymond. *J. Am. Chem. Soc.*, **2007**, *129*, 11153-11160.

[13] J. Long, F. Habib, P. H. Lin, I. Korobkov, G. Enright, L. Ungur, W. Wernsdorfer, L. F. Chibotaru, M. Murugesu. *J. Am. Chem. Soc.*, **2011**, *113*, 5319-5328.

[14] M. L. Kahn, R. Ballou, P. Porcher, O. Kahn, J. P. Sutter. *Chem. Eur. J.,* **2002**, *8*, 525-531.

[15] W. B. Sun, B. L. Han, P. H. Lin, H. F. Li, P. Chen, Y. M. Tian, M. Murugesu, P. F. Yan. *Dalton Trans.,* **2013**, *42*, 13397-13403.

[16] (a) J. Tang, I. Hewitt, N. T. Madhu, G. Chastanet, W. Wernsdorfer, C. E. Anson, C. Benelli, R. Sessoli, A. K. Powell. *Angew. Chem*., **2006**, *118*, 1761–1765*; Angew. Chem. Int. Ed*., **2006**, *45*, 1729–1733. (b) S. Osa, T. Kido, N. Matsumoto, N. Re, A. Pochaba, J. Mrozinski. *J. Am. Chem. Soc.,* **2004**, *126*, 420-421.

[17] (a) F. Habib, J. Long. P. H. Lin, I. Korobkov, L. Ungur, W. Wernsdorfer, L. F. Chibotaru, M. Murugesu. *Chem. Sci.*, **2012**, *3*, 2158-2164. (b) P. H. Lin, W. B. Sun, M. F. Yu, G. M. Li, P. F. Yan, M. Murugesu. *Chem. Commun.,* **2011**, *47*, 10993-10995.

[18] P. H. Lin, T. J. Burchell, R. Clérac, M. Murugesu. *Angew. Chem.,* **2008**, *120*, 8980-8983.

[19] M. L. Liu, J. M. Dou, D. Q. Wang, D. C. Li. *Acta. Cryst.,* **2005**, *E61*, o3876-o3878.

[20] R. H. Petrucci, F. G. Herring, J. D. Madura, C. Bissonnette. *General Chemistry: Principles and Modern Applications,* **2010** (10th ed.), Pearson Canada, Toronto.

Chapter 4

Lanthanide Contraction within a Series of Centrosymmetric Dinuclear Complexes

4.1 Introduction

The heavy rare earth elements share a common outer electronic configuration, only differing in the number of 4*f* electrons that they possess. [1, 2] The filling of the 4*f* shell across the lanthanide series is accompanied by a considerable decrease in the ionic radii, known as lanthanide contraction, [3] which is mainly due to an incomplete shielding of the nuclear charge by the 4*f* electrons. [4] As proven before, minor changes in coordination chemistry can have significant implications on the physical characteristics and observed properties of the lanthanide complexes. [5] Instead of modifying the ligand or coordination environment, by applying different lanthanide ions into the same complex structure, only a handful of complexes will exhibit the same structures across the entire lanthanide series. More often, the result is a decrease in coordination number as the ionic radius shrink. [6] Multidentate Schiff base ligands which exhibit enough flexibility to accommodate ions of different sizes are always an exception, [5, 7] which is also the case in our system. Herein, an isostructural series of dinuclear centrosymmetric lanthanide complexes has been synthesized by using the ligand (E)-2-(dimethylamino)-N'-(2-hydroxy-3-methoxybenzylidene)-acetohydrazide (H_2ovgrd). All complexes have the formula $[Ln^{III}_2(ovgrd)_2(acac)_2(H_2O)_2]\cdot EtOH$, Ln = Gd (**11**), Dy (**12**), Ho (**13**), Er (**14**) and Yb (**15**), in which **11-13** crystalize in the monoclinic crystal system, while the last two are in

triclinic system. The magnetic behavior has been studied for all complexes, and interestingly, the Yb (**15**) analogue reveals SMM properties which is relatively rare to observe.

4.2 Structure Analysis

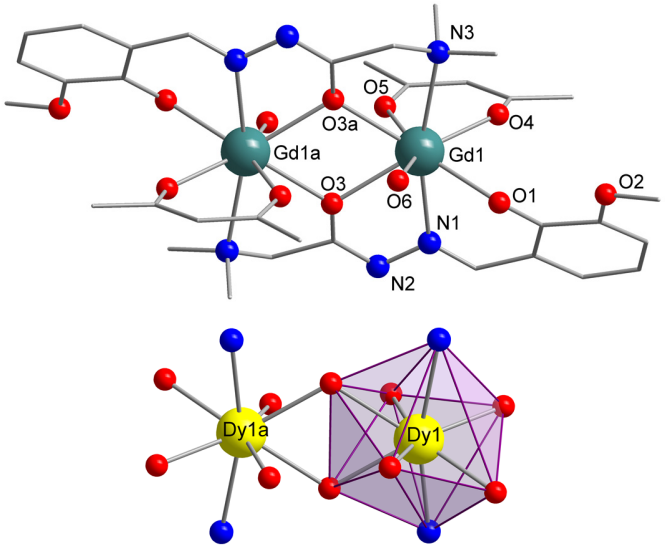

Figure 4.1 Labeled molecular structures of complexes $[Ln^{III}_2(ovgrd)_2(acac)_2(H_2O)_2]\cdot EtOH$, where Ln = Gd (**11**), Dy (**12**), Ho (**13**), and Er (**14**), H_2L = (E)-2-(dimethylamino)-N'-(2-hydroxy-3-methoxybenzylidene) acetohydrazide. Color code: Teal (Gd), yellow (Dy), red (O), blue (N) and grey (C). Hydrogen atoms and solvent molecules have been omitted for clarity. Bottom left: Coordination polyhedron observed in complex **12**. Dy1 exhibits distorted dodecahedron geometry.

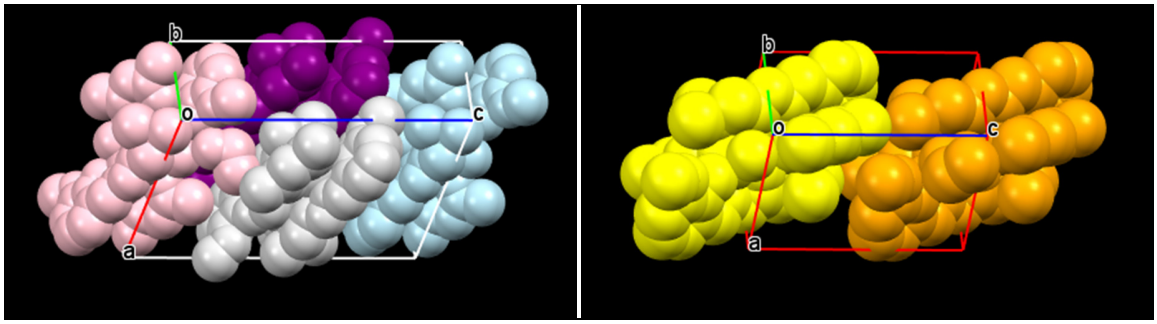

Figure 4.2 Spacefill packing diagrams of **11** (left) and **14** (right). Unit cell axes as shown.

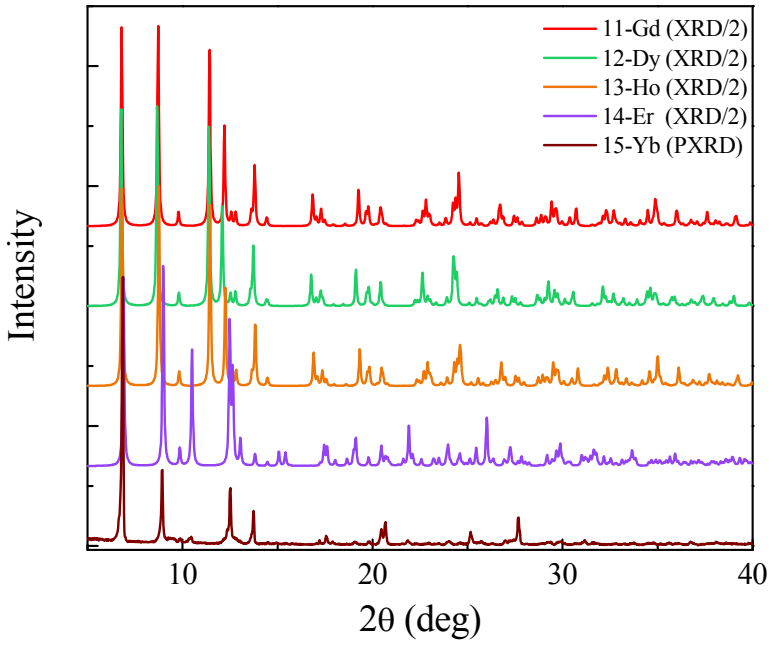

Figure 4.3 Powder X-ray diffraction comparison between the calculated patterns obtained from single crystal X-ray data of complex **11-14** and the experimental pattern (brown) of complex **15** in the 5-40° 2θ region. The calculated pattern was divided by a factor of 2 for comparative purposes.

The single crystal X-ray crystallography studies reveal that complexes **11-13** (Figure 4.1) are isostructural and crystallize in monoclinic $P2_1/n$ or $P2_1/c$ space group. By moving along the periodic table to erbium, the analogous compound **14** shows slightly different structural arrangement, specifically, its space group is $P\ \bar{1}$ (Table A.4, appendix A). For Yb (**15**), its structure has been proven by PXRD measurements and is in good agreement with complex **14** (Figure 4.3). Other than this, the high similarity in the structures may allow us to take the Dy analogue, **12**, as an example and to describe these structures fully. The dinuclear complex contains two eight-coordinate Dy^{III}, bridged by the alkoxido groups (O3, O3a) from two antiparallel doubly-deprotonated ligand, forming a centrosymmetric complex with the Dy···Dy distance being 3.98 Å and the Dy-O-Dy angle equal to 111.63° (Table 4.1). The end-on nitrogen (N3), hydrazide nitrogen (N1) and the phenolate oxygen (O1) also coordinate to the metal center. The coordination sphere for each Dy^{III} ion is then completed by an acetylacetone group (O4, O5) and one water molecule (O6) binding on each side, thus exhibits an overall N_2O_6 coordination

environment with distorted dodecahedral geometry (Figure 4.1). By carefully inspecting the packing arrangement (Figure 4.2), the shortest intermolecular Dy···Dy distance is found to be 8.39 Å.

Table 4.1 Selected bond distances (Å) and angles (°) for complex **11-14**

	11	**12**	**13**	**14**
Ln1···Ln1a	4.0057(3)	3.9775(1)	3.9615(5)	3.9271(5)
Ln1-O3	2.3759(2)	2.3439(1)	2.330(4)	2.312(4)
Ln1-O3a	2.4292(1)	2.4085(1)	2.402(4)	2.377(4)
Ln1-O1	2.2951(2)	2.2713(1)	2.274(4)	2.248(4)
Ln1-O4	2.3196(2)	2.3008(1)	2.363(4)	2.282(4)
Ln1-O5	2.4001(2)	2.3848(1)	2.289(4)	2.360(5)
Ln1-O6	2.3607(1)	2.3446(1)	2.330(4)	2.320(4)
Ln1-N1	2.4940(2)	2.4464(1)	2.438(5)	2.426(4)
Ln1-N3	2.6292(2)	2.5969(1)	2.581(5)	2.565(5)
C9-O3	1.2657(1)	1.3083(0)	1.309(7)	1.311(6)
C9-N2	1.2943(1)	1.2901(0)	1.292(8)	1.300(7)
C8-N1	1.2712(1)	1.2859(0)	1.285(9)	1.288(8)
O3-O3a	2.640(2)	2.602(5)	2.589(6)	2.563(5)
Ln1-O3-Ln1a	112.941(3)	111.633(2)	111.7(2)	111.762(3)
O4- Ln1-O5	70.445(3)	71.066(1)	71.5(1)	71.621 (3)
Packing	8.379(1)	8.3937(5)	8.3607(7)	8.5864(7)

4.3 Magnetic properties

4.3.1 Direct Current Magnetic Measurements

The χT *vs.* T curve of the Gd analogue **11** reveals a decrease of the χT product with decreasing temperatures (Figure 4), the metal centers interact in an antiferromagnetic fashion. A room temperature χT value of 15.84 cm^3 K mol^{-1} is observed for **11**, in good agreement with the expected value for two uncoupled Gd^{III} ions ($^8S_{7/2}$, $S = 7/2$, $\chi T = 15.76$ cm^3 K mol^{-1}). Moreover, due to the isotropic nature of the Gd^{III} ions, by applying the Van Vleck equation to Kambe's vector coupling scheme, the magnetic interactions between two metal centers can be quantified and calculated to be $J = -0.01$ cm^{-1} and $g = 2.01$ which is rather weak as expected for lanthanide complexes. [5b]

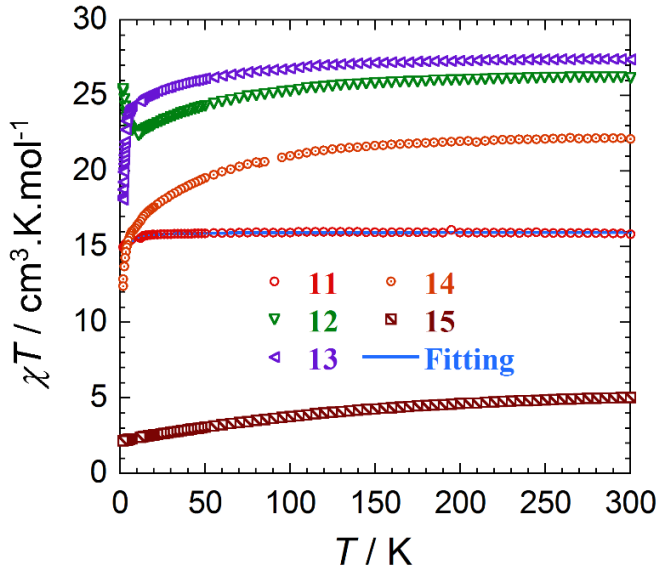

Figure 4.4 Temperature dependence of the magnetic susceptibility χT at 1000 Oe for complexes **11-15**. For Gd complex **11**, the best fit parameters (solid blue line) which reproduce the χT curve are J = -0.01 cm^{-1} and g = 2.01.

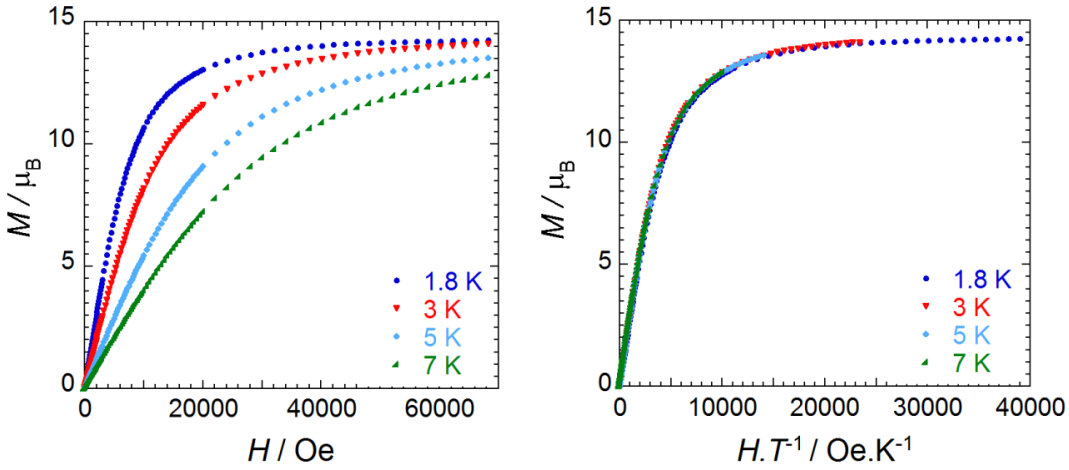

Figure 4.5 Field dependence of the magnetization M at 1.8, 3, 5, and 7 K for complex **11** plotted as M *vs.* H and M *vs.* HT^{-1}.

The field dependence of the magnetization at low temperatures shows that the magnetization rapidly increases with the applied dc field to approach a true saturation above 7 T at which it reaches the value of 14 μ_B (Figure 4.5). This true saturation reveals the absence of magnetic anisotropy within this complex. The superimposition of the M *vs.*

HT^{-1} data on a single mastercurve further confirm this result, which is expected for isotropic systems.

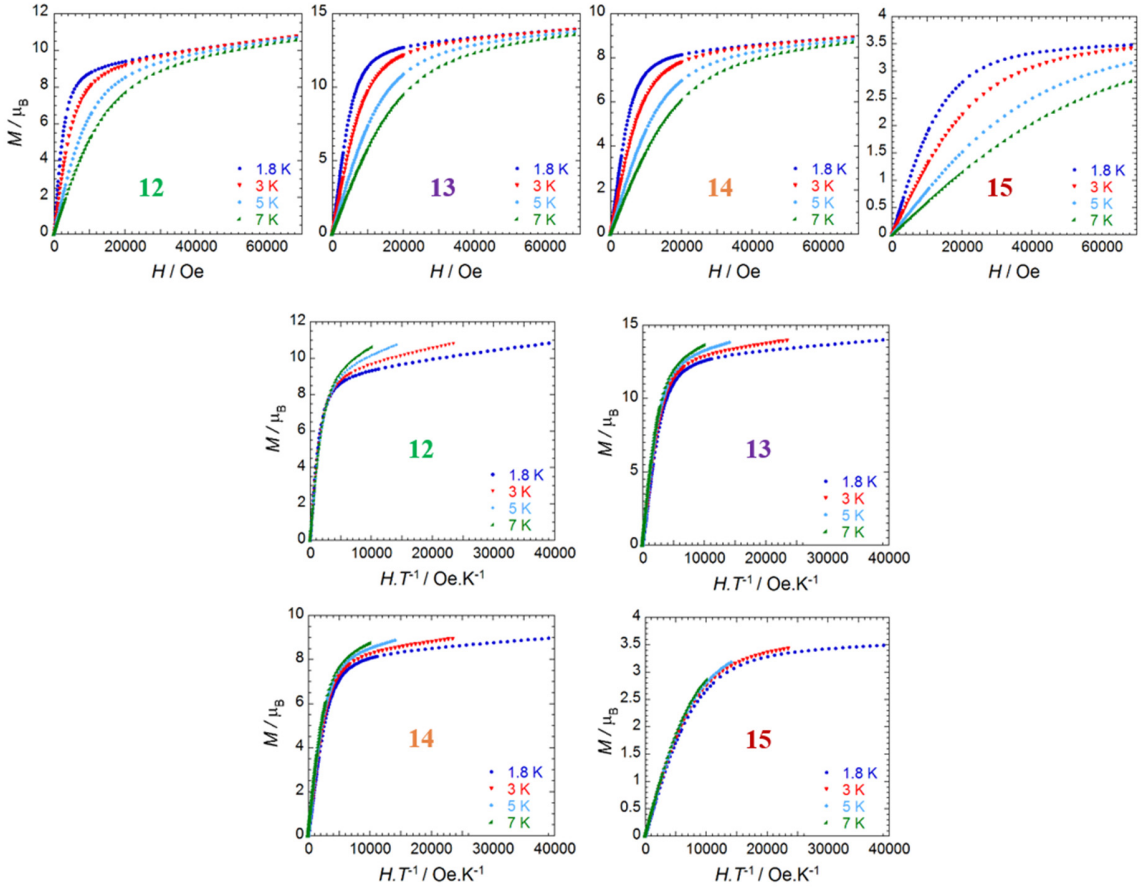

Figure 4.6 Field dependence of the magnetization M at 1.8, 3, 5, and 7 K for complex **12~15** plotted as M *vs.* H and M *vs.* HT^{-1}.

Direct current (dc) magnetic susceptibility studies of complex **12** reveal a room temperature χT value of 26.19 cm^3 K mol^{-1}, which is lower than the theoretical value for two non-interacting Dy^{III} ions ($^6H_{15/2}$, $S = 5/2$, $\chi T = 28.34$ cm^3 K mol^{-1}) (Figure 4.4). The χT product decreases gently with decreasing temperature reaching a minimum value of 22.41 cm^3 K mol^{-1} at 11 K, then increases sharply to a maximum value of 25.46 cm^3 K mol^{-1} at 1.8 K. The decrease is most likely caused by the depopulation of the Stark sublevels and/or significant magnetic anisotropy, while the latter increase can be attributed to weak ferromagnetic interactions between the Dy^{III} ions. The M *vs.* H data shows the field dependence of magnetization rising abruptly at low field, without saturating at higher

field then reaching a value of 10.83 μ_B under 7 T at 1.8 K, which is significant lower than the expected magnetization saturation value but in good agreement with the value of 5.23 μ_B per Dy^{III} ion in a crystal field environment [8] for two isolated Dy^{III} ions (Figure 4.6). This is most likely due to the crystal-field effect at the Dy^{III} ions. [10] Also the high-field variation and non-superposition on a single master curve of the *M vs. HT*$^{-1}$ data indicates the presence of significant magnetic anisotropy and/or low-lying excited states in this system. [9]

For Ho^{III} case, **13**, similar behavior as complex **11** has been obtained. The room temperature χT value is 27.39 cm^3 K mol^{-1} within good agreement as the expected value ($^5I_8$, S = 2, χT = 28.14 cm^3 K mol^{-1}). Following the decreasing of the temperature, χT product decreases gently before a sharp dropping at about 10 K, eventually reached the minimum value of 18.11 cm^3 K mol^{-1} at 1.8 K. This may suggest a weak antiferromagnetic intramolecular interaction and/or thermal depopulation of the Stark sublevels.

As for the Er^{III} analogue, **14**, the χT value at 300 K is 22.11 cm^3 K mol^{-1} which is in good agreement with the theoretical value for two uncoupled Er^{III} ions ($^4I_{13/2}$, S = 5/2, χT = 22.96 cm^3 K mol^{-1}) (Figure 4.4). When lowering the temperature, the χT product decreases gradually before a more drastic drop starts around 50 K, eventually a minimum value of 12.40 cm^3 K mol^{-1} is reached at 1.8 K. This result may point towards antiferromagnetic intramolecular interaction and/or thermal depopulation of the Stark sublevels.

The Yb^{III} complex, **15**, reveals a room temperature χT value of 5.03 cm^3 K mol^{-1}, in reasonable agreement with the theoretical value ($^2F_{7/2}$, S = 1/2, χT = 5.12 cm^3 K mol^{-1}) (Figure 4.4). Upon decreasing of the temperature, the χT value gradually drops and reaches a minimum value of 2.14 cm^3 K mol^{-1} at 1.8 K. Magnetization data for complex **15** behaves in a similar to **12-14**, with M = 3.49 μ_B under 7 T at 1.8 K.

4.3.2 Alternating Current Magnetic Measurements

To probe potential slow magnetic relaxation, alternating current measurements were carried out for complexes **12-15**. The Ho^{III} analogue does not exhibit an out-of-phase signal under the measurement conditions and hence does not behave as an SMM. The ac measurements analysis for **12**, **14** and **15** will be presented here.

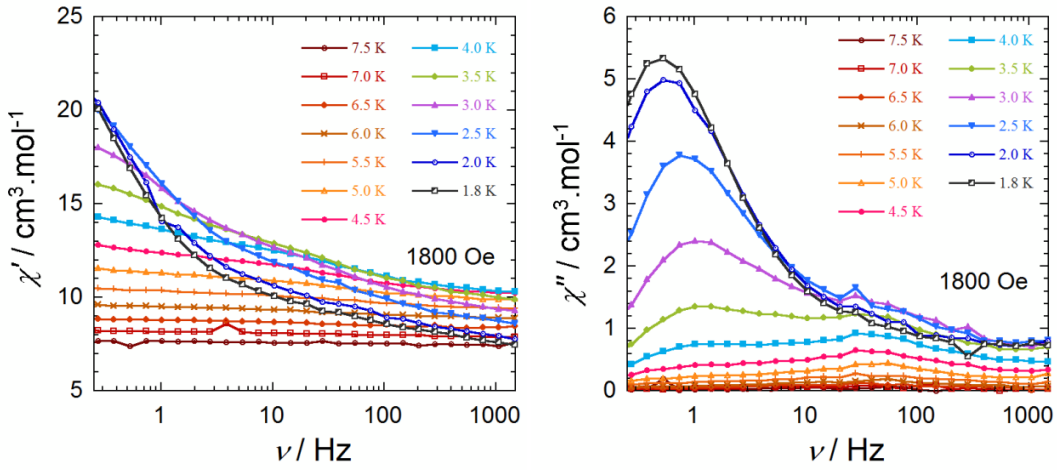

Figure 4.7 Frequency (υ) dependence of the in-phase (χ', left) and out-of-phase (χ'', right) magnetic susceptibility at the indicated temperatures for **12** under an applied optimum dc field of 1800 Oe.

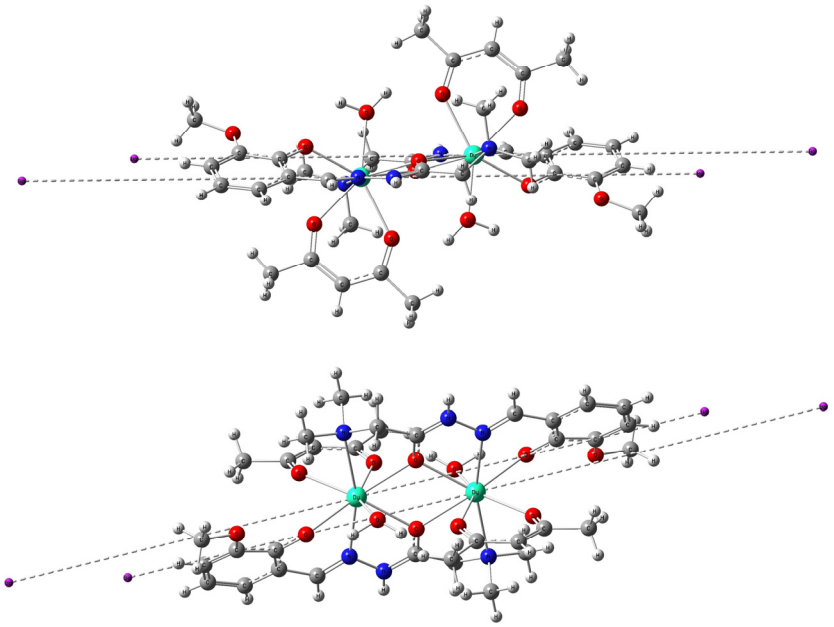

Figure 4.8 Orientations of the anisotropy axes (dashed lines) in **12**.

For complex **12**, significant quantum tunneling of the magnetization (QTM) [10] was observed under zero applied dc field, evident from the lack of clear full peaks. In order to minimize the QTM, ac susceptibility measurements were performed under an optimum field of 1800 Oe in the temperature range of 1.8-7.5 K (Figure 4.7). The presence of peaks shifting to lower frequency with decreasing temperatures, for the out-of-phase (χ'')

susceptibility, indicates potential SMM behavior. However, by fitting the magnetic data between 1.8 and 3.5 K with the Arrhenius equation ($\tau = \tau_0 \exp(U_{eff}/kT)$), an energy barrier of 3.3 K was obtained with a pre-exponential factor (τ_0) of 0.04336 s, suggesting that the QTM effect might be too efficient in this system such that the height of the barrier is compromised.

The *ab initio* calculations [11] on **12** may explain the reason for the low energy barrier (Table 4.2) when the neighboring Dy^{III} ion was replaced by diamagnetic Lu^{III}. The larger values of $\boldsymbol{g}_X$ and $\boldsymbol{g}_Y$ in the ground doublet of individual Dy^{III} ions indicate that this molecule may not be an SMM. The weak magnetic relaxation might still be observed in the presence of an applied magnetic field. Moreover, due to the small angle between local magnetic axes and the Dy-Dy direction, the dipole-dipole interaction in this compound is ferromagnetic, in agreement with the magnetic data (Figure 4.8).

Table 4.2 Energies (cm^{-1}) of the low-lying Kramers doublets (KD) of the ***g*** tensor in the ground KD and the main values of the ***g*** tensor in the ground KD obtained within basis set 2*.

J multiplet	**12**
$^6H_{13/2}$	0
	76
	127
	197
	274
	362
	413
	513
Main Values of the ***g*** Tensor in the Ground KD	
$\boldsymbol{g}_X$	0.3599
$\boldsymbol{g}_Y$	0.8904
$\boldsymbol{g}_Z$	18.4473

*Basis set 1: DZP quality (small-medium); Basis set 2: TZP quality (large).

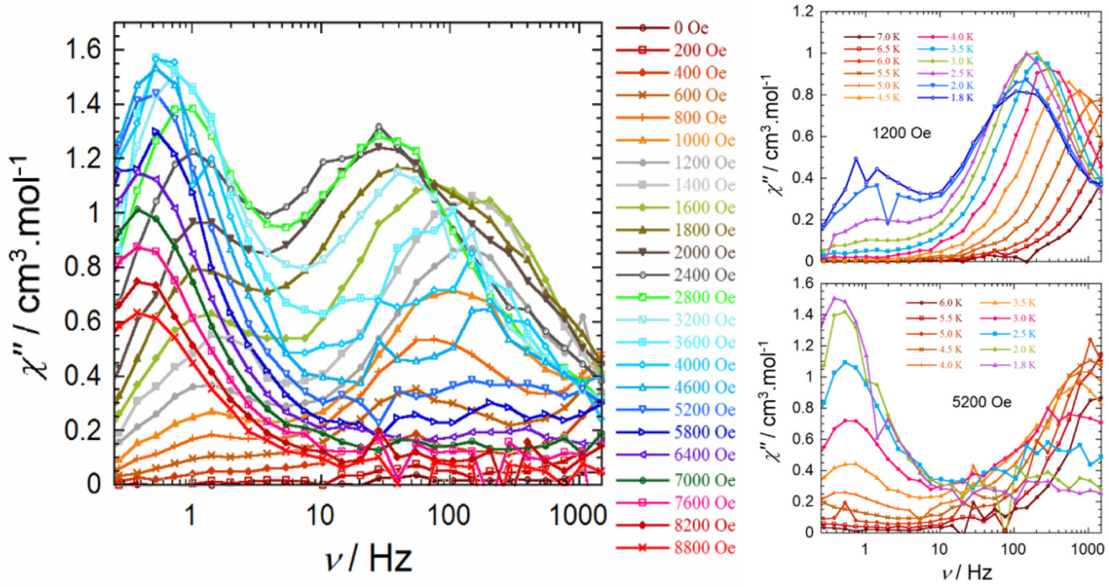

Figure 4.9 Left: Frequency (υ) dependence of the out-of-phase (χ'') magnetic susceptibility at the indicated applied dc field under temperature of 2 K for **14**. Right: Frequency (υ) dependence of the out-of-phase (χ'') magnetic susceptibility at the indicated temperatures for **14** under an applied static dc field of 1200 (top) and 5200 Oe (bottom).

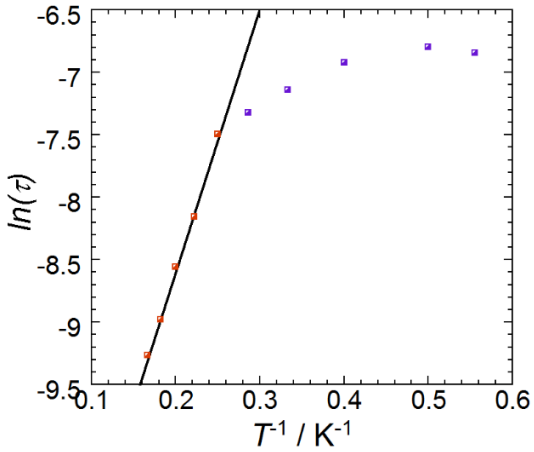

Figure 4.10 Relaxation time of the magnetization *ln(τ) vs.* T^{-1} at applied dc field of 1200 Oe for complex **14**.The anisotropic barriers (obtained by fitting this data using the Arrhenius law, $\tau = \tau_0 \exp(U_{eff}/kT)$) were calculated to be U_{eff} = 21 K ($\tau_0 = 2.75*10^{-6}$ s).

The Er^{III} compound **14** was studied under applied fields ranging from 0-8800 Oe at 2 K (Figure 4.9, left). With increasing of the static field, out-of-phase signals begin to appear at both high-frequency and low-frequency regions. The signal peaks observed at

higher frequency reveal a circuitous shifting which is uncommon and may indicate the occurrence of other type spin-lattice relaxations. [12] By applying the external fields of 1200 and 5200 Oe, two separate relaxation processes have been observed (Figure 4.9, right). The slow relaxation (high-frequency region) occurring under an applied field of 1200 Oe was fitted using the Arrhenius law, and an effective barrier of 21 K (τ_0 = 2.75*10^{-6} s) was calculated. The magnetic susceptibility χ'' under 5200 Oe results in two clear separate processes, at lower frequency the overlapping of peaks might mainly due to a QTM effect. The attempted fitting for high-frequency data gives a barrier value of 2 K with τ_0 = 7.37*10^{-5} s.

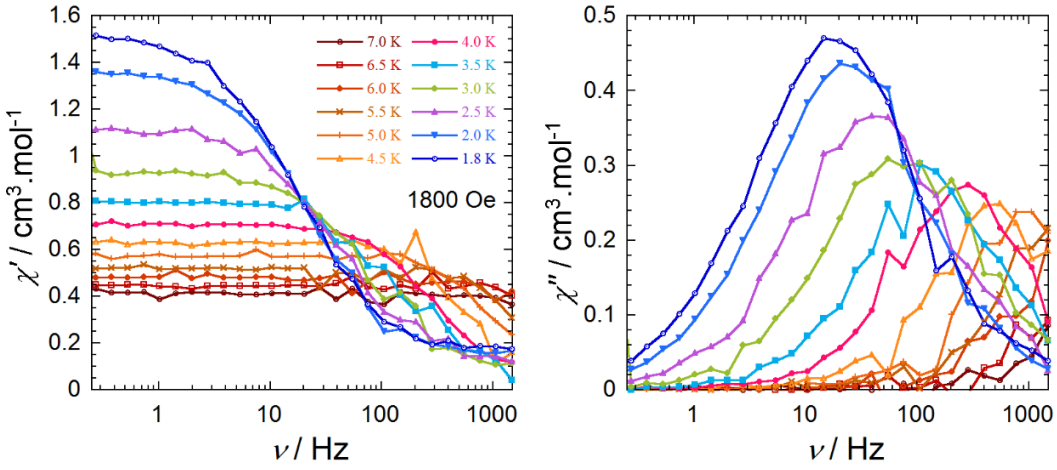

Figure 4.11 Frequency (υ) dependence of the in-phase (χ', left) and out-of-phase (χ'', right) magnetic susceptibility at the indicated temperatures for **15** under an applied optimum dc field of 1800 Oe.

The frequency scan of the ac susceptibility in zero dc field performed at 2 K for the Yb^{III} analogue **15** reveals the absence of any growing out-of-phase signal. However, the application of an external field of 1800 Oe successfully shifts the characteristic maximum of χ'' values to lower frequencies with full peaks observed (Figure 4.11). The relaxation time is extracted from the fit of the frequency dependence of the ac susceptibility data between 1.8 and 7 K. The temperature dependence of the relaxation time follows the Arrhenius law between 3.5 and 5.5 K with an energy barrier U_{eff} = 22 K and τ_0 = 2.13*10^{-6} s (Figure 4.12). Below 3.5 K, the relaxation time deviates from a thermally activated process possibly due to a direct process allowed in a low symmetry environment. [13]

Furthermore the distribution of the relaxation time, α, does not exceed 0.3 at lower-temperature and close to zero up to 5 K. [14]

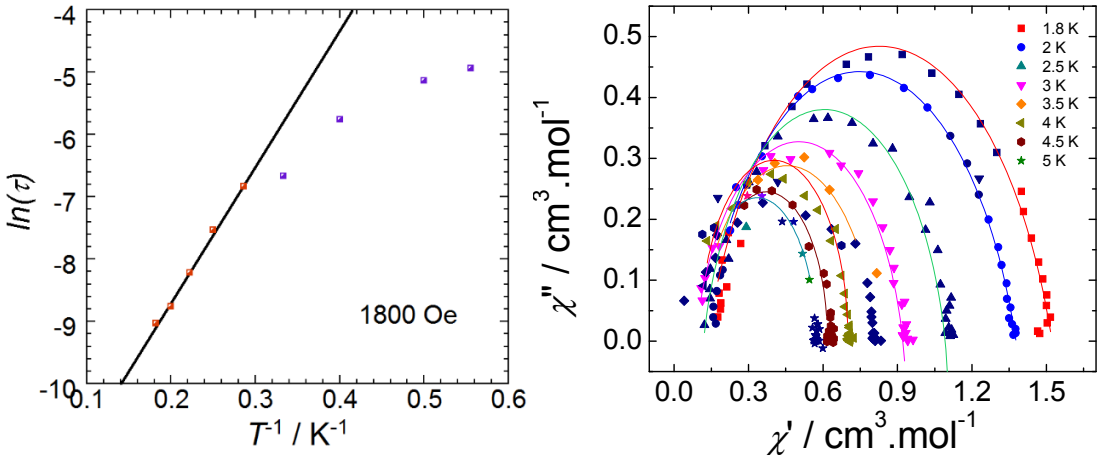

Figure 4.12 Left: Relaxation time of the magnetization *ln(τ) vs.* T^{-1} at an applied dc field of 1800 Oe for complex **15**.The anisotropic barriers (obtained by fitting this data using the Arrhenius law, $\tau = \tau_0 \exp(U_{eff}/kT)$) were calculated to be U_{eff} = 22 K (τ_0 = 2.13*10^{-6} s). Right: Cole-Cole plot using the ac susceptibility data.

4.4 Lanthanide contraction

The average Ln-X (X = O, N) distances for complexes **11-14** are calculated to be 2.59, 2.56, 2.55 and 2.54 Å, respectively. As expected, they follow the trend for the lanthanide contraction, that is, with increasing atomic number *n*, the average distance decreases. From previous reports, the decay of bond lengths with this contraction follows a quadratic decay as a function of the number *n* of *f* electrons. [15] Based on our systems, the centrosymmetric property allows us to simply deal with the Ln-X distances by taking the average value of Ln-O and Ln-N bonds distances. In another word, the Ln-X distances contraction study reveals individual metal center's behavior. The best-fit parameters are found to be: a = 2.6429, b = -0.0038 and c = -0.0005 with R^2 = 0.9946 to the quadratic function $F(n) = a + bn + cn^2$ (Figure 4.13).

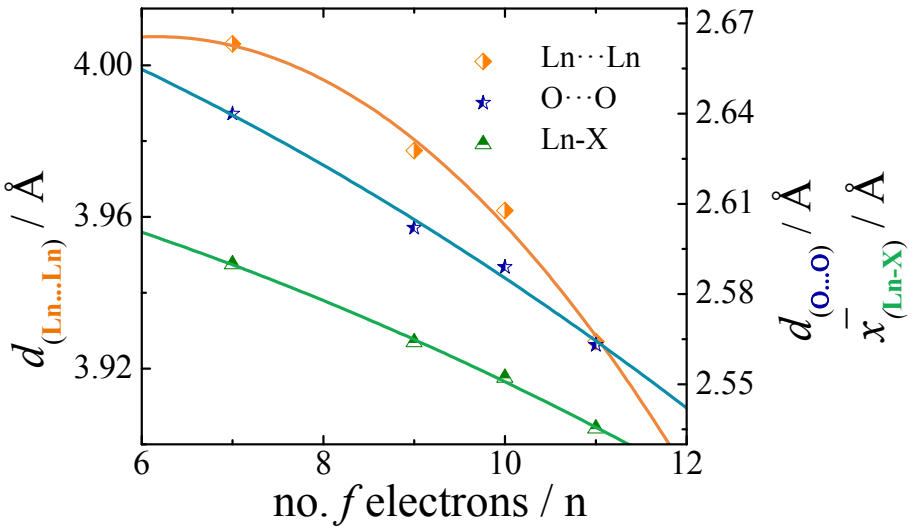

Figure 4.13 Graph of Ln···Ln distances, O···O distances and average Ln-X (X = O, N) bond lengths versus the number of 4*f* electrons (n) for complexes **11** to **14**. The solid lines are best fits to quadratic functions $F(n) = a + bn + cn^2$, demonstrating that these parameters follow quadratic decays with n. Best-fit parameters: a = 3.8793, b = 0.0414 and c = -0.0034 with R^2 = 0.9921; a = 2.7148, b = -0.0061 and c = -0.0007 with R^2 = 0.9923; a = 2.6429, b = -0.0038 and c = -0.0005 with R^2 = 0.9946, for $d_{(Ln\cdots Ln)}$, $d_{(O\cdots O)}$ and $\bar{x}_{(Ln\text{-}X)}$, respectively.

The $d_{(O\cdots O)}$ which represents the distance between oxygen atoms (O3···O3a) that are shared by the coordination polyhedra is analyzed jointly (Figure 4.13). Consequently, it results in a quadratic decay as well with the best-fit parameters of a = 2.7148, b = -0.0061 and c = -0.0007 with R^2 = 0.9923. Such observation could be attributed to the manifestation of the lanthanide contraction on parameters affected by two lanthanide atoms simultaneously. [16] This result must be further corroborated by plotting the dependence of Ln1···Ln1a distances on n, which exhibits similar behavior. The quadratic function parameters for $d_{(Ln\cdots Ln)}$ are: a = 3.8793, b = 0.0414 and c = -0.0034 with R^2 = 0.9921.

4.5 Conclusion

A series of centrosymmetric dinuclear lanthanide complexes has been employed to study the magnetic properties, as well as lanthanide contraction. The high flexibility of the multidentate ligand H_2ovgrd allows us to obtain complexes from Gd^{III} to Yb^{III} with the

same molecular architecture, but, different space groups and packing arrangements. By probing the magnetic properties, the gadolinium analogue, **11**, reveals a weak antiferromagnetic intramolecular interaction, with J = -0.01 cm^{-1} and g = 2.01. The Dy^{III} complex **12** is found not to be an SMM, which due to the larger values of $\boldsymbol{g}_X$ and $\boldsymbol{g}_Y$ in the ground doublet of individual Dy^{III} ions obtained via *ab initio* calculations. Additionally, the Yb^{III} complex **15** exhibits slow relaxation of the magnetization under an applied field with an effective energy barrier of 22 K, a relatively uncommon example of an SMM in this field. It would be interesting to complete the entire lanthanide series with the same structures for further investigation on the contraction behavior with possibly more accurate parameters obtained.

4.6 References

[1] K. A. Gschneidner, L. Eyring (eds). *Handbook on the Physics and Chemistry of Rare Earths*, **1978**, *Vol. 1*, North Holland, Amsterdam.

[2] I. D. Hughes, M. Däne, A. Ernst, W. Hergert, M. Lüders. J. Poulter, J. B. Staunton, A. Svane, Z. Szotek, W. M. Temmerman. *Nature*, **2007**, *446*, 650-653.

[3] (a) R. D. Shannon. *Acta. Crystallogr. A.*, **1976**, *32*, 751-767. (b) W. Küchle, M. Dolg. *J. Phys. Chem. A.*, **1997**, *101*, 7128-7113.

[4] P. S. Bagus, Y. S. Lee, K. S. Pitzer. *Chem. Phys. Lett.*, **1975**, *33*, 408-411.

[5] (a) F. Habib, J. Long. P. H. Lin, I. Korobkov, L. Ungur, W. Wernsdorfer, L. F. Chibotaru, M. Murugesu. *Chem. Sci.*, **2012**, *3*, 2158-2164. (b) A. J. Hutchings, F. Habib, R. J. Holmberg, I. Korobkov, M. Murugesu. *Inorg. Chem.,* **2012**, *53(4)*, 2102-2112.

[6] (a) A. Bowden, S. J. Coles, M. B. Pitak, A. W. G. Platt. *Inorg. Chem.*, **2012**, *51*, 4379-4389. (b) Y. Fukuda, A. Nakao, K. Hayashi. *J. Chem. Soc. Dalton Trans.*, **2002**, 527-533.

[7] (a) P. V. Bernhardt, B. M. Flanagan, M. J. Riley. *Aust. J. Chem.,* **2001**, *54*, 229-231. (b) K. Matsumoto, K. Suzuki, T. Tsukuda, T. Tsubomura. *Inorg. Chem.*, **2010**, *49*, 4715-4719. (c) M. Seitz, A. G. Oliver. K. N. Raymond. *J. Am. Chem. Soc.*, **2007**, *129*, 11133-11140.

[8] (a) J. K. Tang, I. Hewitt, N. T. Madhu, G. Chastanet, W. Wernsdorfer, C. E. Anson, C. Benelli, R. Sessoli, A. K. Powell. *Angew. Chem. Int. Ed.*, **2006**, *45*, 1529-1533. (b) J. Luzon, K. Bernot, I. J. Hewitt, C. E. Anson, A. K. Powell, R. Sessoli. *Phys. Rev. Lett.,* **2008**, *100*, 247205/1-247205/4.

[9] J. Long, F. Habib, P. H. Lin, I. Korobkov, G. Enright, L. Ungur, W. Wernsdorfer, L. F. Chibotaru, M. Murugesu. *J. Am. Chem. Soc.*, **2011**, *113*, 5319-5328.

[10] L. Thomas, F. Lionti, R. Ballou, D. Gatteschi, R. Sessoli, B. Barabara. *Nature,* **1996**, *383*, 145-147.

[11] F. Aquilante, V. L. De, N. Ferré, G. Ghigo, P. A. Malmgvist, P. Neogrády, T. B. Pedersen, M. Pitonák, M. Reiher, B. O. Roos, L. Serrano-Andrés, M. Urban, V. Veryazov, R. Lindh. *J. Comput. Chem.*, **2010**, *31*, 224-247.

[12] M. Goldman. *Spin Temperature and Nuclear Magnetic Resonance in Solids,* **1970**, Clarendon Press, Oxford.

[13] F. Pointillart, B. L. Guennic, S. Golhen, O. Cador, O. Maury, L. Ouahab. *Chem. Commun.*, **2013**, *49*, 615-617.

[14] K. S. Cole, R. H. Cole. *J. Chem. Phys.*, **1941**, *9*, 341-351.

[15] E. A. Quadrelli. *Inorg. Chem.,* **2002**, *41,* 147-149.

[16] D. Aguilà, L. A. Barrios, V. Velasco, L. Arnedo, N. Aliaga-Alcalde, M. Menelaou, S. J. Teat, O. Roubeau, F. Luis, G. Aromí. *Chem. Eur. J.*, **2011**, *19*, 5881-5891.

Chapter 5

Conclusion

5.1 Conclusion and Outlook

This research has successfully produced new complexes exhibiting various structural motifs and fascinating magnetic behaviors.

In chapter 2, eight dinuclear homometallic Ln^{III} complexes (**1-8**) have been synthesized using the ligand H_2ovph and the corresponding salts under varying reaction conditions. All these compounds were characterized by single X-ray diffraction and/or X-ray powder diffraction, and magnetism studied. Compounds **1-3** and **4-6** are isostructural with centrosymmetric architecture that can be divided into two series according to the coordinating solvent molecules of DMF and IPA, respectively. From the shape measure perspective, an average deviation over 4.5°, which can be considered as significant, has been found between these two series of complexes. The Dy^{III} analogues, **1** and **4**, from both series have been shown as more interesting magnetically than the rest, where typical SMM behavior was observed. Furthermore, the effective energy barriers were found to be 58 K ($\tau_0 = 3.51*10^{-6}$ s) and 98 K ($\tau_0 = 6.69*10^{-7}$ s) for **1** and **4**, respectively. Dysprosium-based SMMs **7** and **8** were synthesized and crystallographically characterized as well. Complex **7** contains a seven- and a nine-coordinated Dy^{III} center, while for **8** seven- and eight-coordinated Dy^{III} ions are observed. Except for the presence of the same ferromagnetic coupling as the other two Dy^{III} complexes **1** and **4**, the asymmetric structures of **7** and **8** resulted in an α parameter over 0.20 or multi-relaxation processes with anisotropic barriers of 110 K for the former, and 22 (1200 Oe), 8 (2800 Oe) K for the latter. Compared with other literature $\{Dy_2\}$ systems, the diversity in the source of the μ-O bridge seems to have a significant impact on the metal···metal distances and M-O-M angles. However, there has

been no clear evidence to prove that the bridging oxygen type or the distance and angle are related to the ferromagnetic interaction between the Dy^{III} centers. More theoretical calculations would be useful in the future to shed some more light on this topic.

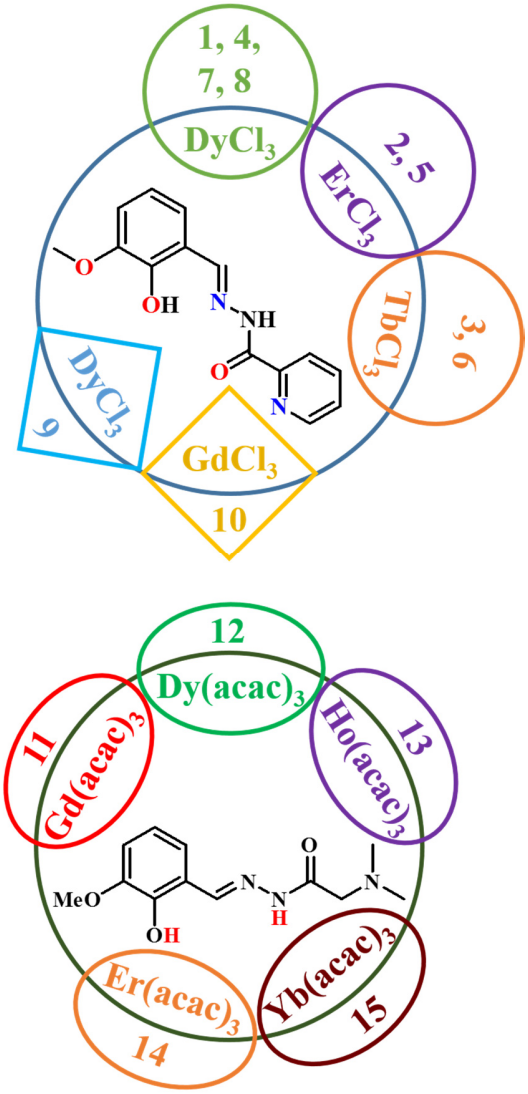

Figure 5.1 Schematic representation of all compounds (**1-15**).

Chapter 3 introduced the hexanuclear {Dy_6} complex (**9**) and its gadolinium analogue (**10**) with trigonal prism core structures. Both complexes were obtained using the ligand H_2ovph and the corresponding salts, with the absorption of CO_3^{2-} co-ligands forming the final structures. This kind of reaction is known as serendipitous synthesis. Crystallographic characterization and magnetic studies were carried out for both

complexes. The ac measurements suggest that compound **9** is an SMM, with an energy barrier of 102 K (τ_0 = 5.18*10^{-7} s). The comparison with previously reported similar compounds **Ref-11** and **Ref-12** was also presented, from structural differences, packing schemes and magnetism aspects, respectively. Among all three comparable complexes, ferromagnetic coupling was observed constantly, while **9** presented the highest barrier.

In chapter 4, five centrosymmetric complexes with general fomula [Ln^{III}_2(ovgrd)$_2$(acac)$_2$(H_2O)$_2$]·EtOH, Ln = Gd (**11**), Dy (**12**), Ho (**13**), Er (**14**) and Yb (**15**) were synthesized with ligand H_2ovgrd. This series of compounds crystallized in different space groups but inheriting the same structure from Gd^{III} to Yb^{III}. Furthermore, the study of lanthanide contraction was able to show, through Ln···Ln distances, O···O distances and average Ln-X (X = O, N) bond lengths three different ways. Magnetic studies were carried on all the complexes, the coupling constant was calculated based on Gd^{III} analogue **11** which revealed weak antiferromagnetic coupling with value of J = -0.01 cm^{-1} and g = 2.01. The Dy^{III} analogue **12** was found not to be an SMM which is due to the larger values of $\boldsymbol{g}_X$ and $\boldsymbol{g}_Y$ in the ground doublet of individual Dy^{III} ions obtained via *ab initio* calculations. On the other hand, Er^{III} **14** and Yb^{III} **15** were shown to exhibit slow relaxation of the magnetization.

Though the methods for synthesizing and characterizing complexes **1-15** are discussed in detail throughout this thesis, the theoretical understanding of their properties remains elusive and can be further investigated. For future work, we may expect more theoretical calculations to lead us close to the answer.

Chapter 6

Experimental Section

This chapter presents the syntheses of the reported ligands and complexes, in addition to various analytical techniques utilized to characterize and investigate the properties of these complexes.

6.1 Experimental Section for Complexes 1-8

Infrared Spectrometry

IR spectra were collected on all samples in the solid state on a Varian 640 FT-IR spectrometer in the 525-4000 cm^{-1} range.

X-ray Powder Diffraction

X-ray powder diffraction data for complex **5** was collected using RIGAKU Ultima IV, with Cu-Kα radiation (λ = 1.541836 Å), and a graphite monochromator. Scanning of the 2θ range from 5 to 40° was performed. The structure of the sample was confirmed by comparison between the collected pattern and the simulated pattern from the single XRD data of its analogue complex. As shown in Figure 6.1.

X-ray Crystallography

For complexes **1-4** and **6**, a single crystal suitable for X-ray diffraction measurements, was mounted on a glass fibre. Unit cell measurements and intensity data collections were performed on a Bruker-AXS SMART 1 k CCD diffractometer using graphite monochromated MoKα radiation (λ = 0.71073 Å). The data reduction included a correction for Lorentz and polarization effects, with and applied multi-scan absorption correction (SADABS). The crystal structure was solved and refined using the SHELXTL program suite. Direct methods yielded all non-hydrogen atoms which were refined with anisotropic

thermal parameters. All hydrogen atom positions were calculated geometrically and were riding on their respective atoms.

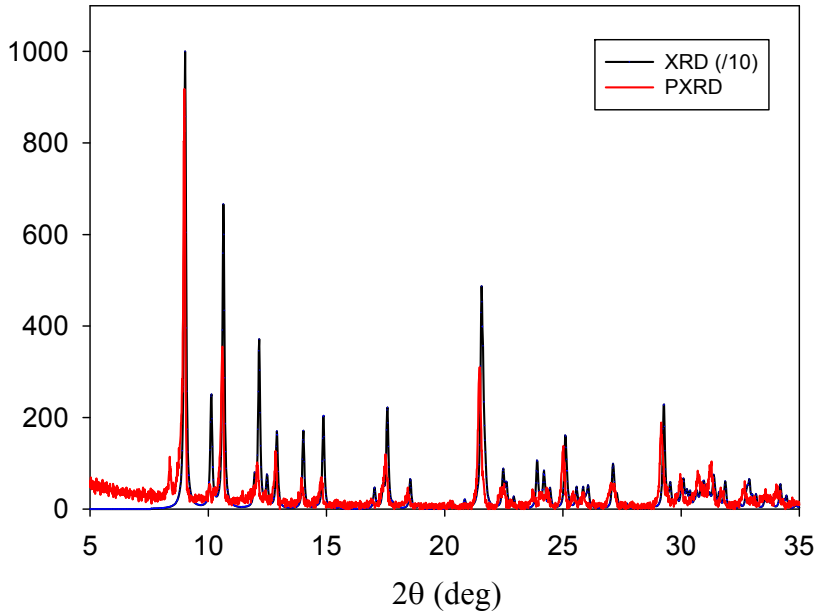

Figure 6.1 X-ray powder diffraction comparison between the calculated pattern obtained from single crystal X-ray data of complex **4** (black) and the experimental pattern (red) of complex **5** in the 5-40° 2θ region. The calculated pattern was divided by a factor of 10 for comparative purposes.

NMR Measurements

NMR analyses were conducted on a Bruker Avance 400 spectrometer equipped with an automatic sample holder and a 5 mm autotuning broadband probe with Z gradient.

Magnetic Measurements

The magnetic susceptibility were obtained using a Quantum Design SQUID magnetometer MPMS-XL7 in the temperature range of 1.8-300 K for dc-applied fields ranging from -7 to 7 T. Dc analyses were performed on polycrystalline samples of 9.3, 7.5, 12.7, 5.0, 16.4, 11.5, 7.8, 8.0 mg for **1**-**8**, respectively. All samples were wrapped in a polyethylene wrap and under a field ranging from 0 to 7 T in the temperature range of 1.8-300 K. Ac susceptibility measurements were carried out under an oscillating ac field of 3 Oe and ac frequencies ranging from 1 to 1500 Hz. The magnetization data was initially collected at 100 K in order to check ferromagnetic impurities, found to be absent in all samples. A

diamagnetic correction was applied for sample holder and the grease which was used to restrain the microcrystals preventing torqueing under high fields.

Synthesis of Schiff base 2-hydroxy-3-methoxybenzaldehyde (pyridine-2-carbonyl) hydrazone (H_2ovph)

The ligand H_2ovph was synthesized in accordance with previously published procedures.[1] 2-Pyridinecarboxylic acid (1371.4 mg, 10 mmol) and *o*-vanillin (1521.5 mg, 10 mmol) were mixed in 20 mL of methanol and treated with stirring for an hour at room temperature. The resulting white powder was collected by suction filtration and washed with cold methanol. Yield= 92%. ^{1}H NMR ($CDCl_3$, 400 MHz): δ 11.09 (s, 1H), 10.93 (s, 1H), 8.59 (m, 2H), 8.30 (dt, 1H), 7.92 (td, 1H), 7.50 (m, 1H), 6.90 (m, 3H), 3.94 (s, 3H). Selected IR (cm^{-1}): 3268 (m), 2930.90 (wk), 1674 (s), 1607 (s), 1589 (wk), 1524 (s), 1463 (s), 1434 (m), 1373 (m), 1235 (s), 1155 (m), 1111 (wk), 1077 (m), 1043 (wk), 998 (m), 968 (m), 901 (m), 901 (m), 834 (wk), 775 (m), 727 (s), 706 (m), 618 (m).

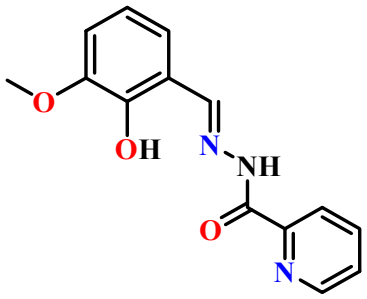

Scheme 6.1 The Schiff-base ligand H_2ovph.

Synthesis of $[Dy^{III}_2(ovph)_2(DMF)_2Cl_2]$ complex 1

To a solution of H_2ovph (54.2 mg, 0.2 mmol) and $NaHCO_3$ (33.6 mg, 0.4 mmol) in 10 mL of MeCN, a solution of $DyCl_3{\cdot}6H_2O$ (0.2 mmol) in 7 mL of DMF/IPA (2:5) was added. The yellow solution was stirred for 3 hours then filtered. The filtrate was placed in a diethyl ether bath to help crystallization at room temperature. Yellow rod-like crystals were isolated after 2 days in ~ 70% yield. Selected IR (cm^{-1}): 3242 (br), 1655 (s), 1599 (s), 1558 (m), 1474 (m), 1444 (m), 1385 (wk), 1337 (s), 1311 (w), 1296 (w), 1245 (s), 1216 (s), 1154 (m), 1106 (m), 1083 (m), 1047 (m), 1015 (m), 997 (wk), 968 (wk), 919 (m), 864 (m), 809 (s), 749 (m), 734 (s), 713 (m), 688 (m), 637 (m), 547 (m).

Synthesis of $[Er^{III}_2(ovph)_2(DMF)_2Cl_2]$ complex 2

This was prepared following the same procedure as for complex **1**, yellow rod-like crystals were obtained after one night in ~ 60% yield. IR is identical to complex **1**.

Synthesis of $[Tb^{III}_2(ovph)_2(DMF)_2Cl_2]$ complex 3

This was prepared following the same procedure as for complex **1**, orange rod-like crystals were obtained after one night in ~ 65% yield. IR is identical to complex **1**.

Synthesis of $[Dy^{III}_2(ovph)_2(IPA)_2Cl_2]$ complex 4

The same procedure as **1-3** was employed to synthesize **4** with DMF/2-Propanol mixed solvent being replaced by 2-Propanol (5 mL) only. All reagents were dried before using. Yellow needle-like crystals suitable for X-ray measurement were obtained after 2 days in ~ 20% yield. Selected IR (cm^{-1}): 3242 (br), 1599 (s), 1558 (m), 1474 (m), 1444 (m), 1385 (w), 1337 (s), 1311 (w), 1296 (w), 1245 (s), 1216 (s), 1154 (m), 1106 (m), 1083 (m), 1047 (m), 1015 (m), 997 (w), 968 (w), 919 (m), 864 (m), 809 (s), 749 (m), 734 (s), 713 (m), 688 (m), 637 (m), 547 (m).

Synthesis of $[Er^{III}_2(ovph)_2(IPA)_2Cl_2]$ complex 5

This is prepared following the same procedure as for complex **4**, orange needle-like crystals were obtained after one night in ~ 42% yield. IR is identical to complex **4**.

Synthesis of $[Tb^{III}_2(ovph)_2(IPA)_2Cl_2]$ complex 6

This is prepared following the same procedure as for complex **4**, orange rod-like crystals were obtained after three to five days in ~ 45% yield. IR is identical to complex **4**.

Synthesis of $[Dy^{III}_2(ovph)_2(H_2O)_3(EtOH)Cl_2]$ complex 7

H_2ovph (54.2 mg, 0.2 mmol) and $NaHCO_3$ (33.6 mg, 0.4 mmol) was dissolved in 10 mL of MeCN, combined with a solution of $DyCl_3$ (anhydrated) in 5 mL of EtOH. The yellow solution was stirred for 10 mins at room temperature then filtered. The filtrate was placed in a diethyl ether bath to help crystallization at room temperature. Yellow rhombus shape crystals were isolated after 2 days in ~65% yield. Selected IR (cm^{-1}): 3327 (br), 2991 (wk), 1650 (wk), 1597 (s), 1552 (s), 1533 (m), 1476 (m), 1460 (m), 1442 (s), 1381 (wk), 1343 (s), 1324 (wk), 1299 (m), 1253 (wk), 1234 (s), 1209 (s), 1158 (m), 1099 (wk), 1079 (m), 1048

(m), 1019 (m), 974 (wk), 963 (m), 919 (m), 884 (wk), 859 (m), 807 (wk), 801 (wk), 736 (s), 691 (s), 633 (m).

Synthesis of $[Dy^{III}_2(Hovph)_2(OH)Cl_3(H_2O)]\cdot 2H_2O$ complex 8

H_2ovph (54.2 mg, 0.2 mmol) and $NaHCO_3$ (33.6 mg, 0.4 mmol) was dissolved in 10 mL of MeCN, combined with a solution of $DyCl_3\cdot 6H_2O$ in 5 mL of IPA. The yellow solution was stirred for 30 mins at room temperature then filtered. The filtrate was placed in a diethyl ether bath to help crystallization at room temperature. Yellow crystals were isolated after 2 days in ~40% yield. Selected IR (cm^{-1}): 3160 (br), 1607 (s), 1158 (m), 1535 (m), 1466 (w), 1438 (m), 1435 (s), 1407 (m), 1339 (m), 1284 (m), 1243 (m), 1214 (s), 1151 (m), 1080 (m), 1050 (w), 1020 (w), 1017 (w), 957 (w), 909 (w), 850 (w), 801 (w), 760 (w), 733 (s), 715 (m), 680 (s), 638 (s), 598 (m), 552 (w).

6.2 Experimental Section for Complexes 9-10

Infrared Spectrometry

IR spectra were collected on complex **9** in the solid state on a Varian 640 FT-IR spectrometer in the 525-4000 cm^{-1} range.

X-ray Crystallography

For complexes **9** and **10**, a single crystal suitable for X-ray diffraction measurements, was mounted on a glass fibre. Unit cell measurements and intensity data collections were performed on a Bruker-AXS SMART 1 k CCD diffractometer using graphite monochromated MoKα radiation (λ = 0.71073 Å). The data reduction included a correction for Lorentz and polarization effects, with and applied multi-scan absorption correction (SADABS). The crystal structure was solved and refined using the SHELXTL program suite. Direct methods yielded all non-hydrogen atoms which were refined with anisotropic thermal parameters. All hydrogen atom positions were calculated geometrically and were riding on their respective atoms.

Magnetic Measurements

The magnetic susceptibility were obtained using a Quantum Design SQUID magnetometer MPMS-XL7 in the temperature range of 1.8-300 K for dc-applied fields ranging from -7 to

7 T. Dc analyses were performed on polycrystalline samples of 5.5 and 0.8 mg for **9** and **10**, respectively. All samples were wrapped in a polyethylene wrap and under a field ranging from 0 to 7 T in the temperature range of 1.8-300 K. Ac susceptibility measurements were carried out under an oscillating ac field of 3 Oe and ac frequencies ranging from 1 to 1500 Hz. The magnetization data was initially collected at 100 K in order to check ferromagnetic impurities, found to be absent in both samples. A diamagnetic correction was applied for sample holder and the grease which was used to restrain the microcrystals preventing torqueing under high fields.

Synthesis of 2-hydroxy-3-methoxybenzaldehyde (pyridine-2-carbonyl) hydrazone (H_2ovph)

The Schiff-base ligand H_2ovph is synthesized by the condensation of picolinoyl hydrazide and *o*-vanillin in a 1:1 ratio in methanol according to the reported procedure. [1]

Synthesis of $[Dy^{III}_6(ovph)_6(IPA)_3Cl_3]\cdot 6MeCN\cdot IPA\cdot TEAOH$ complex 9

To a solution of H_2ovph (54.2 mg, 0.2 mmol) and TEAOH (74.7 mg, 0.4 mmol) in 10 mL of MeCN, a solution of $DyCl_3$·anhydrate (53.77 mg, 0.2 mmol) in 5 mL of IPA was added. The yellow solution was stirred for 2.5 hours then filtered. By slow evaporation of the filtrate at room temperature, yellow square crystals were isolated after 5 days in ~ 40% yield. Selected IR (cm^{-1}): 3346 (br), 1602 (s), 1556 (m), 1475 (s), 1444 (s), 1339 (s), 1297 (w), 1237 (m), 1216 (m), 1157 (w), 1084 (w), 1046 (w), 1018 (w), 969 (w), 949 (w), 921 (w), 870 (m), 804 (w), 735 (s), 714 (m), 688 (s), 637 (s).

Synthesis of $[Gd^{III}_6(ovph)_6(IPA)_3Cl_3]\cdot 6MeCN\cdot IPA\cdot TEAOH$ complex 10

This was prepared following the same procedure as for complex **9**, orange rectangle crystals were obtained after two weeks in ~ 12% yield. IR is identical to complex **9**.

6.3 Experimental Section for Complexes 11-15

Infrared Spectrometry

IR spectra were collected on all samples in the solid state on a Varian 640 FT-IR spectrometer in the 525-4000 cm^{-1} range.

X-ray Powder Diffraction

X-ray powder diffraction data for complex **15** was collected using RIGAKU Ultima IV, with Cu-Kα radiation (λ = 1.541836 Å), and a graphite monochromator. Scanning of the 2θ range from 5 to 40° was performed. The structure of the sample was confirmed by comparison between the collected pattern and the simulated pattern from the single XRD data of its analogue complex.

X-ray Crystallography

For complexes **11-14**, a single crystal suitable for X-ray diffraction measurements, was mounted on a glass fibre. Unit cell measurements and intensity data collections were performed on a Bruker-AXS SMART 1 k CCD diffractometer using graphite monochromated MoKα radiation (λ = 0.71073 Å). The data reduction included a correction for Lorentz and polarization effects, with and applied multi-scan absorption correction (SADABS). The crystal structure was solved and refined using the SHELXTL program suite. Direct methods yielded all non-hydrogen atoms which were refined with anisotropic thermal parameters. All hydrogen atom positions were calculated geometrically and were riding on their respective atoms.

NMR Measurements

NMR analyses were conducted on a Bruker Avance 400 spectrometer equipped with an automatic sample holder and a 5 mm auto tuning broadband probe with Z gradient.

Magnetic Measurements

The magnetic susceptibility were obtained using a Quantum Design SQUID magnetometer MPMS-XL7 in the temperature range of 1.8-300 K for dc-applied fields ranging from -7 to 7 T. Dc analyses were performed on polycrystalline samples of 7.8, 7.7, 19.5, 11.9, 7.8 mg for **11-15**, respectively. All samples were wrapped in a polyethylene wrap and under a field ranging from 0 to 7 T in the temperature range of 1.8-300 K. Ac susceptibility measurements were carried out under an oscillating ac field of 3 Oe and ac frequencies ranging from 1 to 1300 Hz. The magnetization data was initially collected at 100 K in order to check ferromagnetic impurities, found to be absent in all samples. A diamagnetic correction was applied for sample holder and the grease which was used to restrain the microcrystals preventing torqueing under high fields.

Synthesis of Schiff base (E)-2-(dimethylamino)-N'-(2-hydroxy-3-methoxybenzylidene) acetohydrazide (H_2ovgrd)

Girard's reagent D (380.12 mg, 2 mmol) and pyridine (314.4 mg, 4 mmol) were added into 20 mL of MeOH, kept stirring the mixture until a completed dissolution. Then *o*-vanillin (304.3 mg, 2 mmol) in 5 mL MeOH was combined to the system and treated with stirring for 2 hours at room temperature. The resulting white/light yellow color suspend was collected and washed with cold MeOH. Yield = 68%. Selected IR (cm^{-1}): 3367 (br), 2900 (wk), 2627 (br), 1474 (s), 1409 (wk), 1374 (m), 1276 (s), 1259 (m), 1241 (m), 1205 (wk), 1149 (s), 1255 (s), 1226 (m), 1203 (wk), 1184 (wk), 1145 (wk), 1052 (s), 1009 (m), 975 (m), 965 (m), 912 (wk), 859 (wk), 764 (s), 725 (s), 610 (m). ^{1}H NMR (MeOD, 400 MHz): δ 8.39 (s, 1H), 7.24 (d, 1H), 6.99 (d, 1H), 6.83 (t, 1H), 4.52 (s, 2H), 4.10 (s, 1H), 3.88 (s, 3H), 3.00 (s, 6H).

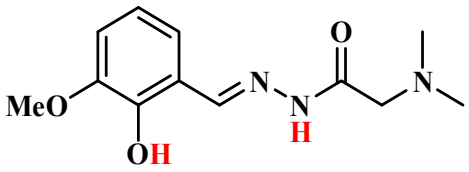

Scheme 6.2 The Schiff base ligand H_2ovgrd.

Synthesis of $[Dy^{III}_2(ovgrd)_2(acac)_2(H_2O)_2]\cdot$EtOH complex 12

H_2ovgrd (50.26 mg, 0.2 mmol) in 10 mL MeCN was treated with tetraethylammonium hydroxide (TEAOH, 264 µL, 0.4 mmol), then a solution of $Dy(acac)_3\cdot 6H_2O$ (0.2 mmol) in 5 mL EtOH was combined. The mixture was stirring for 2 mins then filtered and kept the filtrate at room temperature. Light yellow color needle-like crystals were isolated after 1 night ~ 60% yield. Selected IR (cm^{-1}): 3242 (br), 2965 (wk), 2832 (wk), 1402 (s), 1360 (s), 1309 (s), 1238 (s), 1184 (m), 1129 (m), 1106 (s), 1263 (wk), 1233 (m), 1211 (s), 1102 (wk), 1080 (wk), 1049 (wk), 1020 (m), 988 (wk), 950 (s), 923 (m), 855 (s), 769 (m), 734 (s).

Synthesis of $[Gd^{III}_2(ovgrd)_2(acac)_2(H_2O)_2]\cdot$EtOH complex 11

This was prepared following the same procedure as for complex **12** but under stirring for 13 mins. Light yellow color needle-like crystals obtained after 3 days in ~20% yield. IR is identical to complex **12**.

Synthesis of $[Ho^{III}_2(ovgrd)_2(acac)_2(H_2O)_2]\cdot$EtOH complex 13

This was prepared following the same procedure as for complex **12**. Pale yellow color needle-like crystals obtained after few hours in ~55% yield. IR is identical to complex **12**.

Synthesis of $[Er^{III}_2(ovgrd)_2(acac)_2(H_2O)_2]\cdot EtOH$ complex 14

This was prepared following the same procedure as for complex **12**. Pale pink color needle-like crystals obtained after one night in ~40% yield. IR is identical to complex **12**.

Synthesis of $[Yb^{III}_2(ovgrd)_2(acac)_2(H_2O)_2]\cdot EtOH$ complex 15

This was prepared following the same procedure as for complex **12**. Pale white color needle-like crystals obtained after one night in ~35% yield. IR is identical to complex **12**.

6.4 Reference

[1] M. L. Liu, J. M. Dou, D. Q. Wang, D. C. Li. *Acta. Cryst.,* **2005**, *E61*, o3876-o3878.

Appendix

Appendix A: Crystallographic data

Table A.1 Crystallographic data of the dinuclear complexes **1-4** and **6**

	1	**2**	**3**	**4**	**6**
formula	$C_{34}H_{36}Cl_2Dy_2N_8O_8$	$C_{34}H_{36}Cl_2Er_2N_8O_8$	$C_{34}H_{36}Cl_2Tb_2N_8O_8$	$C_{34}H_{38}Cl_2Dy_2N_6O_8$	$C_{34}H_{38}Cl_2Tb_2N_6O_8$
fw	1080.61	1090.13	1073.45	1052.59	1047.44
T/K	200(2)	200(2)	200(2)	200(2)	200(2)
crystal system	Monoclinic	Monoclinic	Monoclinic	Monoclinic	Monoclinic
space group	$P2_1/n$	$P2_1/n$	$P2_1/n$	$P2_1/n$	$P2_1/n$
a/Å	9.2840(5)	9.22190(10)	9.2526(2)	9.2698(2)	9.3554(8)
b/Å	12.1401(6)	11.9769(2)	11.9630(2)	12.1313(3)	12.1892(11)
c/Å	17.5090(8)	17.4808(3)	17.5928(4)	16.9364(4)	16.9152(16)
α/deg	90	90	90	90	90
β/deg	98.4461(11)	97.798	97.9100(9)	101.2440(10)	101.5572(14)
γ/deg	90	90	90	90	90
Vol/Å^3	1952.01(17)	1912.90(5)	1928.80(7)	1868.02(8)	1891.4(3)
Z	2	2	2	2	2
DC/ Mg m^{-3}	1.839	1.893	1.848	1.871	1.839

	1	**2**	**3**	**4**	**6**
μ/mm^{-1}	3.994	4.557	3.835	4.170	3.907
Reflns collected	27137	32433	32563	11000	23958
GOF	1.017	1.014	1.006	1.093	1.060
*R1, wR*2 (>2σ(I))[a]	0.0267, 0.0648	0.0284, 0.0581	0.0243, 0.0603	0.0413, 0.0896	0.0543, 0.1110
*R1, wR*2 (all data)	0.0388, 0.0716	0.0451, 0.0647	0.0299, 0.0633	0.0319, 0.0853	0.0787, 0.1221

[a] $R=R_1=||F_o| - |F_c||/\Sigma|F_o|$; $wR_2 = \{[\Sigma w(F_o^2-F_c^2)^2]/[w(F_o^2)^2]\}^{1/2}$; $w=1/[\sigma^2(F_o^2)+(ap)^2+bp]$, where $p=[\max(F_o^2,0)+2Fc^2]/3$.

Table A.2 Crystallographic data for the dinuclear complexes **7** and **8**

	7	**8**
formula	$C_{30}H_{33}Cl_2Dy_2N_6O_{10}$	$C_{28}H_{31}Cl_3Dy_2N_6O_{10}$
fw	1033.52	1041.46
T/K	200(2)	200(2)
crystal system	Monoclinic	Triclinic
space group	$P2_1/c$	*P1*
a/Å	9.4224(3)	10.9339(2)
b/Å	11.7141(4)	14.0384(3)
c/Å	30.8652(10)	14.7440(4)
α/deg	90	83.1270(10)
β/deg	96.162(2)	69.8550(10)
γ/deg	90	75.5170(10)
Vol/Å^3	3387.06(19)	2055.76(8)
Z	4	2
DC/ Mg m^{-3}	2.027	1.683
μ/mm^{-1}	4.602	3.852
Reflns collected	5747	10117
GOF	1.244	1.023
*R1, wR*2 (>2σ(I))[a]	0.0897, 0.1836	0.0396, 0.1054
*R1, wR*2 (all data)	0.1031, 0.1883	0.0566, 0.1150

[a] $R=R_1=||F_o| - |F_c||/\Sigma|F_o|$; $wR_2 = \{[\Sigma w(F_o^2-F_c^2)^2]/[w(F_o^2)^2]\}^{1/2}$; $w=1/[\sigma^2(F_o^2)+(ap)^2+bp]$, where $p=[\max(F_o^2,0)+2Fc^2]/3$.

Table A.3 Crystallographic data of the polynuclear complexes **9**, **10**, **Ref-11** and **Ref-12**

	9	**10**	**Ref-11**	**Ref-12**
formula	$C_{108}H_{120.25}Cl_3Dy_6N_{22.75}O_{27.5}$	$C_{107}H_{117}Cl_3Gd_6N_{23}O_{27}$	$C_{183}H_{190}Dy_{12}N_{48}O_{74}$	$C_{89}H_{81}Cl_4Dy_6N_{19}O_{28}$
fw	3258.36	3207.08	6195.83	2981.53
T/K	200(2)	200(2)	296(2)	191(2)
crystal system	Monoclinic	Monoclinic	Monoclinic	Monoclinic
space group	$P2_1/n$	$P2_1/n$	$P2_1/n$	$P2_1/n$
a/Å	29.3565(12)	29.8398(6)	33.272(3)	17.8984(8)
b/Å	15.5405(6)	15.5808(4)	25.317(2)	27.6222(12)
c/Å	29.9095(11)	29.9083(7)	27.923(2)	25.0228(11)
α/deg	90	90	90	90
β/deg	97.001(2)	97.5686(11)	106.009(2)	92.8880(10)
γ/deg	90	90	90	90
Vol/Å^3	13543.4(9)	13784.1(6)	22609(3)	12355.4(9)
Z	4	4	4	4
DC/ Mg m^{-3}	1.598	1.545	1.820	1.603
μ/mm^{-1}	3.399	2.973	4.005	0.71073
Reflns collected	150811	222170	44817	63574
GOF	1.054	1.034	1.043	0.997
*R1, wR*2 (>2σ(I))[a]	0.0357, 0.0860	0.0353, 0.0992	0.0681, 0.1702	0.0600, 0.1740
*R1, wR*2 (all data)	0.0567, 0.0985	0.0471, 0.1091	0.1170, 0.2105	0.1078, 0.2085

[a] $R=R_1=||F_o| - |F_c||/\Sigma|F_o|$; $wR_2 = \{[\Sigma w(F_o^2-F_c^2)^2]/[w(F_o^2)^2]\}^{1/2}$; $w=1/[\sigma^2(F_o^2)+(ap)^2+bp]$, where $p=[\max(F_o^2,0)+2Fc^2]/3$.

Table A.4 Crystallographic data of the dinuclear complexes **11-14**

	11	**12**	**13**	**14**
formula	$C_{36}H_{54}Gd_2N_6O_{11}$	$C_{36}H_{54}Dy_2N_6O_{11}$	$C_{36}H_{54}Ho_2N_6O_{11}$	$C_{18}H_{27}ErN_3O_{6.5}$
fw	1119.42	1129.92	1134.78	579.72
T/K	200(2)	200(2)	200(2)	200(2)
crystal system	Monoclinic	Monoclinic	Monoclinic	Triclinic
space group	$P2_1/n$	$P2_1/n$	$P2_1/c$	$P\bar{1}$
a/Å	11.3263(3)	11.3404(5)	11.2891(8)	8.5864(6)
b/Å	8.3727(2)	8.3937(3)	8.3607(6)	10.3618(8)
c/Å	20.7908(5)	20.8588(8)	20.7052(13)	11.2646(9)
α/deg	90	90	90	74.961(3)
β/deg	102.8720(11)	102.218(2)	102.908(4)	86.219(3)
γ/deg	90	90	90	78.632(3)
Vol/Å^3	2261.48(9)	2282.77(13)	2242.3(3)	1115.24(12)
Z	2	2	2	2
DC/ Mg m^{-3}	1.673	1.673	1.710	1.723
μ/mm^{-1}	2.976	3.314	3.572	3.799
Reflns collected	29945	35453	29375	8337
GOF	1.013	1.063	1.049	1.059
*R1, wR*2 (>2σ(I))[a]	0.0200, 0.0503	0.0492, 0.1028	0.0528, 0.1034	0.0381, 0.0959
*R1, wR*2 (all data)	0.0212, 0.0510	0.0765, 0.1112	0.0849, 0.1114	0.0421, 0.0987

[a] $R=R_1=||F_o| - |F_c||/\Sigma|F_o|$; $wR_2 = \{[\Sigma w(F_o^2-F_c^2)^2]/[w(F_o^2)^2]\}^{1/2}$; $w=1/[\sigma^2(F_o^2)+(ap)^2+bp]$, where $p=[\max(F_o^2,0)+2Fc^2]/3$.